LOWER HYBRID HEATING IN THE ALCATOR A TOKAMAK

J.J. Schuss, M. Porkolab, Y. Takase, D. Cope, S. Fairfax, M. Greenwald, D. Gwinn, I.H. Hutchinson, B. Kusse, E. Marmar, D. Overskei, D. Pappas, R.R. Parker, L. Scaturro, J. West, S. Wolfe

Plasma Fusion Center and Francis Bitter National Magnet Laboratory, M.I.T.

Cambridge, Massachusetts 02139

PFC/RR-80-6

LOWER HYBRID HEATING IN THE ALCATOR A TOKAMAK

J.J. Schuss, M. Porkolab, Y. Takase, D. Cope, S. Fairfax, M. Greenwald, D. Gwinn, I.H. Hutchinson, B. Kusse, E. Marmar, D. Overskei, D. Pappas, R.R. Parker, L. Scaturro, J. West, S. Wolfe

Plasma Fusion Center and Francis Bitter National Magnet Laboratory, M.I.T.

Cambridge, Massachusetts 02139

PFC/RR-80-6

LOWER HYBRID HEATING IN THE ALCATOR A TOKAMAK

J.J. Schuss, M. Porkolab, Y. Takase, D. Cope, S. Fairfax, M. Greenwald, D. Gwinn, I.H. Hutchinson, B. Kusse, E. Marmar, D. Overskei, D. Pappas, R.R. Parker, L. Scaturro, J. West, S. Wolfe

Plasma Fusion Center and Francis Bitter National Magnet Laboratory
Massachusetts Institute of Technology
Cambridge, Massachusetts 02139

Abstract

The results and interpretation of the modest power ($\sim$ 90 kW) lower hybrid heating experiment on Alcator A are presented. The expected results from linear waveguide-plasma coupling theory are outlined, and the possible effects of parametric instabilities, scattering from density fluctuations, and imperfect energetic ion confinement are addressed.

It is found experimentally that good coupling and the absence of rf breakdown are achieved with a double waveguide array at available rf power densities $P_{rf} \leq 4.5$ kW/cm^2, the waveguide vacuum windows being outside the toroidal field magnets; a waveguide array having vacuum windows near the waveguide mouth so that the $\omega = \omega_{ce}$ layer can be pressurized shows no breakdown at $P_{rf} > 8$ kW/cm^2 when a single waveguide is energized. Energetic ion production and a factor of 50 increase in the fusion neutron rate are observed to take

place at well defined values of central plasma density; below these densities electron heating occurs. The ion tail production is found to be independent of the relative phase of the double waveguide array employed. This ion heating occurs at a lower density than theoretically expected; together with the electron heating this indicates waves having $n_{||} \sim 5$ being absorbed near the plasma center. Probes at the plasma edge observe a frequency downshifted and broadened rf pump signal that is strongly attenuated as the plasma density increases through the neutron production band. These anomalous heating results and probe signals can be explained by a parametric decay of the pump wave into higher $n_{||}$ lower hybrid waves near the plasma edge. An alternate qualitative explanation would be the poloidal scattering of the lower hybrid waves at the plasma periphery due to density fluctuations; the $n_{||}$ of the scattered lower hybrid waves would then increase as they propagated inward due to magnetic shear. The neutron rate decay times imply that the rf creates ion tails having a substantial fraction of their energy above 50 keV. The neutron decay times and rates strongly depend on plasma current and indicate the expected influence of ion confinement on rf heating efficiencies. Finally the rf heating efficiencies are assessed.

I. Introduction

Wave injection near the lower hybrid frequency has been proposed for many years as a possible scheme of auxiliary heating of tokamaks. This method of heating would have the advantage of using waveguides external to the vacuum vessel for coupling the wave energy into the plasma. In principle, either electron or ion heating could be obtained by a suitable choice of frequency and wave vector. Furthermore, high power radio frequency sources in the relevant frequency range of several gigahertz are readily available.

Experiments have been carried out exploring this technique in the following tokamaks: ATC[1-4], Wega[5], Petula[6,7], JFT-2[8,9], JIPP T-II[10], and Doublet IIA[11]. With the exception of the Wega experiment, which employed loops, good waveguide - plasma coupling was obtained in these experiments. Both electron and ion heating was observed at plasma parameters consistent with theoretical expectations. The ion heating was generally accompanied by a density rise and in some cases by an increase in impurities. The rf power density at the waveguide mouth was at or below 1 kW/cm^2, although in the Petula experiment power densities of 8.5 kW/cm^2 were achieved for short pulses ($t \sim 100$ μsec) and 5 kW/cm^2 for 2 msec pulses.

In this paper we shall present the results of the moderate power ($P < 100$ kW) Alcator A lower hybrid heating experiment. In this experiment rf power densities of up to 8 kW/cm^2 were achieved for 40 msec pulses. Both electron and ion heating were observed as the plasma density was varied. No impurity influx or density rise was observed due to the rf pulse. However the ion heating, as evidenced by the formation of an energetic ion tail

in the plasma center, occurred at a lower plasma density than expected from linear plasma wave theory. Furthermore the electron heating observed at lower densities was not expected from linear waveguide plasma coupling theory. Contrary to expectations, the ion heating was found to be independent of the waveguide phasing. These results together with rf probe measurements in the edge plasma suggest that the lower hybrid waves launched by the array may undergo strong scattering from parametric instabilities or density fluctuations near the plasma edge. Thus surface interaction strongly modifies the wave behavior from that expected from linear, quiescent plasma theory. From evidence obtained from the neutron rates we further infer that energetic ion confinement played a role in ion heating. These results from the Alcator A lower hybrid heating experiment are the first on a tokamak that clearly demonstrate a modification of the lower hybrid $\vec{k}$ spectrum at the plasma edge and allow some insight into the importance of this effect in high density, high magnetic field plasmas. Some of these observations have been previously reported.[12,13]

In Section II linear lower hybrid wave theory will be reviewed, including waveguide - plasma coupling theory. Possible parametric processes near the edge plasma will be considered and the relevant thresholds calculated. Drift wave scattering theory will be reviewed; it will be shown that in some cases the effect of magnetic field shear together with drift wave scattering at the plasma edge can cause <u>increased</u> wave accessibility to the plasma center. Ion confinement will be reviewed as it applies to Alcator A. In Section III

the experimental results will be presented, including the anomalous heating results and probe spectra. Evidence will be presented that exhibits the effect of ion confinement on plasma heating. In Section IV conclusions will be drawn concerning this work that are relevant to future higher power lower hybrid heating experiments.

II. Theory

A. Linear Wave Theory

Here we review lower hybrid wave propagation in a magnetized plasma and summarize the conditions necessary for accessibility of the wave to the plasma center and its subsequent absorption there. This material is taken from the extensive literature on this subject[14-23].

Near the edge of a tokamak plasma where the ion and electron temperatures are low, the cold plasma dispersion relation describes the evolution of $n_x = k_x\, c/\omega$:

$$n_x^4\, \varepsilon_{xx} + n_x^2 \left[- \varepsilon_{xy}^2 + (\varepsilon_{xx} + \varepsilon_{zz})(n_z^2 - \varepsilon_{xx}) \right]$$

$$+ \varepsilon_{zz} \left[(n_z^2 - \varepsilon_{xx})^2 + \varepsilon_{xy}^2 \right] = 0 \qquad (1)$$

where $n_z = k_z\, c/\omega$, we approximate $\vec{E} \sim \vec{E}_o \exp(ik_x x + ik_z z)$, $\vec{B}$ is in the z direction and

$$\varepsilon_{xx} = 1 + \frac{\omega_{pe}^2}{\omega_{ce}^2} - \frac{\omega_{pe}^2}{\omega^2}$$

$$\varepsilon_{xy} = \frac{i\omega_{pe}^2}{\omega\omega_{ce}} \qquad (1a)$$

$$\varepsilon_{zz} = 1 - \frac{\omega_{pe}^2}{\omega^2}$$

$\omega_{ce} = e B_o/(m_e c)$, and $\omega_{p\alpha}^2 = 4\pi n e^2/m_\alpha$. When $\varepsilon_{xx} \to 0$, $n_x^2 \to \infty$ and there is a resonance in the plasma at a density

$$\omega_{pi}^2 = \omega^2/(1 - \omega^2/\omega_{ce}\omega_{ci}) \qquad (2)$$

which defines the cold plasma lower hybrid resonance layer. Thermal effects described below will significantly modify this resonance in the hot central plasma. In order for the wave to reach the central plasma, it must not mode convert into a whistler wave, which is then confined to the plasma exterior. This occurs when the two solutions to n_x^2 of Eq. (1) converge, at a density

$$\frac{\omega_{pi}}{\omega} \simeq \frac{n_z \omega}{(\omega_{ce}\omega_{ci})^{1/2}} - \left[n_z^2 \left(\frac{\omega^2}{\omega_{ce}\omega_{ci}} - 1 \right) + 1 \right]^{1/2} . \qquad (3)$$

For $n_z > (1 - \omega^2/\omega_{ce}\omega_{ci})^{1/2} \equiv n_{za}$ the wave will not mode convert at any density and will be accessible to the plasma center. Similarly for $\omega \geq \sqrt{\omega_{ce}\omega_{ci}}$, n_{za} is infinite and the waves are not accessible to the plasma center for any n_z. For the Alcator A experiment at 60 kG and deuterium $n_{za} \simeq 2.1$; n_{za} is reduced to about 1.3 for 80 kG and deuterium or 60 kG and hydrogen. We expect that the wave power having $1 < n_z < n_{za}$ will go into surface waves and not heat the

plasma center.

From Eq. (1) it can also be seen that when $\varepsilon_{zz} = 0$ $n_x = 0$. For $\varepsilon_{zz} \simeq 0$ and n_z not too close to 1 Eq. (1) becomes

$$n_x^2 \simeq \varepsilon_{zz}(1 - n_z^2) \quad . \tag{4}$$

We see that for $n_z < 1$ the lower hybrid wave propagates for $\omega_{pe} < \omega$ but is evanescent at $\omega_{pe} > \omega$, whereas the situation is reversed for $n_z > 1$. The waves with $n_z > 1$ are those that will heat the plasma and therefore must travel between the waveguides and the $\omega = \omega_{pe}$ layer. In general this layer is at a low density $n_e \sim 10^{11} cm^{-3}$ and is very close to the waveguide mouth. It should be noted that as $n_z \to 1$ the mode conversion layer of Eq. (3) will asymptote the $\omega = \omega_{pe}$ layer and modify this cutoff, although waves with $n_z > 1$ will still be evanescent when $\omega > \omega_{pe}$.

In the plasma interior for $n_z > n_{za}$, n_x will rise and the wave will become electrostatic. Thermal corrections to Eq. (1) will then be important; specifically $\varepsilon_{xx} = \varepsilon_{xxo} + k_x^2 \varepsilon_{xx1}$, where ε_{xxo} is the cold plasma ε_{xx} and

$$\varepsilon_{xx1} = -\frac{c^2}{\omega^2}\left(3\frac{\omega_{pi}^2}{\omega^2}\frac{T_i}{M_i c^2} + \frac{3}{4}\frac{\omega_{pi}^2\omega^2}{(\omega_{ce}\omega_{ci})^2}\frac{T_e}{M_i c^2}\right) \tag{5}$$

$$= -\frac{c^2}{\omega^2}\frac{\omega_{pi}^2}{\omega^2} a_T$$

We then can obtain the electrostatic dispersion relation

$$\vec{k} \cdot \overline{\overline{\varepsilon}} \cdot \vec{k} = 0$$

or $(\varepsilon_{xxo} + k_x^2 \varepsilon_{xxl})\, k_x^2 + k_z^2 \varepsilon_{zzo} = 0$. The two solutions to this dispersion relation coalesce at the lower hybrid mode conversion layer at a density

$$\omega_{pi}^2 = \frac{\omega^2}{1 - \frac{\omega^2}{\omega_{ce}\omega_{ci}} + 2\, n_z \sqrt{\frac{M_i}{m_e}}\, a_T} \qquad (6)$$

This density is lower than that of Eq. (2) and beyond this density both modes are evanescent. At this density an incident lower hybrid wave will mode convert into an ion mode whose k_x will become large. When $k_x\, v_{Ti}/\omega \sim 1$ perpendicular ion Landau damping can occur and absorb the wave. We thus expect strong ion wave absorption when the lower hybrid mode conversion layer is present in the plasma interior. When the plasma density is substantially lower than that of Eq. (6), we do not expect wave damping due to ion heating.

There are three linear damping mechanisms that can absorb a lower hybrid wave: perpendicular ion Landau damping, electron Landau damping, and collisional absorption. These processes can be included into the dispersion relation by letting $\overline{\varepsilon} = \overline{\overline{\varepsilon}}_o + \delta\overline{\overline{\varepsilon}}$, where $\delta\overline{\overline{\varepsilon}}$ contains the damping terms. We obtain

$$\delta\varepsilon_{xx} = i\,\frac{\nu_{eff}}{\omega}\,\frac{\omega_{pe}^2}{\omega_{ce}^2} + i\,\frac{2\sqrt{\pi}}{k_x^3 v_{Ti}^3}\,\omega_{pi}^2\omega\; e^{-\frac{\omega^2}{k_x^2 v_{Ti}^2}} \qquad (7a)$$

and

$$\delta\varepsilon_{zz} = i\,\frac{\nu_{eff}}{\omega}\,\frac{\omega_{pe}^2}{\omega^2} + i\,\frac{\sqrt{\pi}}{k_z^2\lambda_D^2}\,\frac{\omega}{k_z v_{Te}}\; e^{-\frac{\omega^2}{k_z^2 v_{Te}^2}} \qquad (7b)$$

where $\nu_{eff} \simeq 3.34\,\frac{ne^4 \ln\Omega}{m_e^{1/2} T_e^{3/2}}$

and $v_{Ti,e} = \sqrt{2\,T_{e,i}/m_{e,i}}$. The second term of Eq. (7a) is obtained by treating the ions as unmagnetized. In the limit of $k_x\rho_i >> 1$, where $\rho_i = v_{Ti}/\omega_{ci}$ this produces an equivalent result to treating the ions as magnetized[24]. The first term of Eq. (7a) leads to collisional damping when $\omega_{pe}^2/\omega_{ce}^2$ is not small. This process is enhanced when k_x is large and can be strong near the mode conversion layer[25,26]. It has been shown[26] that the lower hybrid wave will be absorbed near the mode conversion layer if

$$\Delta x = \frac{a_T c^2}{4\,\nu_{eff}^2 \left(\frac{\omega_{pe}^2}{\omega_{ce}^2}\right)^2 L} \ll \frac{a}{2} \qquad (8)$$

where a is the plasma minor radius or a characteristic plasma dimension, $L \equiv |\frac{1}{n}\frac{dn}{dx}|^{-1}$, and all quantities are evaluated at the mode conversion layer. For $L \sim 10$ cm, $n_e = 3 \times 10^{14}\,cm^{-3}$, $B_T = 60$ kG, and $T_i = T_e = 1$ keV we find $\Delta x \sim 300$ cm and clearly collisional absorption is not strong near the plasma center. However, the first term of Eq. (7b) will yield Im $k_x = (n_z/2)(\omega_{pe}/c)(\nu_{eff}/\omega)$. We can estimate that $\int 2\mathrm{Im}k_x dx$ for the edge plasma in Alcator A is about 0.08 for $n_z = 3$, $n_e = 3 \times 10^{13}\,cm^{-3}$, $T_e = 10$ eV and $\Delta x = 1$ cm being the width of the low temperature edge. While this absorption is weak, any process that would repeatedly scatter the lower hybrid wave into the edge could eventually cause a significant power loss there.

The last terms of Eq. (7a) and (7b) are respectively the perpendicular ion Landau damping and electron Landau damping terms. Both are exponentially dependent on the ratio of the wave phase velocity to the thermal velocity; specifically, electron Landau damping would become dominant when $c/(v_{Te} n_z) < 3$. In Alcator A $T_e \gtrsim 1$ keV, and electron Landau damping becomes important for $n_z \sim 5$. As will be shown below we would not expect to efficiently launch such high values of n_z in Alcator A and we would not expect to produce direct electron heating.

Similarly, ion heating would require k_x large so that $\omega/(k_x v_{Ti}) \sim 1$. This large k_x and ion heating can only occur when the plasma density is near the lower hybrid mode conversion value.

Figure (1) plots both k_x and $P(x) = P_o \exp(-2 \int \mathrm{Im} k_x dx)$, where P_o is the incident rf power, for the parabolic density profile of Alcator A. $\bar{n}_e$ is the line averaged density and generally $n_{eo} = 1.5\ \bar{n}_e$, where n_{eo} is the central electron density. T_e and T_i vary like $\exp(-r^2/r_T^2)$ where $r_T = 6$ cm. $f = 2.45$ GHz and $n_z = 5$. k_x is found from the electrostatic dispersion relation in a slab geometry that does not include toroidal or cylindrical effects; as a result k_z = constant. In Fig. (1a) $\bar{n}_e = 2 \times 10^{14} \mathrm{cm}^{-3}$, $T_e = 900$ eV, $T_i = 800$ eV, the ions are deuterium, and only the ion damping terms are included. Mode conversion occurs near the plasma center, and just in front of it k_x becomes large enough so that the wave is absorbed. Figure (1b) is identical to Fig. (1a), except that $\bar{n}_e$ is reduced to $1.6 \times 10^{14} \mathrm{cm}^{-3}$. Ion absorption still occurs even though the mode conversion layer is absent, illustrating that wave absorption can occur at densities slightly below the mode conversion density, n_{LH}. We note below that $n_z = 5$ is a higher value of n_z that we expect to launch with the Alcator A waveguide array. For $n_z = 3$, which should be characteristic of the Alcator A wave spectrum, $n_{LH} \approx 4.3 \times 10^{14} \mathrm{cm}^{-3}$ from which we would expect ion heating at $\bar{n}_e \sim 2.9 \times 10^{14} \mathrm{cm}^{-3}$.

Figure (1c) graphs k_x and $P(x)$ for $\bar{n}_e = 1.2 \times 10^{14} \mathrm{cm}^{-3}$, $T_e = 1100$ eV, $T_i = 800$ eV, deuterium, and here both the electron and ion damping terms are included. We see that the wave is

strongly absorbed, in this case due to electron Landau damping; the ion damping is negligible. We would therefore expect some electron heating at densities below n_{LH} when $T_e > 1$ keV and $n_z \sim 5$. Again, we note that for the expected $n_z \sim 3$ no electron heating should occur for $T_e \sim 1$ keV.

B. Waveguide - Plasma Coupling Theory

We see that the lower hybrid waves that can propagate into the plasma have $n_z > 1$; since waves with $n_z > 1$ do not propagate in vacuum, special slow wave structures must be used to launch these waves. It has been demonstrated[27] and theoretically predicted[28-31] that arrays of variably phased waveguides or "grills" can be successfully employed to couple microwave power into lower hybrid waves having $n_z > 1$ in magnetized plasmas. The basic geometry considered theoretically is shown in Fig. 2, where we have N waveguides of width b at positions $z_1, z_2, \ldots z_N$, each excited by an incident mode having $\vec{E} \| \vec{B}_o \| \hat{z}$. The density gradient is in the $\hat{x}$ direction with $\omega_{pe}^2 = \omega^2(1 + x/L)$, where ω is the incident radiation angular frequency. If the amplitudes of the incident and reflected waveguide modes are α_n and β_n respectively, the following system of equations is obtained:[29,30]

$$\beta_{mq} + \sum_{p=1}^{N} \sum_{n=0}^{\infty} K_{mq,np} \beta_{np} \qquad (9)$$

$$= \alpha_{mq} - \sum_{\substack{p=1 \\ n=0}}^{N} K_{mq,np} \alpha_{np}$$

where

$$K_{mq,np} = \frac{4\pi k_m}{b(1 + \delta_{m,0})} \int_{-\infty}^{\infty} \frac{F_{np}(k_z) F_{mq}^{*}(k_z)\, dk_z}{Z(k_z)\, k_x}$$

$$k_x = \begin{cases} \sqrt{\omega^2/c^2 - k_z^2} & |n_z| < 1 \\ i\sqrt{k_z^2 - \omega^2/c^2} & |n_z| > 1 \end{cases}$$

$$k_m = \begin{cases} \omega/c & m = 0 \\ i\sqrt{m^2\pi^2/b^2 - \omega^2/c^2} & m \neq 0 \end{cases}$$

$$Z(k_z) = \begin{cases} i\, \dfrac{J_{1/3}(\frac{2}{3}\xi_o^{3/2}) + J_{-1/3}(\frac{2}{3}\xi_o^{3/2})}{J_{2/3}(\frac{2}{3}\xi_o^{3/2}) - J_{-2/3}(\frac{2}{3}\xi_o^{3/2})} & |n_z| < 1 \\ \dfrac{I_{1/3}(\frac{2}{3}\xi_o^{3/2}) + e^{-\pi i/3} I_{-1/3}(\frac{2}{3}\xi_o^{3/2})}{I_{-2/3}(\frac{2}{3}\xi_o^{3/2}) + e^{-\pi i/3} I_{2/3}(\frac{2}{3}\xi_o^{3/2})} & |n_z| > 1 \end{cases}$$

$$F_{np}(k_z) = \frac{ik_z}{2\pi} \frac{e^{-ik_z z_p}}{\frac{n^2\pi^2}{b^2} - k_z^2} \left(1 - (-1)^n e^{-ik_z b}\right)$$

and where $\xi_o = \left(\frac{\omega L}{c}\right)^{2/3} |1 - n_z^2|^{1/3}$. Equation (9) takes into account that waves with $|n_z| < 1$ are reflected at $x = L$ where $\omega = \omega_{pe}$, whereas waves with $|n_z| > 1$ tunnel between $x = 0$ and $x = L$, but thereafter propagate into the plasma. This treatment neglects the conversion of $|n_z| > 1$ waves into whistler modes for $x > L$ when $|n_z| < n_{za}$. Given the propagating incident modes α_{np} $(n = 0)$, Eq. (9) can be truncated and solved for the β_{np}'s, and we find that reflection coefficients less than 50% can be achieved for suitable values of ∇n and waveguide array phasing. Figure (3a) shows the global reflectivity as a function of ∇n for the two waveguide array employed on the Alcator A experiment. Here $b = 1.275$ cm, $\omega = 2\pi \times 2.45$ GHz, and there is a 0.09 cm septum separating the waveguides. Equation (9) predicts a minimum in reflectivity at $\nabla n \sim 10^{13} \text{cm}^{-4}$ when $\Delta\phi$, the phase difference between the guides, $= \pi$.

Once the β_{np}'s are solved for, the n_z power spectrum of lower hybrid waves can be found. We obtain

$$P(n_z) = C \frac{|\sigma^2(k_z)|}{|k_x|} \text{Im} \frac{1 - Z(k_z)}{1 + Z(k_z)} \tag{10}$$

where

$$\sigma(k_z) = \left(\frac{2Z(k_z)}{1 + Z(k_z)}\right)^{-1} \sum_{p=1}^{N} \sum_{n=0}^{N} (\alpha_{np} + \beta_{np}) F_{np}(k_z)$$

and C is a constant which is independent of k_z. Figure (3b) graphs the predicted $P(n_z)$ and $\int_1^{n_z} P(\xi)d\xi$ for the Alcator A double waveguide array with L = 0.05 cm for $\Delta\phi = 0$ and $\Delta\phi = \pi$. For $\Delta\phi = \pi$ the $P(n_z)$ spectrum is broad, characterized by a width $n_z \sim 3$, and has about 60% of the power accessible with $n_z > n_{za} \sim 2$. For $\Delta\phi = 0$ less than 10% of the power is accessible; in fact over 80% of the power has $n_z < 1.5$ and would only penetrate the plasma edge with $r > 9$ cm in Alcator A. We would therefore expect a marked change in central heating with $\Delta\phi = \pi$ over $\Delta\phi = 0$.

The reflectivities and power spectra calculated above can be altered by other effects. It has been suggested that corrugations in the vacuum vessel wall, such as those present in Alcator A due to the bellows, can strongly affect the emitted power spectra[32]. However, in Alcator A the corrugations are more than one vacuum wavelength from the waveguide array; it has been shown that in this case the effect of the bellows on $P(n_z)$ is negligible[33]. Another strong effect that has been neglected is the mode conversion of lower hybrid waves into whistler waves for $1 < n_z < n_{za}$. This effect changes $P(n_z)$ by introducing eigenmodes with resonance effects in this portion of the spectrum. However, it has been shown[34] that the proportion of the wave power in this inaccessible part of the n_z spectrum does not change from that expected by neglecting the whistler modes; therefore strong changes in central plasma heating should be observable when changing from $\Delta\phi = \pi$ to $\Delta\phi = 0$ for a two waveguide system.

Finally, this theory neglects any backscatter caused by turbulence or parametric instabilities of the lower hybrid wave

power into the waveguide mouth. It has been predicted that any such backscatter will tend to bounce off the waveguide array with a reflected n_z power spectrum peaked at multiples of $(c/\omega)(\pi/b)$[35]. Thus, any backscatter occurring near the waveguide mouth might exhibit itself as a $P(n_z)$ having a peak at $k_z = \pi/b$ or, for the Alcator A parameters, having a peak at $n_z \sim 5$. However, this effect would depend on the backscattering occurring close enough to the waveguide mouth so that the backscattered lower hybrid waves impinge on the waveguides.

C. Parametric Instabilities

Parametric instabilites have been previously observed in lower hybrid heating experiments on tokamaks[2,7,9] and would be expected to occur on the Alcator A experiment which had rf power densities up to 4.5 kW/cm^2 at the waveguide mouth. These instabilities are driven by a pump wave $\vec{E}_o \cdot \cos(\omega_o t - \vec{k}_o \cdot \vec{x})$ which in the dipole approximation ($\vec{k}_o = 0$) results in a parametric coupling coefficient[36-38]

$$\mu = \frac{e}{m}\left[\left(\frac{E_{oz}k_{\parallel}}{\omega_o^2} + \frac{\vec{E}_{o\perp}\cdot\vec{k}_{\perp}}{\omega_o^2 - \omega_{ce}^2}\right)^2 + \frac{[(\vec{E}_{o\perp}\times\vec{k}_{\perp})\cdot\hat{z}]^2\,\omega_{ce}^2}{(\omega_o^2 - \omega_{ce}^2)^2\,\omega_o^2}\right]^{1/2} \tag{11}$$

where $\vec{B}_o \parallel \hat{z}$, and $k_{\parallel}$, $k_{\perp}$ are the components of $\vec{k}$ of the decay waves. The $E_{oz}k_{\parallel}$ term dominates at low densities and drives lower hybrid decay waves that propagate in the same direction as the pump wave, whereas the $\vec{E}_o \times \vec{k}_{\perp}$ term arises from the $\vec{E}_o \times \vec{B}$ drift of the electrons and drives waves primarily with $\vec{k}_{\perp}$ perpendicular to $\vec{k}_{\perp o}$. μ couples high frequency lower hybrid or hot ion Bernstein sideband modes and low frequency ion cyclotron, ion acoustic or quasi-modes. It is easy to show that the $E_{oz}k_{\parallel}$ term will dominate for densities such that $\omega_{pe}^2 < \omega_o\omega_{ce}$, or for the Alcator A experiment for $n_e < 5 \times 10^{12}$cm^{-3}; above this density the $\vec{E}_o \times \vec{k}_{\perp}$ term would

dominate for $\vec{k}_\perp$ perpendicular to $\vec{k}_{\perp o}$. What follows is a brief qualitative discussion of these parametric processes; in general the exact growth rates and thresholds require a numerical treatment.[36,37]

The $\vec{E}_{o\perp} \times \vec{k}_\perp$ term will drive lower hybrid waves and ion cyclotron waves. Near the plasma edge the low frequency ion cyclotron waves will be lightly damped (in the dipole approximation $|\vec{k}_o| << |\vec{k}|$) for $\omega_o/k_{||} v_{Te} \gtrsim 5$ and for $n \sim 1$ (where $\omega = n\omega_{ci}$). For higher values of n the low frequency waves will be strongly electron Landau damped quasimodes at the plasma edge. Near the plasma center the low frequency ion modes will be strongly damped whenever $\omega \lesssim 2\omega_{lh}$, where $\omega_{lh}^2 = \omega_{pi}^2/(1 + \omega_{pe}^2/\omega_{ce}^2)$. For these parametric processes the finite extent pump threshold will be higher than the inhomogeneous plasma threshold, since $L_{ox} \equiv$ width of the resonance cone in the x direction $= L_{oz}(m_e/M_i)^{1/2}(\omega_o^2/\omega_{lh}^2 - 1)^{1/2} << L_n$, which is the density scale length. This threshold is[37]

$$\frac{\gamma^2}{v_{2x}\Gamma_1} L_{ox} > \pi \qquad (12)$$

where γ is the growth rate, v_{2x} is the group velocity of the lower hybrid wave in the x direction, and Γ_1 is the low frequency wave damping rate. Here the k_x of the decay wave is $\sim 2\pi/L_{ox}$.

Near the Alcator A edge plasma this results in a threshold power $\sim$ 10 kW for $n_e = 5 \times 10^{13} cm^{-3}$, T_e = 200 eV, B = 60 kG, deuterium, $k_{\parallel} \simeq 4/cm$, $n_{\parallel o} = 3$, and for waveguide dimensions L_z = 1.275 cm and L_y = 8.13 cm. We thus expect to excite this instability at the Alcator A lower hybrid heating power of $\sim$ 100 kW. However, the decay into ion cyclotron waves at higher harmonics of ω_{ci} will be strongly electron Landau damped. In this case the finite pump length threshold will be $\gamma L_{oz}/v_{\perp z} > \pi$[37] and is an order of magnitude higher than the threshold of Eq. (17). However near the mode conversion layer where $\omega_o/\omega_{1h} \gtrsim 1$ the WKB enhancement factor raises E_{ox} and thereby lowers the threshold. Furthermore, near $\omega \sim \omega_{1h}$ decay into the hot ion mode is possible since here $v_{\perp z}$ is much smaller than near the edge. We would therefore expect that decay into modes having frequencies $\omega_o - \omega_{ci}$ and ω_{ci} would be possible near the plasma edge; results from detailed numerical calculations of growth rates in homogeneous plasmas also indicate that for $\omega_o/\omega_{1h} >> 1$ only the first few ion cyclotron harmonics will be excited parametrically.[36,37] Decay into modes with frequencies $\omega_o - n\omega_{ci}$ for $n >> 1$ would only be possible near the mode conversion layer in the plasma interior. It has been shown numerically that the latter decay results in a frequency spread of the lower hybrid wave sideband $\Delta\omega \sim 0.3\omega_o$.[37]

The $E_{o\parallel} k_{\parallel}$ term of μ will drive lower hybrid waves that can propagate parallel to the pump wave.[39,40] This feature greatly reduces the inhomogeneous plasma and finite pump length thresholds. This decay will be into lower hybrid waves and ion acoustic waves. In a homogeneous plasma this parametric process has a dispersion relation

$$\varepsilon_I(\omega) = \beta \left[\frac{1}{\varepsilon(\omega_-)} + \frac{1}{\varepsilon(\omega_+)} \right] \qquad (13)$$

where

$$\beta = \frac{v_o^2}{c^2} k_{||}^2 c^2 / (\omega_o^2 \lambda_D^4)$$

$$\varepsilon(\omega) = \left(k_x^2 + k_{||}^2 \left(\frac{\omega_{pe}^2}{\omega(\omega + i\nu_{ei})} - 1 \right) \right)$$

$$\varepsilon_I(\omega) = - k_x^2 \left(1 + \frac{\omega_{pi}^2}{\omega_{ci}^2} \right) + k_{||}^2 \left[\frac{\omega_{pi}^2}{k_{||}^2 v_{Te}^2} Z' \left(\frac{\omega}{k_{||} v_{Te}} \right) - 1 - \frac{1}{k_{||}^2 \lambda_{De}^2} \right]$$

$$v_o = \frac{eE_{oz}}{2m_e \omega_o}$$

$v_{Ti}^2 = 2\ T_i/m_i$, $\vec{k}_o \tilde{=} 0$, $k_{||}$ is the decay wavevector parallel to B_o, and k_x is perpendicular to $\vec{B}_o$, $\omega_- = \omega - \omega_o$, $\omega_+ = \omega + \omega_o$ and $\vec{E}_o(t) = E_{oz} \cos \omega_o t$. ν_{ei} is the effective electron ion collision frequency. We can find the threshold for this instability by letting $\omega = \omega_R + i\gamma$ with $\gamma = 0$ and ignoring the ω_+ upper sideband. Letting $T_e >> T_i$ and assuming

Fig. 49. (a) P_T(kw) and τ_N (msec) vs. T_T(keV) for E_{max} = 100 keV and the parameters of Fig. 48. (b) P_T(kW), τ_N(msec) and δ vs. E_{max}(keV) for T_T = 15 keV and the parameters of Fig. 48.

that both upper and lower sidebands are weakly damped, we obtain

$$\frac{v_o^2}{v_{Te}^2} = \sqrt{\frac{\pi}{2}}\ \frac{\nu_{ei}}{\omega_o}\left(\frac{T_e}{T_i}\right)^{3/2} e^{-T_e/(2T_i)} \qquad (14)$$

Near enough to the waveguide so that $2/3\ \xi^{3/2} < 1$, where $\xi = (\omega L/c)^{2/3}\ |n_z^2 - 1|^{1/3}\ (x/L - 1)$, the electric field will essentially be that at the waveguide mouth and $E_{oz}^2 \simeq 16\pi\ P/(L_y L_z\ c\ (1 - \pi^2 c^2/\omega_o^2 L_y^2)^{1/2})$. $\xi^{3/2} \lesssim 1$ is equivalent to $\Delta x \lesssim L^{1/3}\lambda_o^{2/3}/(2\pi n_z)^{2/3}$, where Δx is the distance from the waveguide to the instability region and for $L \sim 10^{-1}$cm, $\Delta x \sim 0.5$ cm. Equation (14) would then yield a threshold of $P > 20$W for $T_e/T_i = 10$, $T_e = 10$ eV, $n_e = 1 \times 10^{13}\text{cm}^{-3}$ and the Alcator A parameters. Further from the waveguide the WKB relations would fix $E_z^2 \simeq (P/L_y L_z)(8\pi/c)\ n_{\|}\ \omega/\omega_{pe}$ and we would obtain a threshold of $P > 600$W for the same parameters. Of course, both thresholds decrease as the density is lowered, and thus decay is favored toward the plasma edge. For $T_e = T_i$ the low-frequency wave is heavily damped and Eq. (13) requires a numerical solution. Noting that at threshold $\omega_i = 0$ we can obtain the condition

$$-\varepsilon_i(\omega)\left[\varepsilon_{Ii}(\omega) + \varepsilon_{Ir}^2(\omega)/\varepsilon_{Ii}(\omega)\right] = 3 \qquad (15)$$

where the subscript i,r denotes imaginary or real part. This result is a minimum threshold at $\omega \simeq 1.6\ k_{\|} v_{Ti}$ and we

obtain $v_o^2/v_{Te}^2 \sim 0.4\ \nu_{ei}/\omega_o$, which result in a threshold P > 40W near the waveguide mouth. We see that all these thresholds are far below the 100 kW of rf power of the Alcator A experiment.

Additional threshold conditions for this decay must be satisfied due to the finite extent of the pump in the $\hat{z}$ direction and due to the plasma inhomogeneity in the $\hat{x}$ direction. We can define the unit vector $\hat{\xi}$ along the pump wave resonance cone and $\hat{\eta} \perp \hat{\xi}$. Then

$$\xi_x = (\omega_o/\omega_{pe}) \Big/ \sqrt{1 + \omega_o^2/\omega_{pe}^2} \qquad (16)$$

$$\xi_z = -\left(1 + \omega_o^2/\omega_{pe}^2\right)^{-1/2}$$

$$\eta_x = \omega_{pe}/\omega_o \Big/ \sqrt{1 + \omega_{pe}^2/\omega_o^2}$$

$$\eta_z = \left(1 + \omega_{pe}^2/\omega_o^2\right)^{-1/2}$$

$$L_\eta \tilde{=} L_z\ \omega_o/\omega_{pe}$$

where L_z is the waveguide extent along $\vec{B}_o$ and L_η is the width of the resonance cone We then find that, ignoring plasma inhomogeneity, that the decay wave amplitudes vary as $e^{K\eta}$, where[40]

$$K = \frac{-\nu_{2\eta}\Gamma_1 - \nu_{1\eta}\Gamma_2 + \sqrt{(\nu_{2\eta}\Gamma_1 + \nu_{1\eta}\Gamma_2)^2 - 4\nu_{1\eta}\nu_{2\eta}(\Gamma_1\Gamma_2 - \gamma_o^2)}}{2\,\nu_{1\eta}\nu_{2\eta}} \qquad (17)$$

where

$$v_{1\eta} = \frac{\omega_o}{\omega_{pe}}\sqrt{\frac{T_e}{m_i}}$$

$$v_{2\eta} = -\frac{\omega_o}{\omega_{pe}}\sqrt{\frac{T_e}{m_i}} = -v_{1\eta}$$

Γ_1 and Γ_2 are the time decay constants of the low frequency and lower sideband waves, and $v_{1\eta}$, $v_{2\eta}$ are their group velocities in the $\hat{\eta}$ direction. Since $\gamma_o^2 >> \Gamma_1\Gamma_2$ and $\gamma_o > \Gamma_1$ we have the condition for instability

$$KL_\eta \approx \frac{\gamma_o}{v_{1\eta}} L_\eta > 1 \qquad (18)$$

For $n_e = 10^{13}cm^{-3}$, $T_e = 10$ eV, $k_\parallel = 2.6$ cm^{-1} and $L_z = 2.6$ cm, this is satisfied for P > 1W, which is much lower than the available 100 kW of power.

The inhomogeneous plasma threshold condition must be satisfied in the $\hat{x}$ direction. The group velocities in the $\hat{x}$ direction and mismatch term $\kappa' = d/dx\ (k_{ox} - k_{1x} - k_{2x})$ are

$$v_{1x} \approx -\sqrt{\frac{T_e}{m_i}}\ \frac{\omega_s^2}{\omega_{ci}^2}\ \frac{\omega_{pe}}{\omega_o} \qquad (19)$$

$$v_{2x} \simeq \frac{\omega_o^2}{k_{||}\omega_{pe}}$$

$$\kappa' = k_x/2L$$

where at the location of the decay $n(x) = n_o(1 + x/L)$ and $\omega_s = k_{||}(T_e/m_i)^{1/2}$. Letting $\Gamma_1 = \delta\omega_s$, if the low frequency wave is weakly damped and $\delta \sim 10^{-2}$, $\gamma_o > \Gamma_1 \sqrt{v_{2x}/v_{1x}}$ and the inhomogeneous plasma threshold is[41]

$$\frac{2\pi\gamma_o}{v_{1x}v_{2x}\kappa'} > 1 \qquad (20)$$

which for $T_e = 10$ eV, $n_e = 10^{13}$cm^{-3}, L = 2 cm, and $k_{||} = 2.6$ cm^{-1} is satisfied for $P_T > 15$W. Thus for weakly damped waves we easily excite this instability. For strongly damped waves, $\delta \sim 1$, and $\gamma_o < \Gamma_1 \sqrt{v_{2x}/v_{1x}}$. It has been shown that a noise source at x = 0 will be amplified by this instability as[42]

$$a(x) = a_o \exp\left\{ - \Gamma_2 x/v_{2x} + (i\gamma_o^2/|v_{1x}v_{2x}\kappa'|)\left[\ln(x/x_c + i) - i\pi/2\right]\right\} \qquad (21)$$

where $x_c = |\Gamma_1/(v_{1x}\kappa')|$ and a_o is noise source amplitude at $x = 0$. For $\delta \sim 1, x_c \sim 3L$ and is several centimeters long. The condition for a convective decay in the plasma edge in a distance $\ell \sim 2$ cm will then be

$$\frac{2\gamma_o^2 \ell}{v_{2x}\Gamma_1} > 1 \qquad (22)$$

which for the above conditions and $\delta \sim 1$ is satisfied for $P_T > 1.5$ kW. We therefore expect to be able to excite this parametric process in the Alcator A plasma edge at full power $P_T \sim 100$ kW, although the thresholds may be increased to several kilowatts if the low frequency wave is heavily damped.

Finally, it should be noted that it has been predicted[43] that drift waves can be parametrically excited or suppressed by lower hybrid waves. It has been experimentally observed[44] that drift waves can be enhanced by lower hybrid waves at rf powers much lower than the thresholds of other parametric effects. Intense density fluctuations having $\Delta n/n \sim 1$ have been observed in the Alcator A edge plasma[45], although their physical model has not been determined. Any parametric excitation or suppression of these fluctuations at the plasma edge could significantly modify or lower the parametric threshold previously mentioned. These density fluctuations have very

small $k_{||}$ [45] and any scattering from them would not change the $\vec{k}_{||}$ of the lower hybrid wave; rather it would rotate its $\vec{k}_{\perp}$ about B_o.

D. Lower Hybrid Wave Scattering at the Plasma Edge

The previously mentioned parametric decay driven by the $E_{o||} k_{||}$ term can cause an instability which excites higher $k_{||}$ lower hybrid daughter waves near the plasma edge. If a significant fraction of the pump is converted into these waves parametrically, an effective upshift in the $k_{||}$ wave spectrum radiated by the waveguide can occur. This decay process may reflect lower hybrid waves back along the resonance cone into the waveguide mouth; the waves reflected from the waveguides will then be characterized by $k_{||} \sim \pi/b$ as shown above.

Scattering or parametric excitation by density fluctuations near the plasma edge would not change the $k_{||}$ of the lower hybrid waves. Such scattering from an ambient level of density fluctuations has been predicted[46-49] and observed experimentally[50] in a small linear machine. Ott[49] has derived a 90° scattering length $\ell_{90°}$

$$\ell_{90°} \approx \frac{\pi}{4}^{3/2} \frac{\omega^2 \omega_{ce}^2}{\omega_{pe}^4} \left\langle \left(\frac{\Delta n}{n}\right)^2 \right\rangle^{-1} \frac{1}{\xi_o} \qquad (23)$$

where ξ_o is the width of the density fluctuation $k_{\perp}$ spectrum and is $\sim 10\ cm^{-1}$.[45] For $n_e = 3 \times 10^{13} cm^{-3}$, $(\Delta n/N) \sim 0.5$ and $B_T = 60$ kG, $\ell_{90°} \sim 2 \times 10^{-2} cm$. However, the weak turbulence approximation used to obtain Eq. (23) is only valid for

$\ell_{90°} > (k_{\parallel}^2/\xi_o^3)\ \omega_{pe}^2/\omega^2 \sim 1$ cm for $n_{\parallel} \sim 3$ and $n_e = 3 \times 10^{13} cm^{-3}$. Thus for the large values of $\Delta n/N$ present in Alcator A the weak turbulence approxmation of Eq. (23) breaks down. Nevertheless, substantial scattering of the lower hybrid waves at the plasma edge due to density fluctuations could occur in Alcator A.

Such scattering could manifest itself as an increased level of lower hybrid surface waves and therefore an increased absorption at the plasma edge. Recently it has been pointed out that in toroidal coordinates such poloidal scattering of the lower hybrid waves could lead to increased accessibility of the wave to the plasma center.[51] Here we will examine this effect in a cylindrical coordinate system in which the m poloidal number is conserved. Toroidal effects will cause m to vary as the wave propagates inward and therefore may modify these results.

At the plasma edge a lower hybrid wave has a wavevector $\vec{k} = (k_r, k_p, k_\phi)$, where k_r is the radial component of the wavevector, k_p the poloidal component and k_ϕ the toroidal component, which is a constant. Initially k_p is small due to the slight difference in angle between $\vec{B}_o$ and $\hat{\phi}$ caused by the poloidal $\vec{B}$ field. $\vec{k}_\perp$, which is the wavevector perpendicular to the local $\vec{B}_o$, initially has two components $k_{\perp r} \simeq k_{\perp o}$ and $k_{\perp\perp} \simeq 0$, where $k_{\perp r}$ is the component of $\vec{k}_\perp$ in the radial direction, and $k_{\perp\perp}$ is that component in the poloidal plane ($k_{\perp\perp} \mp k_p$). $\vec{k}_{\perp\perp}$ is the component of $\vec{k}$ parallel to the total magnetic field B_o. This is illustrated in Fig. 4. Note

that $k_{\perp o} \simeq k_{||}\ \omega_{pe}/\omega >> k_{||}$, and that in cylindrical coordinates $k_p = m/r$, where m = constant. We then write down the equations relating (k_r, k_p, k_ϕ) and $(k_{\perp r}, k_{\perp\perp}, k_{||})$:

$$\frac{m}{r} = k_p = - k_{\perp\perp} \cos\theta + k_{||} \sin\theta \qquad (24)$$

$$k_\phi = k_{\perp\perp} \sin\theta + k_{||} \cos\theta$$

and

$$k_{\perp\perp} = k_\phi \sin\theta - \frac{m}{r} \cos\theta$$

$$k_{||} = k_\phi \cos\theta + \frac{m}{r} \sin\theta$$

where $\tan\theta = B_{po}/B_{To}$, and B_{po} is the poloidal field and B_{To} is the toroidal field. Initially $k_{\perp\perp} \simeq 0$, $k_{\perp r} \simeq k_{\perp o}$, $k_{||} \simeq k_\phi$, and $k_p \simeq 0$. If at the plasma edge we rotate $k_\perp$ about B_o, then $k_{\perp\perp} = k_{\perp o}\alpha$ and $k_{\perp r} = k_{\perp o}(1 - \alpha^2)^{1/2}$, where for a 90° rotation $\alpha = 1$. Using m and k_ϕ conservation, and expanding to first order in $r/(Rq(r))$, we obtain

$$k_{||}(r) = k_{||}(a)\ \left(1 + \frac{\omega_{peo}}{\omega}\ \alpha\ \frac{a}{R}\ \left(\frac{1}{q(a)} - \frac{1}{q(r)}\right)\right) \qquad (25)$$

where a is the limiter radius, R is the major radius and ω_{peo} =

$\omega_{pe}(a)$. This second term in Eq. (25) can enhance $k_{||}$ by a factor of 2 or 3 by the time the wave propagates into the plasma center for $\alpha \sim 1$. This effect could cause an effective upshift in $k_{||}$ and radically change the expected plasma heating.

This upshift in $k_{||}$ is illustrated in Fig. 5. In Fig. (5a) $k_{\perp r}$, $k_{\perp\perp}$, and $k_{||}$ are graphed vs. r for typical Alcator A plasma parameters and for $\alpha = 0$. $k_{||}$ is a constant and the wave propagates into the plasma center with no absorption. Fig. (5b) is the same graph with $\alpha = -0.707$. $k_{||}$ now increases as the wave propagates inward; near r = 4.5 cm $k_{\perp}$ becomes large enough so that the wave is absorbed by perpendicular ion Landau damping. The density at which wave absorption occurs is much lower than that expected from letting $\alpha = 0$. Fig. (5c) shows the same graph for $\alpha = 0.707$. Now $k_{||}$ decreases as the wave propagates inward, resulting in a mode conversion into a whistler wave at r = 7.5 cm. However, this whistler would propagate back into the plasma edge. There its $\vec{k}_{\perp}$ could presumably be rotated to $\alpha < 0$ and it could subsequently propagate into the plasma interior.

This upshift in $k_{||}$ could also allow lower hybrid waves that are not otherwise accessible to the plasma center to reach there. We can expand Eq. (3) near the plasma edge to find the n_{zc} at which the lower hybrid wave will mode convert into a whistler wave

$$n_{zc} \simeq 1 + \frac{\omega_{pi}}{\sqrt{\omega_{ce}\omega_{ci}}} \qquad (26)$$

where at the plasma edge $\omega_{pi}^2/\omega^2 << 1$. Thus n_{zc} and $n_{||}$ both increase as n_e increases for $\alpha < 0$. If $n_{||}$ increases faster than n_{zc}, the lower hybrid wave will avoid the whistler mode conversion in the plasma interior. Figure 6 shows the effect for typical Alcator A plasma conditions. In Fig. (6a) $n_{||}(a) = 1.3$ and $\alpha = 0$. At $r \simeq 8.5$ the lower hybrid wave mode converts into a whistler wave. For $\alpha = -0.3$ and $n_{||}(a) = 1.3$ the wave penetrates, as shown in Fig. (6b). Thus, a poloidal rotation of only 17° can change a surface wave into a penetrating wave and even waves with $n_{||} < n_{zc}$ may penetrate to the plasma center.

Finally, a crude prediction of the effect of strong poloidal scattering can be made. We can launch a wavepacket with a specific $k_{||}$ spectrum at the plasma edge, and then isotropize $\vec{k}_\perp$ about $\vec{B}$ at the edge for each value of $k_{||}$. Each $(k_{||}(a), \alpha)$ component can then be followed as it propagates inward and is either absorbed or reflected. The local $k_{||}$ spectrum at each radius and the radial profile of the power deposition in the plasma can be calculated. The results of such a calculation as shown in Fig. 7. Figure (7a) shows the absorbed power P_{ABS} vs. r for both electrons and ions for $\bar{n}_e = 1.6 \times 10^{14} cm^{-3}$, deuterium, $B_T =$ 80 kG, $T_e = 1$ keV, $T_i = 800$ eV, $I_p = 150$ kA and for an initial Brambilla spectrum generated by two out of phase waveguides having a width b = 1.275 cm. (Note that P_{ABS} is the power absorbed per unit length; the power absorbed per unit volume would be P_{ABS}/r). 40% of the initially incident power is absorbed by the plasma on the first pass, 90% of which is absorbed by ions. At least half of the incident power will have $\alpha > 0$ and be

reflected as whistler waves at the plasma surface; however on subsequent passes this power can be rescattered into $\alpha < 0$ and actually heat the plasma. This scattering and isotropization in α at the plasma edge result in ion heating at a lower density than expected from the Brambilla $k_{||}$ spectrum. Figures (7b), (c), and (d) shows the $k_{||}$ power spectrum at r = 10 cm, 5 cm, and 2 cm. While at the edge the spectrum is essentially a "Brambilla" spectrum, it spreads to larger $k_{||}$ as the waves propagate inward. Finally, at r = 2 cm the components having $n_{||} > 4.5$ are damped out.

Finally, Fig. (8) shows a P_{ABS} vs. r profile for $\bar{n}_e = 2 \times 10^{14}$, deuterium, $B_T = 62$ kG, $T_e = 1$ keV, $T_i = 800$ eV, $I_p = 150$ kA and two in phase waveguides having b = 1.275 cm. For in phase waveguides no heating would be expected for a Brambilla spectrum; however due to the $k_{||}$ upshift 22% of the initial power is absorbed by the plasma, 95% of which is absorbed by ions. Thus this poloidal rotation can to a certain extent cause waveguide phase independendent heating. This calculation predicts phase independent central ion heating for the Alcator A parameters in deuterium for $\bar{n}_e \sim 1.5 \times 10^{14} cm^{-3}$ and $B_T = 60$ kG. In the absence of such a rotation ion heating would only occur for $\bar{n}_e > 3 \times 10^{14} cm^{-3}$. For $\bar{n}_e \geq 2.5 \times 10^{14} cm^{-3}$ phase independent heating still is predicted to occur, but at the plasma exterior. For $\bar{n}_e < 1 \times 10^{14} cm^{-3}$ electron heating should occur, but only for 0, π waveguide phasing. Thus this model predicts that heating significantly different than the Brambilla prediction will occur if a substantial rotation of $\vec{k}_\perp$ occurs at the plasma edge. Again, we note that additional effects due to toroidicity could occur.[51]

E. Energetic Ion Confinement

At densities near those defined by Eq. (6), the mode conversion density, $k_\perp$ and $k_\perp \rho_i$ become large, and the lower hybrid wave becomes strongly damped by the ions. If the phase coherence between the wave and ion is destroyed over a cyclotron period, the ions would behave as if they were unmagnetized ($\omega >> \omega_{ci}$) and the ion Landau damping velocity space quasilinear diffusion would result. At large $k_\perp \rho_i$ and $E_\perp$ it has been proposed that stochastic heating of the ions may result[52-54]. It has been further proposed that above this stochasticity threshold the ergoticity of the ion motion will produce a decorrelation between the ion motion and wave and result in the ion Landau damping quasilinear diffusion.[55] Such diffusion is predicted to result in perpendicular energetic ion tails extending to energies many times the bulk ion temperature. Such energetic ion tails have been observed experimentally in the Alcator A experiment and will be discussed in Sections III and IV. Here we note that these ion tails must be confined in order that the rf power, which is first transferred to energetic ions, be deposited into the bulk plasma as these ions slow down due to collisions.

These energetic ions can be lost in tokamaks through large excursion banana orbits which hit the plasma limiter. Such losses and orbits have been calculated previously[56,57] and what follows is an application to the conditions of Alcator A. In Alcator A the plasma current can be approximated by a radial profile

$$J_p(r) = J_o \exp(-3r^2/(2r_T^2)) \qquad (27)$$

where

$$J_o = \frac{B_T c}{1.8\ \pi R}$$

$$r_T(\text{cm}) = 1.2\ [I_p(\text{kA})/B_T(\text{T})]^{1/2}$$

Here J_o is the central current density and is fixed by the condition $q(0) = 0.9$. As the plasma current is increased, the current density profile broadens as r_T increases. Noting that in Alcator A $Z_{eff} \simeq 1$, $J_p(r) \propto T_e^{3/2}(r)$. This current density profile is used to calculate the poloidal flux function from which the loss orbits shown below are taken.

Figure 9 shows the boundaries in velocity space between confined ion orbits and ion orbits that strike the limiter. Here R = 54 cm, a = 10 cm, B_T = 60 kG, I_p = 150 kA, and we consider deuterium ions on the tokamak midplane. Each curve shows the confinement boundaries at a given minor radius; the region above the curve contains the unconfined orbits. Only ions having velocities antiparallel to the plasma current are shown, as the confinement for parallel ions is much better. We note that a purely perpendicular ion can be contained in Alcator A in this regime at an energy of 96 keV

at r = 3 cm. However, above an energy of 15 keV (the minimum unconfined energy) such a perpendicular ion would rapidly be lost by pitch angle scattering into the unconfined region. The minimum unconfined energy occurs at a $v_{||}/v \sim 0.4$; perpendicular ions with energy above 15 keV will be lost in a time $t_{loss} \sim 4 |v_{||}/v|^2 \tau_{90°}$, where $\tau_{90°}$ is the 90° scattering time.[58] Thus ions with energies above this minimum unconfined energy will be subject to rapid pitch angle scattering loses. If E_i, the ion energy, is below about 18.6 T_e (for deuterium), this pitch angle loss will occur in a time faster than the time necessary for the ion to slow down on the bulk plasma and a large fraction of its energy will be lost.

Figure 10 shows the confinement boundaries for the same conditions as those of Fig. 9, except that now the plasma current is 75 kA. The minimum unconfined energy is reduced to 6 keV at r = 3 cm. Furthermore at r = 3 cm perpendicular ions with energies greater than 37 keV are on unconfined orbits. Thus at 75kA lower energy ions would be subject to pitch angle scattering losses than at 150 kA. In addition, most perpendicular ions with energies above 37 keV will be on unconfined orbits; we would therefore expect a sharp cutoff in any ion tail produced by the rf at this energy. Figure 11 shows the variation of minimum unconfined energy with minor radius for plasma currents I_p = 100 kA, 150 kA, and 200 kA. We see that as the plasma current is raised an ion will not be subject to pitch angle scattering losses over a larger minor radius. This effect is most pronounced for E_i > 10 keV. In Sections III and IV it will be

shown that ions with energies of tens of keV are produced by the rf and that in fact these confinement considerations are relevant.

It should be noted that the effective loss radius for an ion can in some cases be smaller than the limiter radius a. The edge neutral density in Alcator A when dn/dt = 0 has been estimated at $10^{11}cm^{-3}$. At this density a 10 keV hydrogen ion would be charge exchange lost in a time $\sim$ 100 μsec, which is much shorter than the $\tau_{90°} \sim$ 2 msec in a central plasma density of $2.5 \times 10^{14}cm^{-3}$. During gas puffing in Alcator A in the initial stage of the discharge the edge neutral density could rise to $10^{12}cm^{-3}$, which would push the point at which the neutral density was $10^{11}cm^{-3}$ 2 cm into the plasma. Any ion or an orbit passing through this region would be rapidly charge exchange lost; thus the effective loss radius could shrink from 10 cm to 8 cm during gas puffing. Furthermore, the low electron temperature at the plasma edge will cause some slowing of the ions that pass through that region. The slowing down time of an energetic ion due to electrons is[58]

$$\tau_{se} \simeq \frac{1.26 \times 10^{9} T_e^{3/2}}{n_e \ln \Omega} \qquad (28)$$

where T_e is in eV and $\Omega = n_e \lambda_D^3$. When an ion has an energy greater than the minimum energy for an orbit to cross the plasma edge, it can scatter into orbits that cross the plasma edge at $r < a$. If at this radius τ_{se} is less than $\tau_{90°}$ at the center, a substantial fraction of the ion energy will be dumped at the plasma edge.

If $\tau_{se} \lesssim 0.1\ \tau_{90°}$, then an ion may lose all of its energy in the plasma edge on electrons before scattering into a better confined orbit. In this case the region of velocity space that contains these edge crossing orbits will be depleted and act as a loss region. For a 20 keV deuterium ion in a Alcator A plasma with T_{eo} = 1 keV and I_p = 150 keV, $\tau_{se} = 0.1\ \tau_{90°}$ occurs when T_e = 230 eV at r ∿ 7 cm. Thus high energy ions can have an effective loss radius less than the limiter radius due to $T_e(r)$.

This effect on confinement is shown in Fig. 12 where I_p = 150 kA, B_T = 62 kG and we consider deuterium ions. We plot the minimum confined energy as in Fig. 11, but for several different effective loss radii. Figure 12 shows that as the effective loss radius changes from 10 to 7 cm, a 15 keV deuterium ion will be subject to pitch angle scattering losses outside r = 1 cm, whereas before it could only be lost at r > 3 cm. This shrinkage of the effective loss radius thus causes a shrinkage of the plasma volume that can contain energetic ions and therefore be heated by rf. During gas puffing this effect could reduce rf heating efficiences.

Another energetic ion loss mechanism on Alcator A is due to the ripple in the toroidal field at each port due to the gap in the Bitter magnet. This ripple is 2.5% on axis and 7.5% at the limiter radius. The effective net ripple will be reduced from this value by the rotational transform[59]

$$\delta_{eff} = \delta\left[\sqrt{1 - \alpha^2\sin^2\vartheta}\right. \qquad (29)$$

$$\left. - \alpha\left[\frac{\pi}{2} - \sin^{-1}(\alpha\,|\sin\vartheta|)\right]|\sin\vartheta|\right]$$

where δ is the ripple in the absence of plasma current, δ_{eff} is the effective ripple, θ is the poloidal angle, and $\alpha = 2r/(RNq(r)\delta)$, where $B_{To}(r,\phi) \simeq B_{To}\ (1 - r/R \cos\theta - \delta/2 \cos N\phi)$. In Alcator A the ripple is too large to be seriously reduced according to Eq.(29) and $\delta_{eff} \sim \delta$. Energetic ion losses due to ripple has been previously considered.[59-64] In the case of Alcator A where $\delta_{eff} \sim \delta$ an ion will be trapped in the ripple well if $|v_{||}/v| < \delta^{1/2}$. Such a trapped ion will drift upward with a velocity $v_D = v^2/(2\ \omega_{ci} R)$. It will drift out of the central portion of the plasma if the drift distance $d > a/2$, where $d \simeq 2\delta v_D \tau_{90°}$. This condition defines an energy above which ripple trapped ions will be depleted

$$E_d = \left[\frac{8\pi}{2^{7/2}} \frac{ne^4 \ln\Omega\ m_i^{1/2}\ a\ R\ \omega_{ci}}{\delta}\right]^{2/5} \tag{30}$$

In Alcator A at $n_e = 2.4 \times 10^{14} cm^{-3}$, deuterium, and $B_T = 60$ kG, $E_d \simeq 5$ keV. The depletion of ripple trapped particles above this energy has been observed by charge exchange measurements on Alcator A.[65]

Above this energy E_d within the ripple there is a hole in velocity space. The nearly perpendicularly rf generated ions will be lost by rapidly pitch angle scattering into this hole in a time $\tau_{loss} \sim 4\ (v_{||}/v)^2\ \tau_{90°}$. Since $v_{||}/v \sim (T_i/E_i)^{1/2}$, τ_{loss} can be much smaller than the slowing down time and can cause significant power losses. It should be noted

that on Alcator A the ripple in the toroidal field is not described by a simple cos ϕ relation, but is limited to a small fraction ($\sim$ 0.2) of the machine toroidally near each of the 4 ports; most of Alcator A (toroidally) is ripple free. However, a heuristic Monte Carlo code has shown that this geometrical limitation of the ripple extend will cause no reduction in the ripple losses.[66]

In summary, these forementioned ion losses could cause a substantial effect and reduction in the rf heating efficiences in Alcator A. As will be stated below, the available rf power is far less than the ohmic heating power, and these orbit effects could then significantly affect the experimental observations.

III. Experimental Results

A. Experimental Setup

The experimental arrangement is schematically illustrated in Fig. 13. The rf is injected into Alcator A through one of four horizontal access ports located 180° toroidally away from the main limiter. 15 cm on either side of the waveguide array are "virtual" limiters which protrude 1 cm radially inward from the 12.7 cm radius vacuum vessel wall; the main limiter defines a plasma radius of 10 cm. Diagnostics such as charge exchange, electron cyclotron emission, Thomson scattering, and rf probes are located at the two access ports 90° away toroidally from the waveguides. Hydrogen or deuterium gas puffing is done at the microwave array port.

The microwave array consists of two adjacent waveguides connected along their long side by a 0.09 cm septum. Each waveguide has inside dimensions of 8.13 cm by 1.275 cm for a combined total area of 20 $cm.^2$ Most of the work described below was accomplished with an array having ceramic vacuum windows outside the toroidal field magnet; the $\omega = \omega_{ce}$ layer was then in vacuum. In the final stages of the experiment breakdown tests were performed with an array having ceramic vacuum windows near the waveguide mouths. The $\omega = \omega_{ce}$ layer was then pressurized with dry nitrogen. The power and phase was individually controlled and monitored in each waveguide; in addition the position of the array was adjustable from the vacuum vessel wall to

the limiter radius. Work was carried out at power levels varying between 5 W and 90 kW at a frequency of 2.45 GHz.

Experiments were carried out in both hydrogen and deuterium Alcator A discharges having $B_T < 80$ kG and $I_p < 200$ kA. Average operating parameters were $I_p \approx 150$ kA, and $B_T \approx 60$ kG with a total ohmic input power of 300 kW. Due to the high plasma density which causes rapid electron-ion equilibration ($\tau_{ei} \sim$ 5 msec) T_e and T_i were usually close together ($T_e \approx 1$ keV, $T_i \approx 800$ eV. Since the net rf power injected into the torus (substracting reflected waveguide power) was less than 75 kW and much less than the ohmic power, only small changes in the bulk plasma temperatures are to be expected. The global energy confinement time is $\tau_E \approx 6$ msec at a line averaged density $\bar{n}_e = 1.5 \times 10^{14} cm^{-3}$. Temporal changes in T_e or T_i due to the rf are expected to occur on time scales comparable to τ_E. $\bar{n}_e$ was varied between $0.5 \times 10^{14} cm^{-3}$ to $4.0 \times 10^{14} cm^{-3}$ during this work by pulsed gas injection. The radial density profile at $\bar{n}_e \lesssim 2.0 \times 10^{14} cm^{-3}$ is parabolic for $r < 10$ cm [67] with a peak density $n_{eo} = n_e(r = 0) \tilde{=} 1.5\ \bar{n}_e$; at $r = 10$ cm (the limiter edge) the edge density is $0.1\ n_{eo}$.[68] The density continues to decrease to about $0.03\ n_{eo}$ at $r = 11.5$ cm (the virtual limiter edge) at which point it probably drops sharply (successful density measurements in the shadow of the virtual limiters have not been carried out). The electron temperature profile is gaussian, namely $T_e(r) \approx T_{eo} \exp(- r^2/r_T^2)$, where r_T is defined in Eq. (32); T_i has a similar or perhaps broader radial profile. Finally it should be noted that in Alcator A strong density fluctuations having $\Delta n/N \sim 1$ have been observed at the limiter edge[45]

which could scatter the lower hybrid waves.[49]

B. Waveguide-Plasma Coupling and RF Breakdown

Figure 14 shows the results of coupling measurements made at a power level of 5 W with the center of the waveguide mouths at r = 10 cm. The total global reflectivity R_T of the array is graphed vs. ϕ, the relative phase difference of the incident waves in the two waveguides. This low power work was carried out in deuterium at B_T = 60 kG. A minimum in reflectivity is observed at ϕ = 195° at both $\bar{n}_e = 3 \times 10^{14} cm^{-3}$ and $\bar{n}_e = 0.5 \times 10^{14} cm^{-3}$; as the density increases the reflectivity increases. The solid lines are the theoretical predictions of Brambilla theory, adjusting ∇n to best fit the data. We note here that there was a 15° error in the ϕ measurement; the minimum in R_T at ϕ = 195° is identified as the ϕ = 180° symmetry point and the theory is plotted taking this into account. We note that the density gradients $\sim 10^{15} cm^{-4}$ indicated in Fig. 14 necessary to match R_T to theory are larger than the gradients present in the absence of the waveguide which are $\sim 10^{13} cm^{-4}$. One possible explanation is that sharp gradients of ion Larmor radius scale length could be caused by the presence of the waveguides; however, this hypothesis could not be confirmed as a measurement of ∇n_e at the waveguide mouth was not possible.

Figure 15 shows R_T vs. waveguide mouth position for ϕ = 180° at $\bar{n}_e = 1 \times 10^{14} cm^{-3}$ and $\bar{n}_e = 0.5 \times 10^{14} cm^{-3}$. A sharp minimum in R_T at r = 12.1 cm is observed at which point the waveguide mouth is near the vacuum vessel wall. At r < 12.1 cm R_T increases with increasing density, which suggests that density gradient in front of the waveguide

mouth is greater than $10^{13}cm^{-4}$ as shown in Fig. 3a. At $r > 12.1$ cm part or all of the waveguide mouth is recessed behind the vacuum vessel wall and Brambilla theory doesn't apply (the waveguide mouth itself has a flat face, whereas the vacuum vessel wall is of course circular). The minimum in R_T at $r = 12.1$ cm allows $R_T \leq 20\%$ and good waveguide-plasma coupling results. Since this minimum in R_T at $r = 12.1$ cm persisted at high power, most of the rf heating work was done there.

Figure 16 shows the variation in R_T as the incident power P_{rf} was varied from 5 kW to over 80 kW; within the experimental error R_T is unchanged at 13%. In this case $r = 12.1$ cm, $\phi = 180°$, $\bar{n}_e = 1.7 \times 10^{14}cm^{-3}$, $B_T = 60$ kG and a deuterium discharge was used. No breakdown was observed up to $P_{rf} = 90$ kW, which would correspond to $P_{rf}/A = 4.5$ kW/cm^2 at the waveguide mouth. Furthermore, the unchanged reflectivity as P_{rf} increases by a factor of 10 is not suggestive of any nonlinear or ponderomotive effect on R_T. Figure 17 shows R_T vs. ϕ at $r = 12.1$ cm. There is a slight phase dependence of R_T, resulting in most efficient coupling at $\phi = 180°$. This coupling does not vary as P_{rf} is changed from 32 kW to 85 kW and agrees with measurements at $P_{rf} = 5$ W within experimental error. Fig. 18 shows R_T vs. ϕ at $r = 12.1$ cm, 11.1 cm, and 10.6 cm, for $\bar{n}_e = 1 \times 10^{14}cm^{-3}$, $B_T = 62$ kG, deuterium, and $P_{rf} = 75$ kW. A strong dependence of R_T on ϕ is obtained at steeper density gradients as the waveguide is pushed further into the plasma. In summary, both the high and low power coupling measurements exhibit by themselves no clear contradiction to linear-waveguide plasma coupling theory. However, it should be cautioned that $\bar{n}$ in the presence of the waveguides was not measured; specifically when the waveguides

were positioned at r = 10 cm the plasma at the waveguide mouth may have been overdense ($n_e > 7 \times 10^{10} cm^{-3}$ for $f_o = 2.45$ GHz), and Brambilla theory may not directly apply to this case.

The previous results were all accomplished with a waveguide array having its vacuum windows outside the toroidal field magnets. The $\omega = \omega_{ce}$ layer, which occurs at B = 876 G, was situated within the evacuated section of waveguide. Nevertheless, no clear rf breakdown was observed at $P_{rf} < 90$ kW or $P_{rf}/A < 4.5$ kW/cm^2 with r = 12.1 cm. However, above $P_{rf} = 80$ kW the reflected power in the two waveguides became unbalanced when $\phi = 180°$ and r = 12.1 cm. This is illustrated in Fig. 19, where the balance B is plotted vs. time for three separate rf pulses (B = reflected power in left waveguide/ total reflected power). At $P_{rf} < 50$ kW, B ≈ 0.5 as expected by symmetry. At higher P_{rf} significant deviations from B = 0.5 are obtained. Finally at $P_{rf} = 90$ kW B(t) wildly oscillates, indicating that the reflected power is alternating between waveguides. However the total reflected power does not change and plasma heating is still obtained. Clearer evidence of breakdown is exhibited in Fig. 20, where $\bar{n}_e \sim 0.5 \times 10^{14} cm^{-3}$ and we compare the reflected powers at r = 12.1 cm and r = 11.1 cm. As the waveguide is moved into the plasma, the reflectivity increases, thereby increasing the peak electric field in the waveguides. As shown, there is a sharp increase in reflected power at r = 11.1 cm that is not associated with any rapid change in plasma parameters. We see that, while at r = 12.1 cm no breakdown and good waveguide-plasma coupling are obtained up to $P_{rf}/A = 4.5$ kW/cm^2, this appears to be an upper limit on the power handling capability of this waveguide.

In order to see if this breakdown limit could be pushed to higher power densities, a waveguide array was tested having vacuum windows near the waveguide mouths so that the $\omega = \omega_{ce}$ layer was pressurized.* Otherwise this array was identical to the previous one. Fig. 21 shows raw data obtained from this array at a peak P_{rf} = 90 kW, $\bar{n}_e = 1.5 \times 10^{14} cm^{-3}$, B_T = 62 kG, deuterium, ϕ = 180° and r = 12.1 cm. The lowest four traces are crystal signals proportional to the forward and reflected powers in each waveguide. No sudden change in any crystal signal is observed. A large increase in the neutron rate occurs concurrent with the rf, which is evidence of ion heating and will be further discussed below. Thus there is no sign of breakdown at $P_{rf}/A = 4.5\ kW/cm^2$.

Fig. 22a plots R_T vs. P_{rf} for 3 values of $\bar{n}_e$ and with the array at r = 12.1 cm. Within experimental error R_T is independent of P_{rf}, further indicating the lack of breakdown. Fig. 22b shows R_T vs. $\bar{n}_e$ for P_{rf} = 90 kW. R_T decreases as $\bar{n}_e$ increases, which indicates that the waveguide mouth may be slightly further away from the plasma than the location of the optimum R_T in Fig. 15. This hypothesis was tested by moving the array 1.5 mm further into the plasma; at $\bar{n}_e \sim 1.5 \times 10^{14} cm^{-3}$ R_T decreased, as shown in Fig. 22. This result indicates the sharpness of the minimum in R_T vs. r.

Finally, Fig. 23 shows the result of roughly doubling P_{rf}/A by exciting only one waveguide. Here 80 kW of rf power is launched into the left waveguide, which now has

P_{rf}/A = 8 kW/cm^2. The right waveguide is not directly excited by the rf generator and is terminated in a dummy load. No sign of breakdown is exhibited in either the forward or reflected power signals (the reflected power in the left waveguide is less than 3% of the incident power).

C. Plasma Heating Results

Studies of plasma heating were carried out using the two waveguide array having vacuum windows outside the toroidal field magnets. The center of the waveguide mouths was positioned at r = 12.1 cm for the lowest R_T and P_{rf} was between 80 kW and 90 kW. Generally, deuterium plasmas were used with B_T = 62 kG, I_p = 150 kA, $T_e \simeq 1$ keV and T_i = 800 eV at $\bar{n}_e \sim 1.5 \times 10^{14} cm^{-3}$. Figure 24a shows typical raw data during an rf shot having P_{rf} = 80 kW. There is no increase in loop voltage V_L, resistive voltage V_R (V_R is formed from V_L by taking into account the mutual inductance between the center of the plasma and the vacuum vessel) or density. No effect is observed on the nitrogen, oxygen, carbon, or molybdenum impurity radiation due to the rf pulse. However, the lowest trace shows a factor of 15 increase in the neutron rate concurrent with the rf pulse. Up to factors of 50 increase in the neutron rate have been observed due to the rf, which correspond to peak neutron rates of $2 \times 10^{11} sec^{-1}$.

This neutron rate enhancement could be caused by photoneutrons from the molybdeum limiter, e - D disintegration neutrons, or D - D fusion neutrons. Several neutron detectors situated at different toroidal locations see equal neutron rates; photoneutrons originating from the limiter would cause a factor of 30 difference in response between detectors at the limiter and at the waveguide array.[69] The neutrons are therefore uniformly produced toroidally and cannot be photoneutrons from the limiter. e - D neutrons would be caused by energetic

electrons having energies in excess of 2.2 MeV. Electron cyclotron emission at $\omega = 2\omega_{ce}$ is sensitive to nonthermal electrons, yet sees no increase in $\omega = 2\omega_{ce}$ radiation during the neutron rate increase. Furthermore, when the density is reduced below $1 \times 10^{14} cm^{-3}$ and strong nonthermal electron cyclotron emission is observed during the rf pulse, no neutron rate increase occurs. Finally, concurrent with the neutron rate increase there is a sharp increase in high energy neutrals emitted by the plasma having E > 5 keV. These observations virtually rule out the possibility of the rf generated neutrons being caused by e - D disintegrations and indicate that this neutron rate increase is due to D - D fusion neutrons.

Figure 24b shows the increase in the neutron rate vs. density for several shots at $B_T = 62$ kG, $I_p = 150$ kA, and in deuterium. Enhancements in the neutron rate are confined to a narrow range of $\bar{n}_e$ centered about $1.7 \times 10^{14} cm^{-3}$, suggesting a resonant effect. In Fig. 25 we show the neutron rate enhancement vs. $\bar{n}_e$ in deuterium for $B_T = 80$ kG, and $I_p = 200$ kA. A similar resonance is obtained, although the peak in the neutron rate may be slightly downshifted in $\bar{n}_e$ by the order of $0.1 \times 10^{14} cm^{-3}$. A slight upshift in the density band is found when B_T is lowered to 52 kG. No neutron enhancement occurs at all when $B_T \leq 48$ kG for $\bar{n}_e \leq 2.5 \times 10^{14} cm^{-3}$. At this low field $\omega > (\omega_{ce}\omega_{ci})^{1/2}$ for $r < 5$ cm and the central plasma is therefore not accessible to the lower hybrid wave. These results will be summarized below. Fig. 26 shows the neutron rate enhancement vs. $\bar{n}_e$ for $B_T = 62$ kG, $I_p = 150$ kA, deuterium, and the array mouth positioned at $r = 10.6$ cm.

Now the face of the array is no longer between the virtual limiters, but further into the plasma where n and ∇n are larger. Nevertheless, the neutron density band is essentially the same as that of Fig. 24, showing that this result is not an artifact of the density gradient at the waveguide-plasma interface.

The absence of rf generated neutrons when $B_T < 48$ kG suggests that the rf enhanced neutron production occurs near the plasma center. Figure 27 shows an expanded graph of a typical neutron rate and the central chord soft x-ray emission rate. Sawteeth are observable on the enhanced neutron rate which are well correlated to the sawteeth on the soft x-rays originating in the plasma center. This indicates that the neutrons are produced by energetic ions within the $q = 1$ surface at $r < 3$ cm. The neutron rate falls off with a time constant of 1.5 msec after the rf is shut off. This time is much longer than the 10 μsec loss times expected for ions generated at the plasma edge. As will be discussed in section IV this decay time is consistent with energetic ions at the plasma center slowing down on electrons. Figure 28 plots the relative neutron count rate during rf vs. r for a collimated neutron detector.[70] During these measurements the total neutron production of many shots were added together at each chord position; however, the rf neutron production dwarfed the thermal emission by over an order of magnitude. The shaded area is the level of neutron leakage into the detector due to imperfect collimation. The rate is sharply peaked at $r = 0$. An Abel inversion of this data reveals a neutron production rate peaked at $r = 0$

with a half maximum occurring at r = 1.7 cm. The results show that the rf enhanced neutron production is localized to the plasma center.

Fig. 29 shows the variation in rf enhanced neutron rate enhancement vs. ϕ for P_{rf} = 80 kW, B_T = 62 kG, $\bar{n}_e = 1.6 \times 10^{14} cm^{-3}$ and I_p = 150 kA. Within $\pm$ 10% there is no variation in the neutron rate when ϕ is varied from 0° to 180°. This result strongly contradicts the theory of Fig. 3b, which predicts that the $P(n_z)$ power spectrum will change from being characterized by $n_z \sim 3$ to having $n_z \gtrsim 1$ when ϕ varies from 180° to 0°. At ϕ = 0° over 80% of the power would have $n_z < 1.5$ and not be accessible past the plasma edge at r = 9 cm where $n_e = 7 \times 10^{13} cm^{-3}$ when $\bar{n}_e = 1.6 \times 10^{14} cm^{-3}$. Thus little effect on the ions at r = 0 would be expected when ϕ = 0°. This result implies that the lower hybrid waves are having their $\vec{k}$ changed at the plasma edge at r > 9 cm in order to gain accessibility.

Fig. 30 plots the rf neutron rate enhancement vs. P_{rf} for $\bar{n}_e \simeq 1.7 \times 10^{14} cm^{-3}$, B_T = 60 kG, I_p = 150 kA, and ϕ = 180°. The rf produced enhancement becomes detectable at P_{rf} = 10 kW, above which it varies roughly as P_{rf}^2. From this result it seems that by increasing the rf power the ratio of (neutron rate)/(rf power input) can be substantially increased.

During the rf neutron enhancement an increase is observed in energetic neutral emission by the plasma. This emission is monitored by a charge exchange analyzer oriented

perpendicularly to the toroidal magnetic field. Due to the 2.5% ripple on axis in the toroidal field at the ports, the charge exchange analyzer monitors ions that are ripple trapped in this magnetic well. Figure 31 shows typical fast neutral spectra observed through the central chord of the plasma before, during and after the rf pulse. Without rf the spectra are characterized by T_i = 750 eV; in agreement with Eq. (30) there is a cutoff above E $\sim$ 5 keV due to ripple trapping. Above this energy the ripple trapped ions will drift out of the plasma in t $\sim$ 100 μsec and are subject to a depletion. During the rf pulse this depleted tail is repopulated by the rf as shown in Fig. 31. Due to the rapid ∇B losses this perpendicular ion distribution function is not necessarily the same as the toroidally circulating ion distribution function. However, it does indicate that during neutron enhancement the rf creates energetic ions. When the rf is turned off, the neutral flux at energies greater than 5 keV decays away in a time less than 500 μsec. This is expected, since these ions are ripple trapped and ∇B drift out of the plasma. The neutron enhancement is produced by circulating ions and therefore decays in a much longer time. Furthermore, if the charge exchange spectrum of Fig. 31 is used to calculate a neutron rate enhancement, it is over a factor of 10 smaller than that observed. This point will be discussed in Section IV. Finally it should be noted that within the accuracy of the charge exchange apparatus (ΔT_i = 100 eV) no clear change in bulk ion temperature is observed; furthermore any change in T_e due to the rf during this neutron enhancement is less that 50 eV.

Figure 32 shows the results of an up-down scan of the charge exchange analyzer during the rf pulse at E = 6.6 keV and E = 9.8 keV. No flux is observed through a chord crossing more than 5 cm below the plasma center. As the chord is moved upwards (in the direction of the ∇B drift) the energetic flux sharply increases as the plasma center is approached. This is interpreted as evidence that the energetic ion production is localized near the plasma center. The increase in flux as the chord is moved above the plasma center is due to the energetic ions drifting into the higher neutral density plasma exterior. Figure 33 shows a density scan of the E = 8 keV charge exchange flux in hydrogen during the rf pulse. A density band is found which is similar to that of the neutron band in deuterium, except that the density band is downshifted to $\bar{n}_e \sim 0.9 \times 10^{14} cm^{-3}$. This downshift is in rough agreement with the mass dependence of the lower hybrid mode conversion layer of Eq. 6.

When the plasma density is lowered below the neutron production band, the high energy tail in the charge exchange spectrum no longer appears. However, electron heating is observed to take place. Figure 34 shows raw data from an rf shot at $\bar{n}_e \sim 0.9 \times 10^{14} cm^{-3}$ where P_{rf} = 80 kW, $\phi = 180°$, B_T = 60 kG, and deuterium is employed. During the rf pulse there is no change in impurity radiation or density, but V_R decreases slightly. Soft X-ray emission from the plasma center increases during the rf pulse and there is a 10% increase in the $\omega = 2\omega_{ce}$ electron cyclotron emission from the plasma

center. At this density and at T_e = 1.1 keV the $\omega = 2\omega_{ce}$ layer is optically thick and this emission should be proportional to T_e. Thomson scattering measurements averaged over consecutive identical shots with and without rf indicates an increase in T_e from 1130 eV $\pm$ 50 eV without rf to 1250 eV $\pm$ 30 eV with rf. This 10% increase in T_e due to rf represents at least a 35% heating efficiency in this mode and will be further discussed in Section IV. The increase in $\omega = 2\omega_{ce}$ emission is found to be roughly proportional to P_{rf} between 20 kW and 80 kW. In fig. 35 we plot $T_e(r)$ with and without rf from the $\omega = 2\omega_{ce}$ emission from two identical shots; $\bar{n}_e = 1.2 \times 10^{14} cm^{-3}$, P_{rf} = 80 kW, $\phi = 180°$, B_T = 60 kG, and deuterium is employed. The change in T_e is seen to be largest near the plasma center, as would be expected from electron Landau damping. Past r = 5 cm the $\omega = 2\omega_{ce}$ layer is no longer optically thick and the temperature plotted is higher than the true temperature. Finally, we note that when $\bar{n}_e$ is further reduced to $0.5 \times 10^{14} cm^{-3}$, strong nonthermal electron cyclotron emission enhancement during the rf pulse is observed which reflects the generation of suprathermal electrons. Decreases in V_R and V_L are clearly observable and the plasma column shifts outward. However, Thomson scattering measurements were not carried out in this regime to determine what fraction of this increased plasma energy is in the suprathermal electrons and what fraction is in the bulk distribution.

In Fig. 36 we summarize the previously cited results by indicating the density bands within which a neutron enhancement is observed during rf, and the density

bands within which energetic neutrals are observed during the application of rf power in hydrogen discharges. The curves indicate the appearance of the mode conversion layer at the plasma center for $n_{||} = 3$ and $n_{||} = 5$; in graphing the experimental results we let $n_{eo} = 1.5\ \bar{n}_e$ = central plasma density. We see that for $n_{||} = 3$, the typical value of $n_{||}$ expected from linear theory to characterize the lower hybrid wave spectrum launched by the waveguide array, the theoretical curve is in poor agreement with the experimental ion heating bands in deuterium. From Section II we would expect that ion heating would only occur at or slightly below the mode conversion density. However, for $n_{||} = 5$ the curves agree well. Furthermore, electron Landau damping would only be expected to occur when $\omega/k_{||}\ v_{Te} < 3$ or $n_{||} > 5$ for $T_e = 1$ keV. This is an additional indication that the $P(n_{||})$ wave power spectrum is upshifted from that expected from linear theory. Finally, the neutron enhancement being independent of the waveguide phasing indicates that this upshift must originate near the plasma edge in order to permit penetration of the lower hybrid waves to the plasma center. In summary these results are contrary to expectations based on the validity of linear theory and require a reformulation of the wave-plasma interaction at the plasma periphery.

In the previous analysis we interpret the experimental ion heating results as corresponding to the appearance of the mode conversion layer at the plasma center. This interpretation would predict an upper limit to the density at which ion heating could occur; as the density is raised above the central plasma ion heating value, the heating zone would move radially

outward into regions of poorer energy confinement. For example, increasing $\bar{n}_e$ from $1.7 \times 10^{14} cm^{-3}$ to $2.4 \times 10^{14} cm^{-3}$ would move the absorption zone out to r = 5 cm. More importantly, at r > 5 cm energetic ion confinement would be worse than at r = 0; from Fig. 11 an ion with E > 6 keV at r > 5 cm would be subject to rapid pitch angle scattering into unconfined banana orbits. Since the rf heats ions by first depositing energy into an energetic tail, this confinement effect would lead to well defined ion heating density bands.

It should be noted that the Alcator A lower hybrid heating experiment is the first in which the thermal corrections to the dispersion relation are large enough to exhibit any n_z dependence experimentally. From Eq. (6) we can define a thermal correction factor $C = 2n_z (M_i a_T/m_e)^{1/2}/(1 - \omega^2/\omega_{ce}\omega_{ci})$ which determines the fractional decrease of the density at which the mode conversion layer appears. For previous experiments[1-9] $C \sim 0.5$ for $n_z = 3$, but for Alcator A $C \approx 2.1$ at $B_T = 62$ kG, $n_z = 3$ and deuterium. In Alcator A an upshift in n_z from 3 to 5 would lower the heating density by 31%, whereas in previous experiments this reduction would be less than 18%. As seen in Fig. 36 this correction is less in hydrogen due to the mass reduction of $\omega^2/(\omega_{ce}\omega_{ci})$ and this anomalous upshift in n_z is not noticeable from the ion heating results.

D. RF Probe and Waveguide Reflected Power Frequency Spectra

As shown in Fig. 13, an rf probe was situated 90° away from the waveguide array toroidally on the torus midplane. The probe had a 1 mm diameter by 3 mm long wire tip bent in

the poloidal direction. The probe, which had a flat frequency response within 3 db up to 2.5 GHz, was situated at r = 11 cm in the shadow of the limiter but outside the shadow of the virtual limiters. Using Eq. (4) we can calculate the angle of propagation of the lower hybrid wave having $n_z^2 >> 1$ in the edge plasma where $\omega_{pe}^2 << \omega_{ce}^2$ and $\omega_{pe}^2 << \omega^2$ using Eq. (4):

$$\tan\theta = \frac{v_{g\perp}}{v_{g\parallel}} = \frac{\left.\frac{\partial\omega}{\partial k_\perp}\right|_{k_\parallel}}{\left.\frac{\partial\omega}{\partial k_\parallel}\right|_{k_\perp}} \approx \frac{\omega}{\omega_{pe}} \quad . \tag{31}$$

For $n_e = 3 \times 10^{13} cm^{-3}$ (the density at r = 10 cm during ion heating) $\tan\theta \approx 5 \times 10^{-2}$ and by the time it traverses 90° toroidally a lower hybrid ray starting at the virtual limiters at r = 11.5 cm will easily penetrate further into the plasma than the position of the probe. Thus the probe will not see rays directly emitted by the waveguide array. It will monitor either surface waves with $n_\parallel < n_{za}$, surface waves caused by scattering $n_\parallel > n_{za}$ waves in the turbulent edge plasma, or waves that fill the plasma column after several passes. The probe could not be inserted further into the torus since it would be destroyed by the plasma.

Figure 37a shows a typical high frequency rf probe spectrum taken with P_{rf} = 30 kW, B_T = 62 kG, deuterium, and $\bar{n}_e = 2.1 \times 10^{14} cm^{-3}$. A well defined lower sideband is present that has well defined peaks which are separated by $\Delta\omega = \omega_{ci}$ for deuterium. At the probe the amplitude of the lower frequency sideband is usually at least 10 db down from the pump amplitude.

Figure 37b shows a typical low frequency rf probe spectrum taken with P_{rf} = 90 kW, I_p = 165 kA, $\bar{n}_e = 1.6 \times 10^{14} cm^{-3}$, B_T= 62 kG and deuterium. Well defined peaks at multiples of the deuterium cyclotron frequency occur on this spectrum. The appearance of both a high and low frequency spectrum during the rf pulse indicates the presence of parametric processes in the plasma. These decay waves have been previously observed in tokamaks.[2,7,9]

Figure 38 shows the variation in the shape of the high frequency rf probe spectrum as density is changed; here B_T = 82 kG, I_p = 200 kA, P_{rf} = 90 kW and a deuterium discharge is employed. At low density (where presumably mode conversion does not occur) no lower sideband is observed that is separated from the pump frequency by more than $\Delta\omega = 2\omega_{ci}$. As the density rises, the sideband amplitude increases for waves having $\Delta\omega > 2\omega_{ci}$; at $\bar{n}_e = 1.9 \times 10^{14} cm^{-3}$ a peak at $\Delta\omega = 9\omega_{ci}$ is clearly visible. At this point the mode conversion layer is presumably in the plasma. This result is qualitatively consistent with the discussion in Section II and previous numerical results.[37] The low frequency spectrum of Fig. 37b does not significantly change its form as the density is varied, which suggests it is generated near the plasma edge. The dependence of the amplitude of the lower sideband frequency spectrum on P_{rf} is found to be strongly nonlinear. At $\bar{n}_e = 1.7 \times 10^{14} cm^{-3}$, B_T = 62 kG, I_p = 150 kA and in deuterium, this lower sideband is not observed below a threshold power of 10 kW; above this threshold

its frequency integrated amplitude increases faster than P_{rf}. However, at P_{rf} = 50 kW it is still an order of magnitude less than the pump signal. Thus, the lower sideband parametrically generated lower hybrid waves do not appear to have a significant amplitude compared to the pump wave, at least as observed by the rf probe.

Figure 39 shows the rf probe spectra under finer frequency resolution with a 300 KHz spectrum analyzer bandwidth. Figure 39a shows the high frequency spectrum centered about the pump frequency; here B_T = 62 kG, $\bar{n}_e = 2.8 \times 10^{14} cm^{-3}$, I_p = 150 kA, and P_{rf} = 80 kW in deuterium. There is negligible power in the narrow peak at 2.45 GHz, the signal being broadened and downshifted in frequency (usually the sharp peak doesn't occur at all). Figure 39b shows the low frequency rf probe response with and without rf for $\bar{n}_e = 1.6 \times 10^{14} cm^{-3}$, I_p = 150 kA, B_T = 62 kG, and P_{rf} = 80 kW. We see that during the rf pulse there is a strong enhancement in the amplitude of the low frequency fluctuations. In the absence of the rf the low frequency fluctuations have a FWHM = 150 KHz.[45] The frequency downshift of the 2.45 GHz signal and the enhancement of the low frequency signal suggest these spectra result from a parametric decay; alternatively the broadening of pump wave could be caused by scattering

from drift waves. However, at this density where the high frequency signal FWHM $\sim$ 5 MHz >> 150 KHz, a huge number of scattering would be required to produce the observed frequency broadening. Furthermore, it is unlikely that a large number of passive scatterings could result in a frequency downshifted spectrum.

Figure 40 shows the high frequency spectrum of the rf probe at a lower $\bar{n}_e = 1 \times 10^{14} cm^{-3}$, deuterium, $B_T = 62$ kG, and $P_{rf} = 80$ kW, for both a 30 KHz and 300 KHz bandwidth. At lower density the FWHM of the probe signal is sharply reduced and (as will be later plotted) its amplitude increases. The asymmetrical frequency downshift of the probe signal is correspondingly reduced and is essentially only apparent in the 30 KHz bandwidth frequency spectrum. The behavior of the frequency integrated 2.45 GHz signal amplitude and its FWHM as a function of $\bar{n}_e$ are plotted in Fig. 41 for $P_{rf} =$ 80 kW, $\phi = 180°$, $B_T = 62$ kG, $I_p = 150$ kA, and a deuterium discharge. In Fig. 41a the probe signal amplitude at 2.45 GHz is plotted and exhibits a sharp decrease beginning at $\bar{n}_e \sim 1.5 \times 10^{14} cm^{-3}$ where the ion heating begins. Figure 41b shows the FWHM of the probe spectra vs. $\bar{n}_e$ which also shows a sharp increase from $\sim$ 400 KHz to 5 MHz at $\bar{n}_e$ rises from $1.5 \times 10^{14} cm^{-3}$ to $2.5 \times 10^{14} cm^{-3}$. At $\bar{n}_e > 3 \times 10^{14} cm^{-3}$ the mode conversion layer is certainly present in the plasma and should absorb the waves that are accessible to the plasma center, whereas for $\bar{n}_e < 1 \times 10^{14} cm^{-3}$ the mode conversion layer will not be present and weakly damped lower hybrid waves should fill the plasma column. Thus at high density the probe essentially monitors the surface waves.

Fig. 41a then implies an exceedingly low amplitude surface wave in the plasma due to the low amplitude signal at $\bar{n}_e > 3 \times 10^{14} cm^{-3}$. The sharp decrease in probe signal amplitude as $\bar{n}_e$ increases through the neutron enhancement band would be caused by the onset of absorption of the accessible lower hybrid waves at the mode conversion layer. This interpretation is illustrated by the arrows in Fig. 41a, which depict the values of $n_{||}$ that will mode convert and be absorbed at the plasma center at successive values of $\bar{n}_e$. Similarly, the sharp increase in the FWHM of the probe signal as $\bar{n}_e$ rises in Fig. 41b could be qualitatively explained by the appearance of the mode conversion layer. At high density only the surface waves are monitored, which are localized to the edge region where successive scatterings from density fluctuations or parametric instabilities could occur.

Figure 42 shows the dependence of the probe signal intensity at f = 2.45 GHz on ϕ; P_{rf} = 80 kW, B_T = 62 kG, I_p = 150 kA, $n_e = 1 \times 10^{14} cm^{-3}$ and a deuterium discharge is employed. At the three waveguide mouth positions at r = 12.1 cm, r = 11.1 cm and r = 10.6 cm virtually no ϕ dependence is obtained. Similar ϕ independent results are obtained at $\bar{n}_e = 1.7 \times 10^{14} cm^{-3}$.

Figure 43 shows the variation of probe signal power within 5 MHz of 2.45 GHz. vs. P_{rf} at $\bar{n}_e = 3.2 \times 10^{14} cm^{-3}$, I_p = 150 kA, B_T = 62 kG, deuterium, and with the array at r= 12.1 cm. The probe signal is roughly linear in P_{rf} over 3 orders of magnitude; no threshold is observed at P_{rf} = 100 W. Although threshold powers of the order of 1 kW are expected for a parametric decay into lower hybrid waves and ion acoustic waves, this level is still much higher

than 100W. The lack of a threshold at $P_{rf} \simeq 100$ W suggests that these results may be caused by a parametric decay into drift-waves; the threshold for this process might be low (as previously observed in a linear machine[44]), although in Alcator A these fluctuations are not understood. Alternatively, some of the frequency broadening could be caused by passive scattering from density fluctuations at the plasma edge, although this process alone would not account for the low frequency probe signal enhancement or the asymmetrical frequency downshift of the 2.45 GHz waves.

Figure 44 shows the frequency spectrum of the reflected power in a waveguide positioned at r = 12.1 cm for B_T = 62 kG, deuterium, I_p = 120 kA, $\bar{n}_e = 2.5 \times 10^{14} cm^{-3}$ and a 300 KHz spectrum analyzer bandwidth. The spectrum for both P_{rf} = 7 kW and P_{rf} = 200 W is shown. The reflected power is dominated by the "pump" signal at f = 2.45 GHz. The frequency integrated amplitude of the sidebands is 30 db down from the pump amplitude and the lower frequency sideband is larger in amplitude than the sideband whose frequency is above 2.45 GHz. Figure 45 shows a "discreet line" reflected power that would appear when the waveguide was inserted further into the plasma than the r = 12.1 cm point; here B_T = 62 kG, deuterium, $\bar{n}_e = 2.5 \times 10^{14} cm^{-3}$, I_p = 100 kA, P_{rf} = 80 kW and we use a 300 KHz bandwidth spectrum analyzer. In this case the waveguide array face was at r = 11.1 cm. While in Fig. 45 there are only frequency downshifted sidebands, in some cases discreet sidebands appear both above and below the pump frequency. These spectra do not change at different values of $\bar{n}_e$, which suggests they originate near the waveguide mouth at the plasma edge.

In Fig. 46 we show the pump and frequency integrated sideband reflected powers near 2.45 GHz vs. P_{rf} for the waveguide array face at r = 12.1 cm and for $\bar{n}_e = 2.5 \times 10^{14} cm^{-3}$, B_T = 62 kG, deuterium, and I_p = 120 kA. Figure 46a shows that the amplitude of the pump reflected power is proportional to the incident power until $P_{rf} < 200$ W, at which point this proportionality no longer holds. At this low power level the sideband power is of the same order of magnitude as the pump. Figure 46b shows that the sideband amplitude varies as $P_{rf}^{1/2}$ until $P_{rf} < 200$ W, at which point it rapidly decreases and is absent below P_{rf} = 50 W. Thus the sideband amplitude is not a linear function of P_{rf} and exhibits a threshold. This threshold for the appearance of this frequency broadened spectrum increases to 7 kW as the waveguide array is moved in to r = 11.1 cm. The behavior of the threshold of the discrete line reflected power sideband is opposite. When the face of the array is at r = 11.1 cm, the discrete line sideband onsets at $P_{rf} \sim 50$ kW. When the array is withdrawn from the plasma this threshold increases, until at r = 12.1 cm the sideband is not excited even at P_{rf} = 90 kW. These sidebands could be caused by density oscillations in the $\omega = \omega_{pe}$ layer in front of the waveguides that controls waveguide-plasma coupling. Alternatively these sidebands would be evidence of parametric backscatter localized near the waveguide mouth.

CO_2 laser scattering was also carried out during this work and observed the driven lower hybrid waves in the plasma interior. The wave amplitude in the plasma interior was found to be independent of relative waveguide phasing. Frequency downshifted and broadened wave spectra were measured, but

their FWHM did not follow the same $\bar{n}_e$ dependence as those of the rf probe. The amplitude of the lower hybrid wave inside the plasma was found to be proportional to P_{rf} for powers between 10 kW and 80 kW. The main results of this work were presented elsewhere.[13]

E. Energetic Ion Confinement Effects

As discussed in Section II the rf heats ions by first producing energetic ion tails; in order for lower hybrid heating to be efficient these tails must be confined in the plasma column. One loss mechanism is due to ripple trapping in the magnetic well of the port gap in the toroidal field magnet. Since ion heating only occurred at a fixed density, it was not possible to make a parametric study of this loss effect on rf heating. Another loss mechanism is due to imperfectly confined banana orbits; this loss process would affect ions with $E \gtrsim 15$ keV and is current dependent. Evidence that the rf produced ion tails having energies greater than 50 keV will be presented in Section IV. In fact dependences of the neutron enhancements on I_p were observed and these can be attributed to banana orbit losses.

At $I_p < 100$ kA no enhancement of the neutron rates during application of rf power were ever observed. Above I_p = 100 kA, the rf enhanced neutron rate grew as I_p grew, reaching a maximum enhancement factor of 50 above the thermal rate between 150 kA $< I_p <$ 200 kA at B_T = 62 kG. Furthermore, when the rf power was turned off the e-folding decay time of the neutron rate enhancement grew with increasing I_p. In Fig. 47 the e-folding decay time of the neutron rate after the rf pulse shutoff is graphed vs. I_p for

P_{rf} = 85 kW, $\bar{n}_e \sim 1.5 \times 10^{14} cm^{-3}$ and B_T = 62 kG and 80 kG. Over a factor of two increase in the decay time occurs when I_p is increased from 120 kA to 200 kA. Since within this range of I_p, $T_e(r = 0)$ does not vary by more than 10%[71] and since the neutron production originates at the plasma center, this increase can be interpreted as due to scattering of energetic ions into orbits that either hit the limiter, or pass through the edge plasma where T_e is low and the neutral density is high.

Finally, no neutron rate enhancement was observed when the rf power was injected during rapid density increases concurrent with gas puffing; this lack of neutron enhancement could be due to an increase in neutral density at the plasma periphery. This interpretation is strengthened by the observation that thermal neutron emission is usually absent or depressed during this period. These effects will be further elaborated on in Section IV.

IV. Discussion and Summary

A. Energetic Ion Tail Production and Confinement

As discussed in Section II, we expect that the lower hybrid wave heats the plasma by first producing energetic ion tails, which must be confined in order to obtain reasonable bulk plasma heating efficiencies. The charge exchange diagnostic measures fast neutrals having $\vec{v} \perp \vec{B}$, which originate from ions superbanana trapped in the toroidal field ripples. Due to this ripple, these trapped ions are subject to rapid ∇B drift losses for $E_i > 5$ keV; the fast neutral spectra obtained from these perpendicular ions are therefore not indicative of the untrapped ion distribution function which dominates the neutron production. The neutron rate is only sensitive to the integral of the fast ion distribution function and doesn't yield its detailed shape. Nevertheless, it is certain that the factor of 50 increase in the neutron rate due to the application of the rf power is mainly due to the energetic tail ions; if a tail was absent and these neutrons were of thermal origin, T_i would have had to increase from 800 eV to at least 1300 eV, which was not observed. Below we formulate a simple model in order to set a lower limit on the rf produced ion tail energy. In this model we shall calculate the neutron rate and decay time after rf turn off ignoring ion orbit losses. By ignoring these losses we will underestimate the ion tail energy and overestimate the neutron rate decay time. We can express the ion distribution function as

$$f(E) = (1 - \delta)\, f_b\,(E) + \delta\delta' \sum_{n=1}^{N} \delta(E - E_n)\, \alpha_n \qquad (32)$$

where $$\alpha_n = \frac{2\pi}{(\pi T_T)^{3/2}} E_n^{1/2}\, \Delta E\, e^{-E_n/T_T} = \text{constant}$$

$$\Delta E = E_{n+1} - E_n = \text{constant}$$

$$E_n = n\Delta E$$

$$\delta' = \left(\sum_{n=1}^{N} \alpha_n \right)^{-1} > 1$$

In Eq. (32) $f(E)$ has been expressed as a bi-maxwellian with a bulk distribution function at $T = T_o$ and a tail distribution function at $T = T_T$. Furthermore, the tail has been broken up into a sum of closely spaced delta functions normalized so that a fraction δ of the total ion population is in the tail. It is easy to show that for $T_T > 5$ keV the resulting neutron rate will be closely approximated by tail-bulk ion collisions in which we can ignore the bulk ion energies. We then obtain

$$n_e \nu_n = \text{Neutron Rate} \qquad (33)$$

$$\equiv 2n_e^2 (1 - \delta)\delta\delta' \sum_{n=1}^{N} \sigma_{DD}(E_n(t)) \left(\frac{2E_n(t)}{M_i} \right) \alpha_n$$

where we now allow $E_n(t)$ to vary as ions at an initial energy $E_n = E_{no}$ slow down on ions and electrons[56,57].

$$(E_n(t))^{3/2} = (E_{no}^{3/2} + E_c^{3/2}) \exp(-3t/\tau_{se}) - E_c^{3/2} \qquad (34)$$

where τ_{se} is given in Eq. (28) and $E_c \simeq 18.6$ Te for deuterium. $\sigma_{DD}(E)$ is the neutron production cross-section for a deuteron of energy E impinging on a stationary deuteron[72]. α_n is held constant, as ion orbit losses are ignored. Using Eq. (33) we can set δ by requiring a factor of 50 increase in the neutron rate during the rf pulse over the thermal rate for a given T_T and N (N fixes a cutoff energy at $E_{max} = N\Delta E$). The power in the tail per unit volume is

$$P_T/cm^3 = n_e \delta \delta' \sum_{n=1}^{N} \alpha_N \frac{2E_n(t)}{\tau_{se}} \left(1 + \left(\frac{E_c}{E_n(t)}\right)^{3/2}\right) \quad (35)$$

from which we can calculate the rf power necessary to sustain tail collisional power losses. In calculating the total power we will assume that the tail is uniform in a volume $2\pi R\pi\Delta r^2$, where $\Delta r = 3$ cm.

Figure 48a shows the result of this calculation for Alcator A lower hybrid heating parameters, $T_T = 20$ keV and $E_{max} = N\Delta E = 100$ keV. In order to maintain a factor of 50 increase in the neutron rate, $\delta = 0.0013$ and the total tail power is $P_T = 3.8$ kW. Furthermore, the neutron rate e-folding decay time is $\tau_N = 1.75$ msec, in rough agreement with the experimental results. Fig. 48b is the same as Fig. 48a, except that now $E_{max} = 25$ keV. Now $P_T = 90$ kW and $\tau_N = 0.64$ msec. This decay time is much shorter than the experimentally observed time. Similarly, Fig. 48c is the same as Fig. 48a, except that $T_T = 5$ keV. Now $\delta = 0.085$ and P = 249 kW. Again $\tau_N = 0.8$ msec and is much shorter than the experimental decay time.

Fig. 49 a and b summarize these results for a 50 X neutron enhancement. In Fig. 49a P_T and τ_N are graphed vs. T_T(keV) for E_{max} = 100 keV. We see that in order to obtain reasonable values of P_T and τ_N, T_T > 10 keV. Similarly, fig. 49b graphs P_T and τ_N vs. E_{max} for T_T = 15 keV. Again, in order to achieve reasonable values of P_T and τ_N, E_{max} > 50 keV in order to be at least qualitatively consistent with the experimental results. We note that these neutron rate decay times are characteristic of the slowing down of suprathermal ions with $E_i > E_c$ on bulk electrons. We can write

$$n_e \nu_n \propto \int_0^\infty dE\ E^{1/2}\ e^{-E/T_T} \left(\frac{2E_n(t)}{M_i}\right)^{1/2} E_n^{-1}(t) \quad \exp\left[-\frac{\gamma}{E_n^{1/2}(t)}\right] \tag{36}$$

where $\gamma \simeq 45.8$ for $E_n(t)$ in keV and is taken from the σ_{DD} cross-section for $E_n(t)$ above 13 keV. For $E_n(t) > E_c$, we can let $E_n(t) = E \exp(-2t/\tau_{se})$. Equation (36) can then be approximated by a saddle point technique, where the saddle point then occurs at $E = (\gamma T_T/2)^{2/3} \exp(\frac{2}{3}t/\tau_{se})$. For $t << \tau_{se} \simeq 12$ msec, we then find the asymptotic result that

$$\tau_N \simeq \tau_{se} \left[\frac{2^{1/3}\gamma^{2/3}}{T_T^{1/3}} - 1\right]^{-1} \tag{37}$$

which for T_T = 15 keV, T_e = 1 keV, and τ_{se} = 12 msec, τ_N = 2.2 msec. This calculation also indicates that the maximum neutron production will occur at $E_i \sim 50$ keV.

The inclusion of ion orbit losses will of course reduce τ_N. However, the neutron rate is dominated by ions with $E_i >> E_c$ where $\tau_{slow} \sim \tau_{se}$ and is independent of E_i. The orbit loss time will be $\sim (v_{||}/v)^2 \tau_{90°} \propto E_i^{3/2}$, as it is proportional to the time for an ion to scatter into the loss cone in velocity space. For not too small $v_{||}/v$, $\tau_{loss} > \tau_{se} >> \tau_N$ for $E_i > 50$ keV and the neutron decay time should be only mildly affected by orbit losses. However, the rf heating efficiency will be strongly affected. As the ions quasilinearly diffuse up to $E_i \sim 50$ keV due to the rf, they will be subject to strong pitch angle scattering losses into the ripple loss cones when $E_i > 5$ keV. Furthermore, a sizeable fraction of the tail power between 5 keV and 20 keV will more rapidly be lost by pitch angle scattering into this loss cone than will deposit its energy into the bulk, since in this region $\tau_{loss} \sim (v_{||}/v)^2 \tau_{90°} \sim (T_i/E_i)\tau_{90°}$ and is much less than $\tau_{slow} \sim \tau_{90°}$. Although a more detailed calculation of the combination of quasilinear diffusion and pitch angle scattering losses is necessary to accurately determine the rf bulk plasma heating efficiency, we see that the ripple losses will certainly limit rf power deposition into the bulk plasma.

This suprathermal nature of the ion tail allows us to qualitatively explain other aspects of the neutron enhancement. Figures 9 and 10 show that at r = 3 cm a reduction of I_p from 150 kA to 75 kA should lower the cut off of the perpendicular ion tail from 96 keV to 37 keV. From Fig. 49b we would then expect at least a factor of 10 reduction in the neutron rate,

which is qualitatively consistent with the absence of a neutron enhancement during rf when $I_p < 100$ kA. Furthermore, the τ_N vs. I_p curve of Fig. 47 is expected, as lowering E_{max} from 96 keV to 37 keV lowers τ_N from 1.6 msec to 0.9 msec in Fig. 49b. Finally, these suprathermal ions should be sensitive to a shrinkage in the effective loss radius, as discussed in Section II, and the absence of neutrons during gas puffing is consistent with this expectation. Thus the experimental observations are consistent with the rf production of a suprathermal ion tail which would be strongly affected by imperfectly confined orbits.

B. RF Heating Efficiences

As previously mentioned, due to the effect of the ripple loss on the perpendicular charge exchange diagnostic, a quantitative evaluation of the rf power deposited in the ion tail is not possible. Estimates of the rf power transferred into bulk plasma energy can be made. However, these estimates will be crude, as the maximum net available rf power of 75 kW is much less than $P_{OH} = 300$ kW and only small changes in the bulk plasma parameters are expected. Furthermore, during ion tail formation ion orbit losses are expected to further limit bulk heating efficiences.

A simple equation can be written for the power balance in the central plasma of Alcator A:

$$\frac{d\,T_e}{dt} = -\frac{T_e}{\tau_{Ee}} - \frac{(T_e - T_i)}{\tau_{ei}} + \frac{P_{OH}}{\frac{3}{2}n_e} + \frac{P_{rfe}}{\frac{3}{2}n_e} \qquad (38)$$

$$\frac{d\,T_i}{dt} = -\frac{T_i}{\tau_{ei}} + \frac{(T_e - T_i)}{\tau_{ei}} + \frac{P_{rfi}}{\frac{3}{2}n_e}$$

where $(T_e - T_i)/\tau_{ei}$ is the power transfer from electrons to ions, T_e/τ_{Ee} is the remaining electron power loss, T_i/τ_{Ei} is the remaining ion power loss, $P_{OH} = \eta J^2$ is the ohmic input power, and $P_{rfe,i}$ is the rf power input into the electrons or ions. τ_{ei} and η are the classical values of electron-ion equilibration and resistivity. We can average Eq. (38) over the central 5 cm radius plasma. By letting n_e = constant, $T_{e,i}(r) = T_{eo,io} \exp(-r^2/r_T^2)$, $J(r) = J_o \exp(-\frac{3}{2}r^2/r_T^2)$, and defining $V^{-1}\int dV\, T_i/\tau_{Ei} = \alpha\, T_{io}/\langle\tau_{Ei}\rangle$, where V is the volume, we obtain:

$$\frac{d\,T_{eo}}{dt} = -\frac{T_{eo}}{\langle\tau_{Ee}\rangle} - \frac{\gamma}{\alpha}\frac{(T_{eo} - T_{io})}{\beta\, T_{eo}^{3/2}} + \frac{\phi}{\alpha}\frac{n_o T_{eo}^{-3/2} J_o^2}{\frac{3}{2}n_e} + \frac{1}{\alpha}\frac{\langle P_{rfe}\rangle}{\frac{3}{2}n_e V} \qquad (39)$$

$$\frac{d\,T_{io}}{dt} = -\frac{T_{io}}{\langle\tau_{Ei}\rangle} + \frac{\gamma}{\alpha}\frac{(T_{eo} - T_{io})}{\beta\, T_{eo}^{3/2}} + \frac{1}{\alpha}\frac{\langle P_{rfi}\rangle}{\frac{3}{2}n_e V}$$

where J_o is the central current density corresponding to $q(o) = 0.9$, $\tau_{ei} = \beta\, T_{eo}^{3/2}$, $\eta = \eta_o\, T_{eo}^{-3/2}$ and γ, α, and ϕ are volume averaging constants:

$$\gamma = \frac{1}{\pi r^2}\int_0^r 2\pi r dr\, e^{1/2(r^2/a_T^2)} = 1.2$$

$$\alpha = \frac{1}{\pi r^2}\int_0^r 2\pi r dr\, e^{-r^2/a_T^2} = 0.72$$

$$\phi = \frac{1}{\pi r^2}\int_0^r 2\pi r dr\, e^{-3/2(r^2/a_T^2)} = 0.62$$

In Eq. (39) we have ignored changes in the temperature profiles as T_{eo}, T_{io} increase due to rf heating, which may change $\langle\tau_{Ei}\rangle$, $\langle\tau_{Ee}\rangle$ from the $P_{rf} = 0$ level. Furthermore, we have let T_e and T_i have the same radial profile; $T_i(r)$ is not well known but may be somewhat broader than $T_e(r)$. Nevertheless for the small changes expected in T_{eo} and T_{io} due to the rf power, Eq. (39) should give a reasonable estimate of the rf heating efficiency.

In steady state with $P_{rf} = 0$ we can set $d/dt = 0$ and find $\langle\tau_{Ee}\rangle$ and $\langle\tau_{Ei}\rangle$, which we will treat as constants. However, Eq. (39) allows the power transfer from electrons to ions and the ohmic power input to decrease at T_e increases. If we now let $T_{eo} = T_{eo} + \delta T_e$, $T_{io} = T_{io} + \delta T_i$, where δT_e, δT_i are small changes in T_e, T_i due to rf heating, in steady state we obtain after some algebra:

$$\delta T_i \left[-\frac{\gamma}{\alpha} \frac{T_{eo}}{\tau_{eio} T_{io}} \right] + \delta T_e \left[\frac{\gamma}{\alpha} \frac{1}{\tau_{eio}} \left(\frac{3}{2} \frac{T_{io}}{T_{eo}} - \frac{1}{2} \right) \right] = -\frac{1}{\alpha} \frac{\langle P_{rfi} \rangle}{\frac{3}{2} n_e V} \tag{40}$$

$$\delta T_i \left[\frac{\gamma}{\alpha} \frac{1}{\tau_{eio}} \right] + \delta T_e \left[\frac{5}{3} \frac{P_{ei}}{\alpha V} \frac{1}{n_e T_{eo}} - \frac{5}{3} \frac{P_{OH}}{\alpha V} \frac{1}{n_e T_{eo}} - \frac{\gamma}{\alpha} \frac{1}{\tau_{eio}} \right] = -\frac{1}{\alpha} \frac{\langle P_{rfe} \rangle}{\frac{3}{2} n_e V}$$

where $\tau_{eio} = 3\, T_{eo}^{3/2}$, $\langle P_{rfe,i} \rangle$ are the total rf power heating the bulk electrons or ions,

$$P_{OH} = \phi V n_o T_{eo}^{-3/2} J_o^2 = \text{total ohmic power into electron for } r < 5 \text{ cm}$$

$$P_{ei} = \frac{3}{2} n_e V \gamma \frac{T_{eo} - T_{io}}{\tau_{eio}} = \text{total power transfer for electrons to ions for } r < 5 \text{ cm.}$$

We can first examine the ion heating case when $n_e = 2.4 \times 10^{14} cm^{-3}$, $T_{eo} = 1$ keV, $T_{io} = 750$ eV, $\tau_{eio} = 6$ msec, $P_{OH} = 195$ kW, and $P_{ei} = 77$ kW. We find that $\delta T_e \simeq 0.51\ \delta T_i$ and for $\langle P_{rfe} \rangle = 10$ kW, $\delta T_i = 32$ eV. For a 50% heating efficiency (or 37.5 kW into the ions) $\delta T_i = 120$ eV, which is only marginally above the 100 eV resolution of the charge exchange measurement. During electron heating $n_e = 1 \times 10^{14} cm^{-3}$, $T_{eo} = 1.1$ keV, $T_{io} = 600$ eV, $\tau_{eio} = 11$ msec, $P_{OH} = 195$ kW and $P_{ei} \simeq 52$ kW. In this case $\delta T_i \cong 0.17\ \delta T_e$ and for $\langle P_{rfe} \rangle = 10$ kW, $\delta T_e = 25$ eV. Again for a 50% heating efficiency $\delta T_e = 94$ eV, which is detectable by the $2\omega_{ce}$ electron cyclotron emission. We see that reasonable rf heating efficiencies produce small bulk temperature changes. These estimates are in qualitative agreement with a more sophisticated 1 - D Alcator A transport code, which takes into account profile changes and inductive effects[73]. In this code the rf heating effects will vary somewhat from these results depending on the energy transport model employed.

From these estimates and the code we can conclude that the total electron heating efficiency is at least 35%. However, the ion heating efficiency is less than 40%. This low efficiency occurs in spite of the probe signals indicating the onset of strong wave absorption during neutron production. If the $\delta T_i(r)$ is strongly localized near $r = 0$, it would be only marginally observable

on the charge exchange diagnostics due to the radial gradients in the neutral density. The 1 - D transport code[73] indicates that when rf absorption is localized to r < 3 cm, $\delta T_i(r = 0)$ decays away after rf shutdown in a faster time than τ_E as the sharply peaked $\delta T_i(r)$ spreads to larger r. This $\delta T_i(r = 0)$ would therefore not persist long enough after rf shutdown to be observable on the neutron rate. Another strong possibility is that a large fraction of the rf power deposited into $E_i > 5$ keV ions may be lost through the ripple wells before heating the plasma.[66] In any case the exact rf heating efficiency in the neutron enhancement mode is not now known on Alcator A.

C. Anomalous Heating

As previously discussed, the neutron enhancement density bands are not consistent with the expected linear lower hybrid wave spectrum characterized by $n_{||} \sim 5$. The independence of the neutron rate on relative waveguide phasing also contradicts linear theory. Finally electron heating is not expected from the expected lower hybrid wave spectrum. These results require a reformulation of the lower hybrid wave-plasma interaction in the edge region.

One possible explanation for these results would be the parametric decay of the originally launched lower hybrid waves into higher $n_{||}$ lower hybrid waves and ion acoustic waves at the edge plasma. Since this decay would occur at the plasma periphery, where the waves are always accessible even for $n_{||} \gtrsim 1.5$, it would produce phase independent heating. Furthermore, it has been shown that such a decay occurring sufficiently close to the waveguide mouth would result in a wave power spectrum peaked at $n_{||} \sim c/\omega(\pi/b) \sim 5$ where b is the waveguide width[35]. This decay

would produce a frequency downshifted lower hybrid wave spectrum, which is also experimentally observed in addition to the enhanced low frequency wave spectrum. Sidebands are observed on the reflected power in the waveguide array, which have a nonlinear dependence on P_{rf} and suggest the presence of backscattering near the waveguide array. A problem with this explanation arises with Fig. 43, which shows a linear response at the rf probe 90° away toroidally from the waveguides at P_{rf} down to 100 W. From the discussion of section II thresholds in excess of 1 kW are expected for this decay when $T_e \sim T_i$ and the ion acoustic waves are strongly damped (T_i has not been directly measured in the edge Alcator A plasma, but is expected to be $\sim T_e \sim 10$ eV). This observation suggests that the low frequency decay waves being excited are weakly damped drift type waves, whose exact model in Alcator A has not been determined. It has previously been observed in a linear machine that such drift waves can be excited by lower hybrid waves at extremely low thresholds[44]. Furthermore, the fact that the enhanced low frequency waves are measured by an rf probe 90° away toroidally from where they are most likely to be generated (at the waveguides) further implies that they are weakly damped. Since these low frequency fluctuations are poorly understood, their parametric thresholds and decay properties are not known.

Nevertheless, the absence of a threshold or a clear nonlinear power dependence on the rf probe signals suggests that passive scattering processes off density fluctuations may also contribute to these results. As discussed in section II, an

isotropization of the launched lower hybrid wave at the plasma edge would result in an $n_{||}$ upshift due to magnetic shear as the wave propagated inward. This model would be in qualitative agreement with the observed phase-independent ion heating results and the electron heating results. Furthermore, it would produce power independent probe signal frequency spectra and linearly varying probe signal amplitudes. However, this passive scattering would not produce the frequency downshifted probe signals (or the frequency downshifted waves measured in the plasma interior by CO_2 laser scattering). Furthermore, the 5 MHz FWHM high $\bar{n}_e$ probe signal spectra are much wider than the 150 KHz FWHM drift wave frequency spread (although such a large lower hybrid wave frequency spread could in principle be caused by repeated scatterings of the surface waves). Thus, neither the parametric decay or the scattering from drift wave turbulence explain by themselves all of the details of the experimental results. It is possible that both processes are occurring and contributing to the anomalous observations.

It is interesting to note that Eq. (25) indicates that if drift wave scattering is the cause of the anomolous low ion heating densities, lowering I_p should further lower these densities. This is because as I_p is lowered, q(a) rises but q(o) is constant $\sim$ 0.9; thus the enhancement in $k_{||}$ (o) increases as I_p decreases. At $I_p \sim$ 125 kA a slight downshift in the neutron production band is observed from $\bar{n}_e \sim 1.7 \times 10^{14} cm^{-3}$ at $I_p \sim$ 170 kA to $\bar{n}_e = 1.4 \times 10^{14} cm^{-3}$. However, this small a shift in the density could be caused by small profile effects and is not conclusive in itself.

In section II it has been shown that scattering from drift waves can also enhance the edge plasma absorption of the lower hybrid waves. This edge absorption would be enhanced by $\ell_{90°}/\Delta x$, where Δx is the radial width of the scattering region[49]. This absorption would then increase with density and could limit rf heating efficiencies. However, it is unlikely that this effect could account for the strong wave absorption depicted in Fig. 41a at $\bar{n}_e \sim 1.5 \times 10^{14} cm^{-3}$, or any of the anomalous heating. We can calculate the imaginary part of k_z at the edge plasma due to the electron-ion collisional damping as $k_{zi} = k_z \nu_{eff}/(2\omega)$, where ν_{eff} is given in Eq. (7). Then the signal amplitude at the rf probe due to lower hybrid waves scattered back onto the surface by density fluctuations would roughly be

$$P_s \propto A(\Delta n/N) \exp(-\pi k_{zi} R) \qquad (41)$$

where $A(\Delta n/N)$ is a function that increases as $\Delta n/N$ increases and expresses the surface wave enhancement due to scattering of lower hybrid waves back onto the plasma periphery. The exponential factor is the maximum collisional attenuation of a lower hybrid ray in traversing between the waveguide array and the probe regardless of the strength of the drift wave scattering. For $n_z = 4$, $T_e = 10$ eV and $n_e(r = a) = n_{eo}/10$, $\pi k_i R \approx 0.25 (\bar{n}_e /10^{14})$. Fig. 41a shows no probe signal enhancement as $\bar{n}_e$ rises which would indicate a surface wave enhancement due to scattering. Furthermore, the decrease in probe signal amplitude as $\bar{n}_e$ increases past $1.5 \times 10^{14} cm^{-3}$ is

far more rapid that the 1.1 db/$(\bar{n}_e/10^{14}cm^{-3})$ decrease expected from collisions. Thus this rapid decrease in probe signal is not caused by collisional surface absorption. The appearance of the mode conversion layer at the plasma center as $\bar{n}_e$ increases past $1.5 \times 10^{14}cm^{-3}$ can cause rapid enough absorption to account for this signal decrease.

In conclusion, the Alcator A experiment has demonstrated lower hybrid wave penetration into the plasma interior and electron and ion heating, although the ion heating efficiency is not known. Suprathermal ion tails have been produced and ion orbit confinement effects observed. Furthermore these results point out the importance of acquiring a better understanding of the wave-plasma interaction at the plasma periphery.

Acknowledgments

The authors wish to express their appreciation to R.E. Slusher and C.M. Surko for their discussions on CO_2 laser scattering of lower hybrid waves, P. Bonoli for pointing out the possibility of drift wave scattering causing increased lower hybrid wave accessibility, T. Antonsen and R. Englade for discussions on energetic ion tails and for 1 - D transport code calculations of rf heating on Alcator A, A Gondhalekar for his discussions on Alcator A energy transport, J. Rice for his discussions on soft x-ray measurements of T_e, and for the engineering help of G. Chihoski and H. Israel.

This work was supported by D.O.E. Contract No. DE-AC02-78ES1013.A002.

References

* Waveguide array nosepiece built by Varian Assoc., Palo Alto, CA.

1. S. Bernabei, et. al., in Proceedings of the Third Symposium on Plasma Heating in Toroidal Devices, Varenna, Italy, 1974, edited by E. Sindoni (Editrice Compositori, Bologna, 1976), p. 68.

2. M. Porkolab, et. al., Phys Rev. Lett. 38, 230 (1977).

3. A.H. Kritz, et. al., Nucl. Fusion 18, 835 (1978).

4. S. Suckewer and E. Hinnov, Nucl. Fusion 17, 945 (1977).

5. C. Gormezano, et. al., in Proceedings of the Third Topical Conference on Radio Frequency Plasma Heating, California Institute of Technology, Pasadena, Cal., 1978, paper A3.

6. C.M. Singh, P. Briand, and L. Dupas, in Proceedings of the Third Topical Conference on Radio Frequency Plasma Heating, California Institute of Technology, Pasadena, Cal., 1978, paper B3.

7. P. Briand, et. al., in Proceedings of the Seventh International Conference on Plasma Physics and Controlled Nuclear Fusion, Innsbruck, Austria, 1978 (International Atomic Energy Agency, Vienna, Austria, 1979).

8. T. Nagashima and N. Fujisawa, in Proceedings of the Joint Varenna-Grenoble International Symposium on Heating in Toroidal Plasma, Grenoble, France, 3-7 July 1978, edited by T. Consoli and P. Caldirola (Pergamon, Elmsford, N.Y. 1979), Vol. II, p. 281.

9. T. Imai, T. Nagashima, T. Yamamoto, K. Vehara, S. Konoshima, H. Takeuchi, H. Yoshida and N. Fujisawa, Phys. Rev. Lett. 43, 536 (1979).

10. K. Ohkubo, K. Matsuura and JIPP T-II Group, Report IPPJ-366 (Nagoya University, Nagoya 464 Japan) Feb. 1979.

11. J.L. Luxon, et. al., Bull. Am. Phys. Soc., 23, 821 (1978).

12. J.J. Schuss, S. Fairfax, B. Kusse, R.R. Parker, M. Porkolab, D. Gwinn, I. Hutchinson, E.S. Mamar, D. Overskei, D. Pappas, L.S. Scaturro, and S. Wolfe, Phys. Rev. Lett. 43, 274 (1979).

13. C.M. Surko, R.E. Slusher, J.J. Schuss, R.R. Parker, I.H. Hutchinson, D. Overskei, and L.S. Scaturro, Phys. Rev. Letters 43, 1016 (1979).

14. T. H. Stix, Phys. Rev. Lett. 15 878 (1965).

15. R.J. Briggs and R.R. Parker, Phys. Rev. Lett. 29, 852 (1972).

16. M.D. Simonutti, Phys. Fluids 18, 1524 (1975).

17. P.M. Bellan and M. Porkolab, Phys. Fluids 17, 1592 (1974).

18. F. Troyan and F.W. Perkins, in Proceedings of the Second Topical Conference on RF Plasma Heating (Texas Tech. Univ., Lubbock Texas, 1974), paper B4.

19. J.J. Schuss, Phys. Fluids 18, 1178 (1975).

20. M. Brambilla, Nucl. Fusion 18, 493 (1978).

21. R.L. Berger, F.W. Perkins, and F. Troyon, Princeton Plasma Physics Laboratory Report No. PPPL-1366, (Princeton University, Princeton, N.J.) August 1977.

22. A. Bers, in Proceedings of the Third Symposium on Plasma Heating in Toroidal Devices, Varenna, Italy, 1974, edited by Editrice Compositori, Bologna, 1976), p. 99.

23. T.H. Stix, The Theory of Plasma Waves (McGraw-Hill Book Company, Inc., New York) 1962.

24. M. Brambilla, Plasma Physics 18, 669 (1976).

25. P.M. Bellan, in Proceedings of the Third Topical Conference on Radio Frequency Plasma Heating, California Institute of Technology, Pasadena, Cal., 1978, paper E1.

26. J.J. Schuss, M. Porkolab and R.R. Parker, in Proceedings of the Third Topical Conference on Radio Frequency Plasma Heating, California Institute of Technology, Pasadena, Cal., 1978, paper E2.

27. S. Bernabei, M.A. Heald, W.M. Hooke, and F.J. Paoloni, Phys. Rev. Lett 34, 866 (1975).

28. P. Lallia, in Proceedings of 2nd Topical Conference on RF Plasma Heating (Lubbock, 1974), paper C3.

29. M. Brambilla, Nucl. Fusion 16, 47 (1976).

30. S. Bernabei, M.A. Heald, W.M. Hooke, R.W. Motley, F.J. Paoloni, M. Brambilla, and W.D. Getty, Nucl. Fusion. 17, 929 (1977).

31. V. Krapchev and A. Bers, Nucl. Fusion 18, 519 (1978).

32. Y.F. Baranov and O.N. Shcherbinin, Proc. of the III Int. Meeting on Toroidal Plasma Heating, Grenoble, 1976; Fizika Plasmy 3, 246 (1977); [Sov. Phys. Plasma Phys. 3, 136 (1977)].

33. O.N. Shcherbinin and J.J. Schuss, Nucl. Fusion 19, 1675 (1979).

34. M. Brambilla, Nucl. Fusion 19, 1343 (1979).

35. J.J. Schuss, (to be published in Nuclear Fusion).

36. M. Porkolab, Phys. Fluids 17, 1432 (1974).

37. M. Porkolab, Phys. Fluids 20, 2058 (1977).

38. M. Porkolab, Nucl. Fusion 18, 367 (1978).

39. K.L. Wong, P. Bellan and M. Porkolab, Phys. Rev. Lett. 40, 554 (1978).

40. K.L. Wong, J.R. Wilson and M. Porkolab, Princeton Plasma Physics Laboratory Report No. 1499 (Princeton University, Princeton, N.J.) Feb. 1979; also Phys. Fluids 23, 96 (1980).

41. M.N. Rosenbluth, Phys. Rev. Lett. 29, 565 (1972).

42. D. Pesme, G. Laval, and R. Pellat, Phys. Rev. Lett. 31, 203 (1973).

43. A.K. Sundaram and P.K. Kaw, Nucl. Fusion 13, 901 (1973).

44. K.L. Wong and P.M. Bellan, Phys. Fluids 21, 841 (1978).

45. R.E. Slusher and C.M. Surko, Phys. Rev. Lett. 40, 400, 593(E)(1978).

46. R.L. Berger, L. Chen, P.K. Kaw, and F.W. Perkins, Phys. Fluids 20, 1864 (1977).

47. A. Sen and N.J. Fisch, Bull. Am. Phys. Soc. 23, 789 (1978).

48. J.Y. Hsu, S.C. Chiu, and V.S. Chan, Bull. Am. Phys. Soc. 23, 789 (1978).

49. E. Ott, Phys. Fluids 22, 1732 (1979); and Erratum, Phys. Fluids 23, 421 (1

50. P.M. Bellan and K.L. Wong, Phys. Fluids 21, 592 (1978).

51. P.T. Bonoli, E. Ott, J.-M. Wersinger, T.M. Antonsen, M. Porkolab, and R. Englade, Bull. Am. Phys. Soc. 24, 1020 (1979).

52. C.F.F. Karney and A. Bers, Phys. Rev. Lett. 39, 550 (1977),

53. J.Y. Hsu, K. Matsuda, M.S. Chu and T.H. Jensen, Phys. Rev. Lett. 43, 203 (1979).

54. C.F.F. Karney, Phys. Fluids 21, 1584 (1978).

55. C.F.F. Karney, Phys. Fluids 22, 2188 (1979).

56. J.A. Rome, D.G. McAlees, J.D. Callen, and R.H. Fowler, Nucl. Fusion 16, 55 (1976).

57. R.J. Goldston, Ph.D. Thesis, Princeton University, 1977.

58. L. Spitzer, Jr., Physics of Fully Ionized Gases (John Wiley & Sons, Inc., New York) 1962.

59. T.E. Stringer, Nucl. Fusion 12, 689 (1972).

60. J.W. Connor, R.J. Hastie, Nucl. Fusion 13, 221 (1973).

61. J.N. Davidson, Nucl. Fusion 16, 731 (1976).

62. K.T. Tsang, Nucl. Fusion 17, 557 (1977).

63. D.L. Jassby, H.H. Towner, R.J. Goldston, Nucl. Fusion 18, 825 (1978).

64. R.J. Goldston and H.H. Towner, Bull. Am. Phys. Soc. 24, 1045 (1979).

65. M. Greenwald, J.J. Schuss, D. Cope (to be published).

66. J.J. Schuss (to be published).

67. A. Gondhalekar, et. al., In Proceedings of the Seventh International Conference on Plasma Physics and Controlled Nuclear Fusion Research, Innsbruck, Austria 1978 (International Atomic Energy Agency, Vienna, Austria, 1979).

68. L.S. Scaturro and B. Kusse, Nucl. Fusion 18, 1717 (1978).

69. D.S. Pappas, R.R. Parker, M.I.T. Plasma Fusion Center Research Report No. 5, Feb. 1978.

70. D. Gwinn, J.J. Schuss, W. Fisher, Bull. Am. Phys. Soc. 24, 998 (1979).

71. A. Gondhalekar, private communication.

72. D.J. Rose and M. Clark, in Plasmas and Controlled Fusion (M.I.T. Press, Cambridge, Mass., 1961).

73. R. Englade, T. Antonsen and M. Porkolab, Bull. Am. Phys. Soc. 23, 766 (1978).

FIGURE CAPTIONS

Fig. 1. k_x and $P(x) = P_o \exp(-2 \int \mathrm{Im} k_x dx)$ (arbitrary units) graphed vs. r is a slab geometry, f = 2.45 GHz. A parabolic density profile and gaussian $T_e(r) = T_{eo} \exp(-r^2/r_T^2)$ are taken, with r_T = 6 cm. (a) $\bar{n}_e = 2 \times 10^{14} cm^{-3}$, B_T = 60 kG, T_e = 900 eV, T_i = 800 eV, deuterium, and n_z = 5. Mode conversion occurs at a maximum $k_x = 495\ cm^{-1}$. (b) Same as (a), except $\bar{n}_e = 1.6 \times 10^{14} cm^{-3}$ and now maximum $k_x = 358\ cm^{-1}$. In (a) and (b) only ion damping is included. (c) Electron damping is included, $\bar{n}_e = 1.2 \times 10^{14} cm^{-3}$, T_e = 1100 eV and T_i = 700 eV; the rest is identical to (a) and (b). The maximum $k_x = 279\ cm^{-1}$ and the wave is subject to strong electron Landau damping.

Fig. 2. Schematic of waveguide-plasma coupling geometry. $\nabla n \| \hat{x}$ and $\omega = \omega_{pe}$ at x = L. There are N waveguides of width b at positions $z_1, z_2, \ldots z_N$. The incident $\vec{E}$ in each guide is parallel to $\vec{B}$.

Fig. 3. (a) Theoretical global reflectivity R vs. ∇n for $\Delta\phi = 0$ and $\Delta\phi = \pi$. b = 1.275 cm, f = 2.45 GHz, and a 0.09 cm septum separates the two waveguides. (b) $P(n_z)$ and $\int_1^{n_z} P(\xi) d\xi$ for the waveguide array of (a) for $\Delta\phi = \pi$ and $\Delta\phi = 0$. For $\Delta\phi = 0$ the power is compressed in the portion of the n_z spectrum that can only access the plasma edge. In both cases R $\sim$ 18%.

Fig. 4. Wave scattering geometry. $\tan\vartheta = B_{po}/B_{TO}$, $k_{\perp\perp}$ is in the poloidal plane and perpendicular to $\vec{B}_o$ and $\vec{k}_{\|} \| \vec{B}_o$.

Fig. 5. Profiles of $k_{\perp r}$, $k_{\perp\perp}$, $n_{||}$, and P(r), the rf power flux density, for $\bar{n}_e = 2 \times 10^{14} cm^{-3}$, $B_T = 62$ kG, $I_p = 150$ kA, deuterium, and $n_{||}(a) = 2.7$. The edge density is 0.1 times the central density, (a) $\alpha = 0$, (b) $\alpha = -0.707$, and (c) $\alpha = 0.707$. In each figure the relative $k_{\perp\perp}$ and $k_{\perp r}$ are graphed.

Fig. 6. Profile of $k_{\perp r}$, $k_{\perp\perp}$ and $n_{||}$, for $\bar{n}_e = 7 \times 10^{13} cm^{-3}$, $B_T = 62$ kG, $I_p = 150$ kA, $n_{||}(a) = 1.3$ and deuterium. (a) $\alpha = 0$ and the wave doesn't penetrate (b) $\alpha = -0.3$ and the wave penetrates to within r = 1 cm. In each figure the relative $k_{\perp\perp}$ and $k_{\perp r}$ are graphed.

Fig. 7. (a) Heating predicted by a poloidal isotropization of $\vec{k}_\perp$ at the plasma edge for $\bar{n}_e = 1.6 \times 10^{14} cm^{-3}$, deuterium, $B_T = 80$ kG, $T_e = 1$ keV, $T_i = 800$ eV, $I_p = 150$ kA, and two out of phase waveguides having b = 1.275 cm. $n_e(a) = n_e(r=0) * 0.1$, and the scattering is done at r = a. Here P_{ABST} is the total absorbed power profile and P_{ABSI} is the ion absorbed power profile. The total power absorbed is 40% on the first pass, 90% of which is absorbed by ions. (b), (c), and (d) - $n_{||}$ power spectra at different radii for the same conditions as (a). (b) - r = 10 cm, (c) - r = 5 cm, and (d) - r = 2 cm.

Fig. 8. P_{ABS} vs. r for $\bar{n}_e = 2 \times 10^{14} cm^{-3}$, deuterium, $B_T = 62$ kG, $T_e = 1$ keV, $T_i = 800$ eV, $I_p = 150$ kA, and two in phase waveguides having b = 1.275 cm. Here the total power abosrbed by the plasma is 22% on the first pass, 95% of which is absorbed by ions.

Fig. 9. Loss boundaries for deuterium ions in velocity space for B_T = 60 kG, a = 10 cm, R = 54 cm, I_p = 150 kA and the current profiles of Eq. (32). Each loss curve is generated for antiparallel ions at the minor radius indicated on the plasma midplane; the unconfined regime is above each curve. When $v_{||}/v = 0$, the loss energy E_L is: r = 1 cm - E_L = 104 keV, r = 3 cm - E_L = 96 keV, r = 5 cm - E_L = 68 keV, r = 7 cm - E_L = 36 keV, and r = 9 cm - E_L = 10 keV.

Fig. 10. Same loss boundaries as in Fig. a, except that I_p = 75 kA. Now when $v_{||}/v = 0$, E_L = 46 keV for r = 1 cm, E_L = 37 keV for r = 3 cm, E_L = 22 keV for r = 5 cm, E_L = 10 keV for r = 7 cm, and E_L = 3 keV for r = 9 cm.

Fig. 11. Minimum unconfined energy vs. r for deuterium ions and B_T = 60 kG, a = 10 cm, R = 54 cm, and I_p = 100 kA, 150 kA, and 200 kA as shown.

Fig. 12. Minimum unconfined energy vs. r for deuterium ions and B_T = 60 kG, I_p = 150 kA and R = 54 cm. A different curve is plotted for effective ion loss radii of 10 cm, 9 cm, 8 cm, 7 cm and 6 cm. At a given radius an ion having an energy greater than that given by the curve can scatter into a orbit that crosses that loss radius.

Fig. 13. Schematic of Alcator A access ports during lower hybrid experiment (top view) a = 10 cm, a' = 12.7 cm, b = 1.275 cm, d = 1 cm, and R = 54 cm.

Fig. 14. Global reflectivity R_T vs. relative waveguide phase ϕ with the center of the waveguide mouth at r = 10 cm; B_T = 60 kG, deuterium, and □ - $\bar{n}_e = 0.5 \times 10^{14} cm^{-3}$, x - $\bar{n}_e = 3 \times 10^{14} cm^{-3}$. Theoretical curves are presented for $\nabla n = 9 \times 10^{15} cm^{-4}$ and $\nabla n = 1.1 \times 10^{15} cm^{-14}$.

Fig. 15. R_T vs. position of center of waveguide mouth for B_T = 60 kG, deuterium, and ϕ = 180°. x - $\bar{n}_e = 1 \times 10^{14} cm^{-3}$ and • - $\bar{n}_e = 0.5 \times 10^{14} cm^{-3}$.

Fig. 16. R_T vs. total incident rf power P_{rf} for ϕ = 180°, B_T = 60 kG, deuterium, $\bar{n}_e = 1.7 \times 10^{14} cm^{-3}$ and r = 12.1 cm.

Fig. 17. R_T vs. ϕ for r = 12.1 cm, B_T = 60 kG, deuterium, $\bar{n}_e \sim 1.7 \times 10^{14} cm^{-3}$; □ - P_{rf} = 85 kW and x - P_{rf} = 32 kW.

Fig. 18. R_T vs. ϕ for B_T = 62 kG, $\bar{n}_e \sim 1 \times 10^{14} cm^{-3}$, deuterium, and P_{rf} = 75 kW. • - r = 12.1 cm, □ - r = 11.1 cm, and Δ - r = 10.6 cm.

Fig. 19. Balance B vs. time for three different shots at increasing P_{rf}; B_T = 60 kG, r = 12.1 cm, ϕ = 180°, and $\bar{n}_e \sim 1.5 \times 10^{14} cm^{-3}$. The last shot shows wild variations in B.

Fig. 20. Forward and reflected powers for two different shots having r = 12.1 cm and r = 11.1 cm; B_T = 60 kG, $\bar{n}_e \sim 0.5 \times 10^{13} cm^{-3}$, and $\phi = 180°$.

Fig. 21. Raw data from breakdown test of waveguides having ceramic vacuum windows near array mouth; V_L = loop voltage, I_p = plasma current, and the lowest four traces are crystal outputs proportional to the forward and reflected powers in each waveguide. The peak forward rf power is 90 kW. There is no sign of rf breakdown.

Fig. 22. (a) R_T vs. P_{rf} for waveguides with ceramic vacuum windows near the array mouth; $\phi = 180°$, r = 12.1 cm, B_T = 60 kG, deuterium and o - $\bar{n}_e = 1.8 \times 10^{14} cm^{-3}$, • - $\bar{n}_e = 2.7 \times 10^{14} cm^{-3}$, x - $\bar{n}_e = 3 \times 10^{14} cm^{-3}$, (b) same as (a), except now P_{rf} = 90 kW and R_T is graphed vs. $\bar{n}_e$. • - r = 12.1 cm and □ - r = 11.95 cm.

Fig. 23. Raw data from exciting only one of two waveguides at P_{rf} = 80 kW, leading to $P_{rf}/A \sim 8$ kW/cm^2. The lowest trace is a crystal voltage proportional to P_{rf}. The reflected power is less than 0.03 P_{rf} and there is no evidence of rf breakdown. Here B_T = 60 kG, and a deuterium discharge is employed.

Fig. 24. (a) V_R, I_p, $\bar{n}_e$ and neutron rate vs. time during a typical plasma shot with P_{rf} = 90 kW, ϕ = 180°, B_T = 62 kG, and the face of the array at r = 12.1 cm. The rf pulse is turned on and off as indicated. (b) Neutron rate enhancement vs. $\bar{n}_e$ for many plasma shots; P_{rf} = 90 kW, ϕ = 180°, B_T = 62 kG and I_p = 150 kA.

Fig. 25. Neutron rate enhancement vs. $\bar{n}_e$ for B_T = 80 kG, and I_p = 200 kA; the remaining conditions are identical to Fig. 24b.

Fig. 26. Neutron rate enhancement vs. $\bar{n}_e$ for the same conditions as Fig. 24b, except that the face of the array is at r = 10.6 cm.

Fig. 27. Expanded neutron rate and central chord soft x-ray rate vs. time for P_{rf} = 90 kW, ϕ = 180°, $\bar{n}_e = 1.6 \times 10^{14} cm^{-3}$, B_T = 60 kG, I_p = 150 kA, and a deuterium discharge. The correlation between the neutron and x-ray sawteeth is evident.

Fig. 28. Relative neutron rate of collimated neutron detector vs. distance of viewed chord from plasma center. Each point is the sum of the total neutron yield of many shots; however, on each shot the total neutron yield due to the rf pulse was at least an order of magnitude greater than the thermal yield.

Fig. 29. Neutron rate vs. ϕ for P_{rf} = 90 kW, $\bar{n}_e = 1.6 \times 10^{14} cm^{-3}$, B_T = 60 kG, I_p = 150 kA and the face of the array at r = 12.1 cm.

Fig. 30. Neutron rate vs. average P_{rf} for $\bar{n}_e \simeq 1.7 \times 10^{14} cm^{-3}$, B_T = 62 kG, I_p = 150 kA, ϕ = 180° and the face of the array at r = 12.1 cm.

Fig. 31. Perpendicular charge exchange energy spectra before, during, and after the rf pulse during neutron enhancement for B_T = 62 kG and P_{rf} = 90 kW. In the absence of rf $T_i \simeq 750$ eV. The cutoff of neutrals for $E_i > 5$ keV due to the ∇B drift is apparent.

Fig. 32. 6.6 keV and 9.8 keV fast neutral deuterium flux vs. radius of viewed chord during rf produced neutron enhancement at $\bar{n}_e = 1.6 \times 10^{14} cm^{-3}$, B_T = 62 kG, I_p = 150 kA, P_{rf} = 90 kW and ϕ = 180°, x = 6.6 keV and • = 9.8 keV.

Fig. 33. Enhancement in 8 keV neutral hydrogen flux vs. $\bar{n}_e$ for B_T = 62 kG, I_p = 150 kA, P_{rf} = 90 kW and ϕ = 180°.

Fig. 34. Raw data from low density electron heating shot: V_R, I_p, $\bar{n}_e$, central soft x-rays, in-out plasma position loop (up is outward), $\omega = 2\omega_{ce}$ electron cyclotron emission and rf power. P_{rf} = 80 kW, ϕ = 180°, B_T = 62 kG, and deuterium gas.

Fig. 35. $T_e(r)$ vs. r from $\omega = 2\omega_{ce}$ emission with and without rf power for two identical plasma shots; $\bar{n}_e = 1.2 \times 10^{14} cm^{-3}$, $P_{rf} = 50$ kW, $B_T = 60$ kG, $\phi = 180°$, and a deuterium discharge. The arrows indicates the expected optical thickness of the emitting layer, τ, at a given radius.

Fig. 36. Experimental bands of neutron or fast ion enhancement and theoretical predictions of the central density n_{eo} at which mode conversion should occur at vs. B_T for the indicated parameters. □ = fast ion band in hydrogen discharges and • = neutron enhancement band in deuterium. The plasma conditions used to calculate the curves are those during rf injection.

Fig. 37. (a) High frequency rf probe spectrum; $B_T = 62$ kG, deuterium, $\bar{n}_e = 2.1 \times 10^{14} cm^{-3}$ and $P_{rf} = 30$ kW. The peaks at the edges of the graphs are caused by the spectrum analyzer resetting. (b) Low frequency rf probe spectrum at $B_T = 62$ kG, deuterium, $\bar{n}_e = 1.6 \times 10^{14} cm^{-3}$, and $P_{rf} = 90$ kW.

Fig. 38. RF probe spectra at $B_T = 82$ kG, deuterium, $I_p = 200$ kA and $P_{rf} = 90$ kW at three different values of $\bar{n}_e$.

Fig. 39. Higher frequency resolution rf probe spectra. (a) High frequency spectrum at $B_T = 62$ kG, deuterium, $\bar{n}_e = 2.8 \times 10^{14} cm^{-3}$, $I_p = 150$ kA and $P_{rf} = 80$ kW. The sudden decrease in amplitude occurred at the end of the rf pulse.

(b) Low frequency spectrum both with and without rf at B_T = 62 kG, deuterium, $\bar{n}_e = 1.6 \times 10^{14} cm^{-3}$, I_p = 150 kA and P_{rf} = 80 kW. The peak at 0 Hz is a reference maker.

Fig. 40. High frequency rf probe spectra at P_{rf} = 80 kW, B_T = 60 kG, deuterium and $\bar{n}_e = 1 \times 10^{14} cm^{-3}$ for both a 30 KHz and a 300 KHz instrument bandwidth. The sharp peak at 2.45 GHz in the 30 KHz signal is due to a frequency marker at the pump frequency.

Fig. 41. (a) Frequency integrated amplitude of rf probe signal at 2.45 GHz vs. $\bar{n}_e$ for a deuterium plasma, B_T = 62 kG, I_p = 150 kA and P_{rf} = 75 kW. The arrows indicate the value of n_z that will mode convert at the plasma center at the indicated value of $\bar{n}_e$. (b) FWHM of 2.45 GHz rf probe signal vs. $\bar{n}_e$ for the same conditions as (a).

Fig. 42. Frequency integrated 2.45 GHz rf probe signal vs. ϕ for $\bar{n}_e \simeq 1 \times 10^{14} cm^{-3}$, I_p = 150 kA, B_T = 62 kG, deuterium and P_{rf} = 75 kW. Face of waveguide array is at: Δ - r = 12.1 cm, $\circ$ - r = 11.1 cm, and $\bullet$ - r = 10.6 cm.

Fig. 43. Amplitude of frequency integrated rf probe signal at f = 2.45 GHz vs. P_{rf} for $\bar{n}_e = 3.2 \times 10^{14} cm^{-3}$, I_p = 150 kA, B_T = 62 kG, deuterium, and the face of the waveguide array at r = 12.1 cm.

Fig. 44. Frequency spectrum of reflected power in waveguide array for P_{rf} = 7 kW and P_{rf} = 200W; B_T = 62 kG, deuterium, I_p = 120 kA, $\bar{n}_e = 2.5 \times 10^{14} cm^{-3}$, and the face of the array at r = 12.1 cm. The spectrum analyzer has a 300 KHz bandwidth.

Fig. 45. Frequency spectrum of reflected power in the waveguide array for P_{rf} = 80 kW, B_T = 62 kG, deuterium, I_p = 100 kA, and the face of the array at r = 11.1 cm. The spectrum analyzer bandwidth was 300 KHz.

Fig. 46. (a) Pump reflected power vs. P_{rf} for $\bar{n}_e = 2.5 \times 10^{14} cm^{-3}$, B_T = 62 kG, deuterium, I_p = 120 kA, and the face of the array at r = 12.1 cm. In the shaded area the pump power was of the same order of magnitude as the sideband power. (b) Frequency integrated sideband amplitude vs. P_{rf} for the same conditions as (a).

Fig. 47. RF enhanced neutron rate 1/e decay time vs. I_p for $\bar{n}_e \sim 1.5 \times 10^{14} cm^{-3}$, P_{rf} = 85 kW, deuterium, and • = 62 kG, o = 80 kG.

Fig. 48. Neutron rate R_N and tail energy E_T vs. time for a factor of 50 increase in the neutron rate during rf. Here $n_e = 2.4 \times 10^{14} cm^{-3}$, T_e = 1 keV, T_i = 0.8 keV, and Δr = 3 cm. (a) T_T = 20 keV and E_{max} = 100 keV; now δ = 0.0013, P_T = 3.8 kW and τ_N = 1.75 msec. (b) T_T = 20 keV and E_{max} = 25 keV; δ = 0.036, P_T = 90 kW and τ_N = 0.64 msec. (c) T_T = 5 keV and E_{max} = 100 keV; δ = 0.085, P_T = 249 kW and τ_N = 0.8 msec

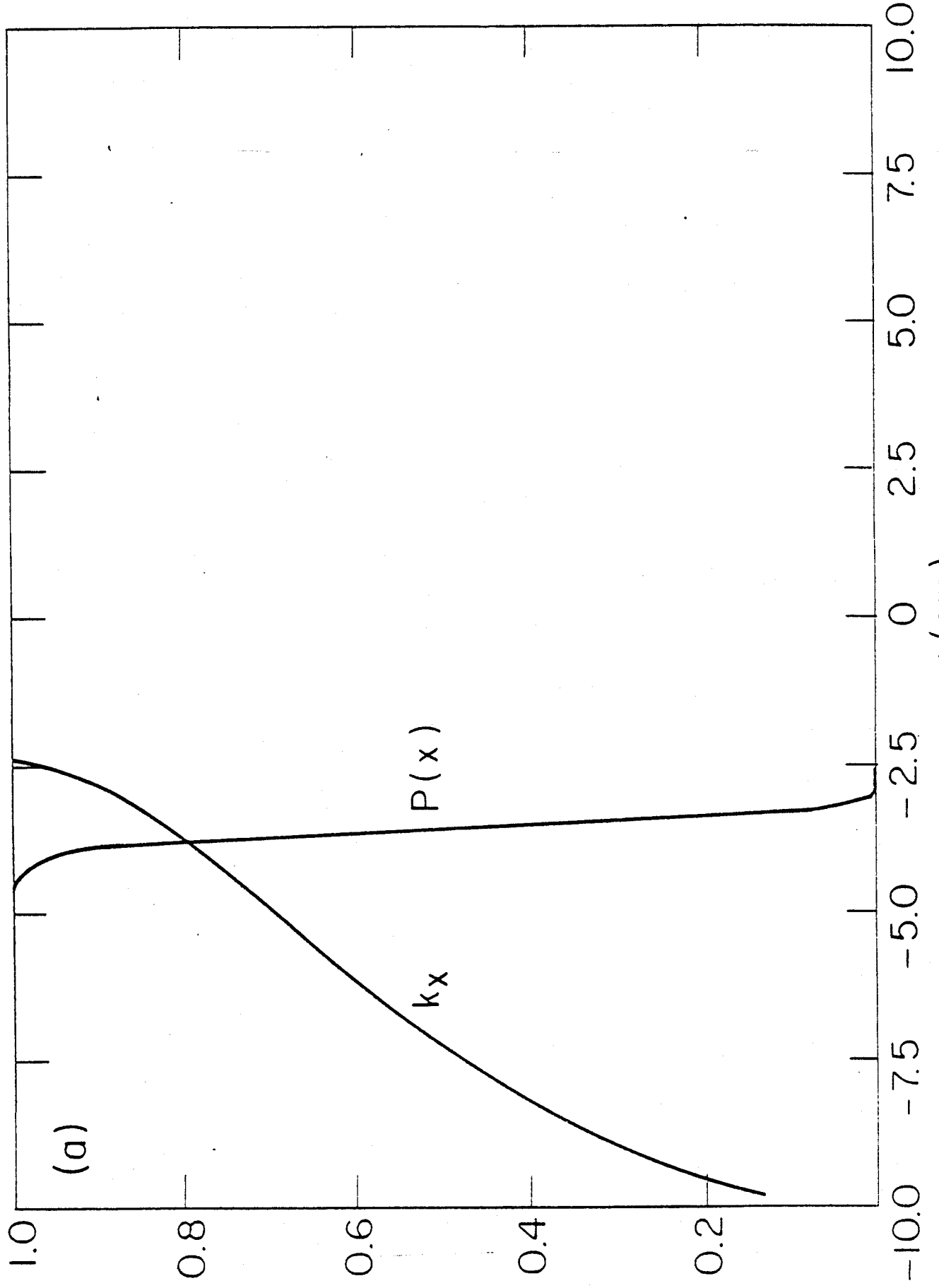

Fig. 1

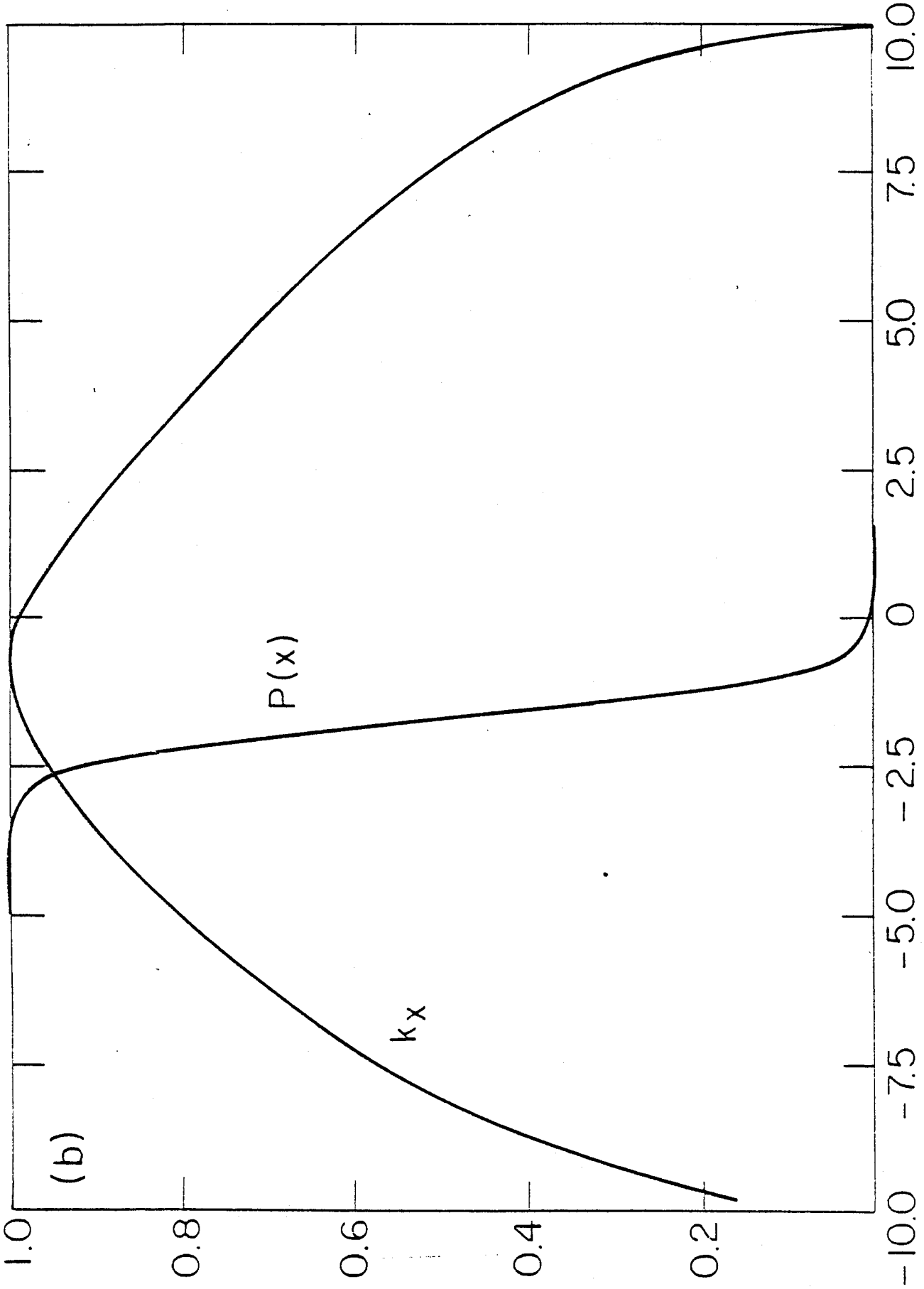

Fig. 1

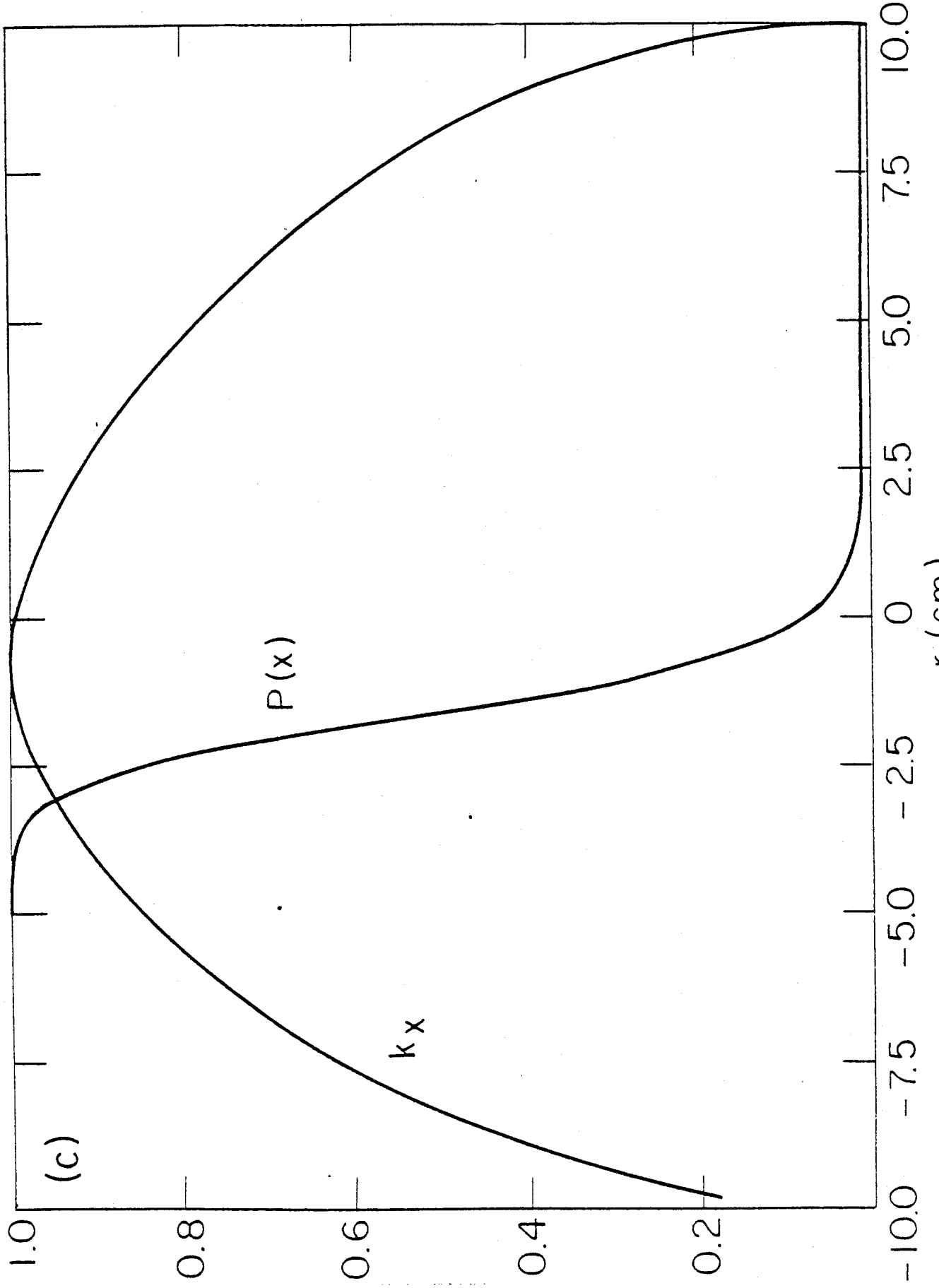

Fig. 1

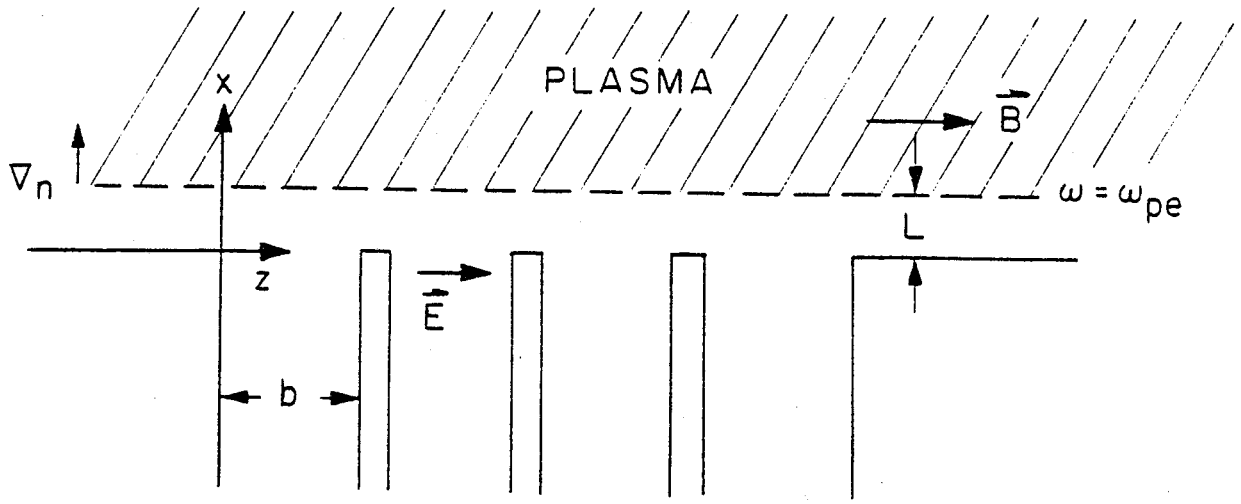

Fig. 2

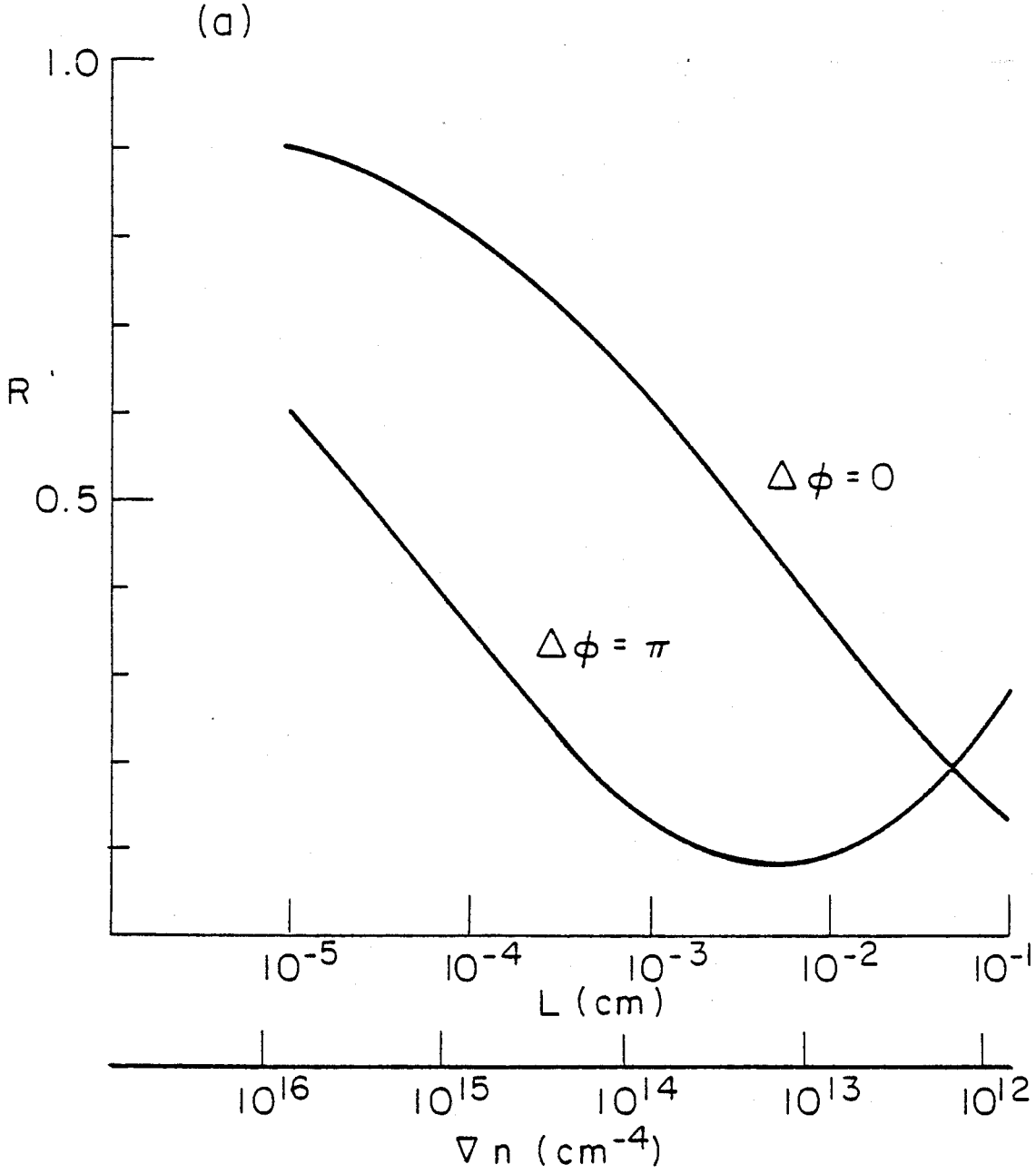
(a)
1.0
0.5
R
Δφ = 0
Δφ = π
10^-5
10^-4
10^-3
10^-2
10^-1
L (cm)
10^16
10^15
10^14
10^13
10^12
∇ n (cm^-4)

Fig. 3

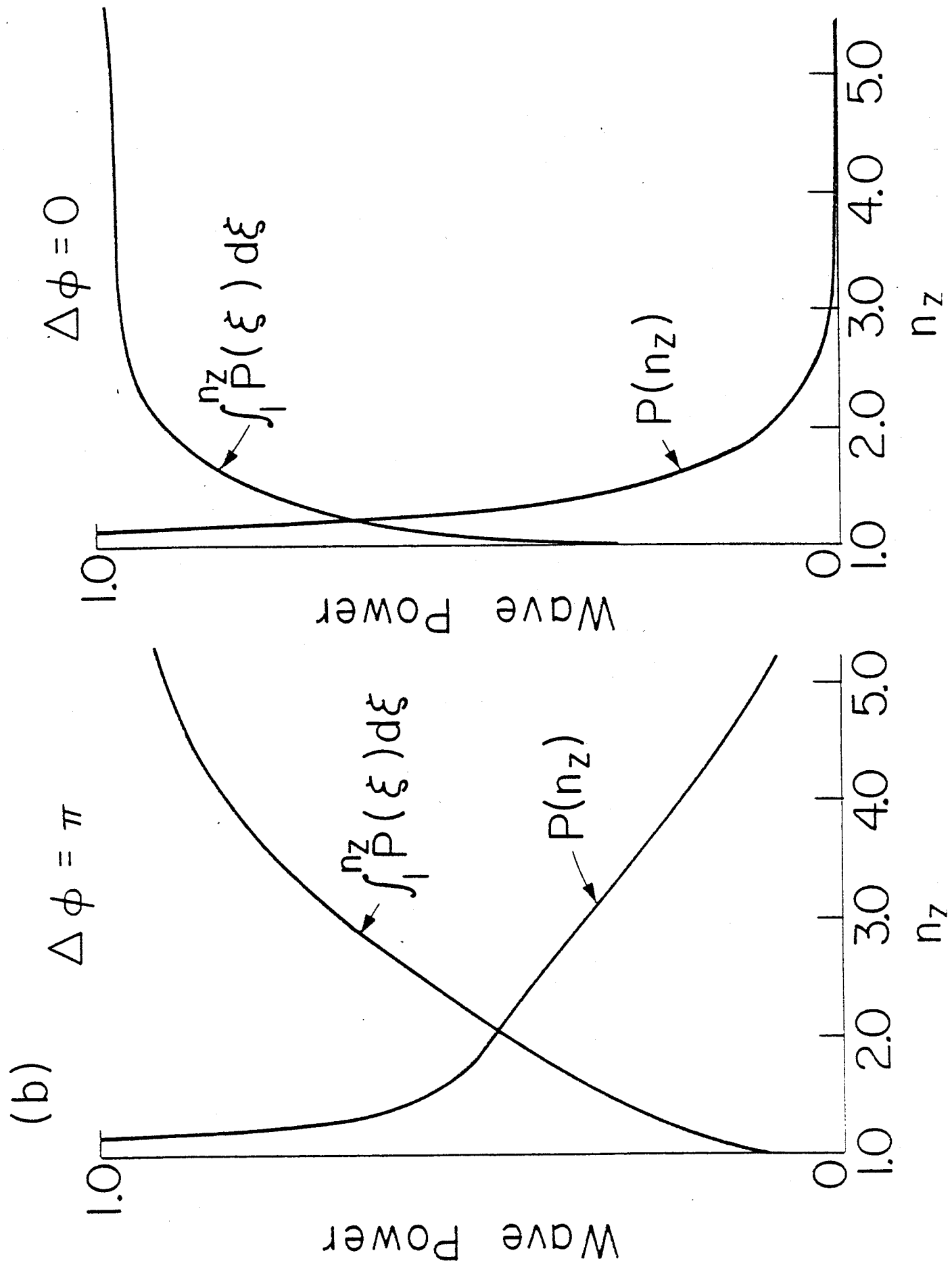

Fig. 3

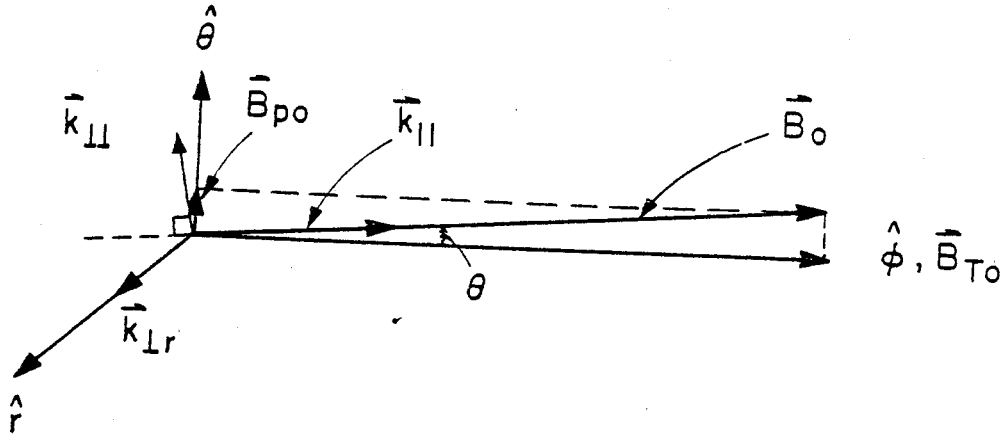
$\hat{\theta}$
$\vec{k}_{\perp\perp}$
$\vec{B}_{po}$
$\vec{k}_{\parallel}$
$\vec{B}_o$
$\hat{\phi}$, $\vec{B}_{To}$
θ
$\vec{k}_{\perp r}$
$\hat{r}$

Fig. 4

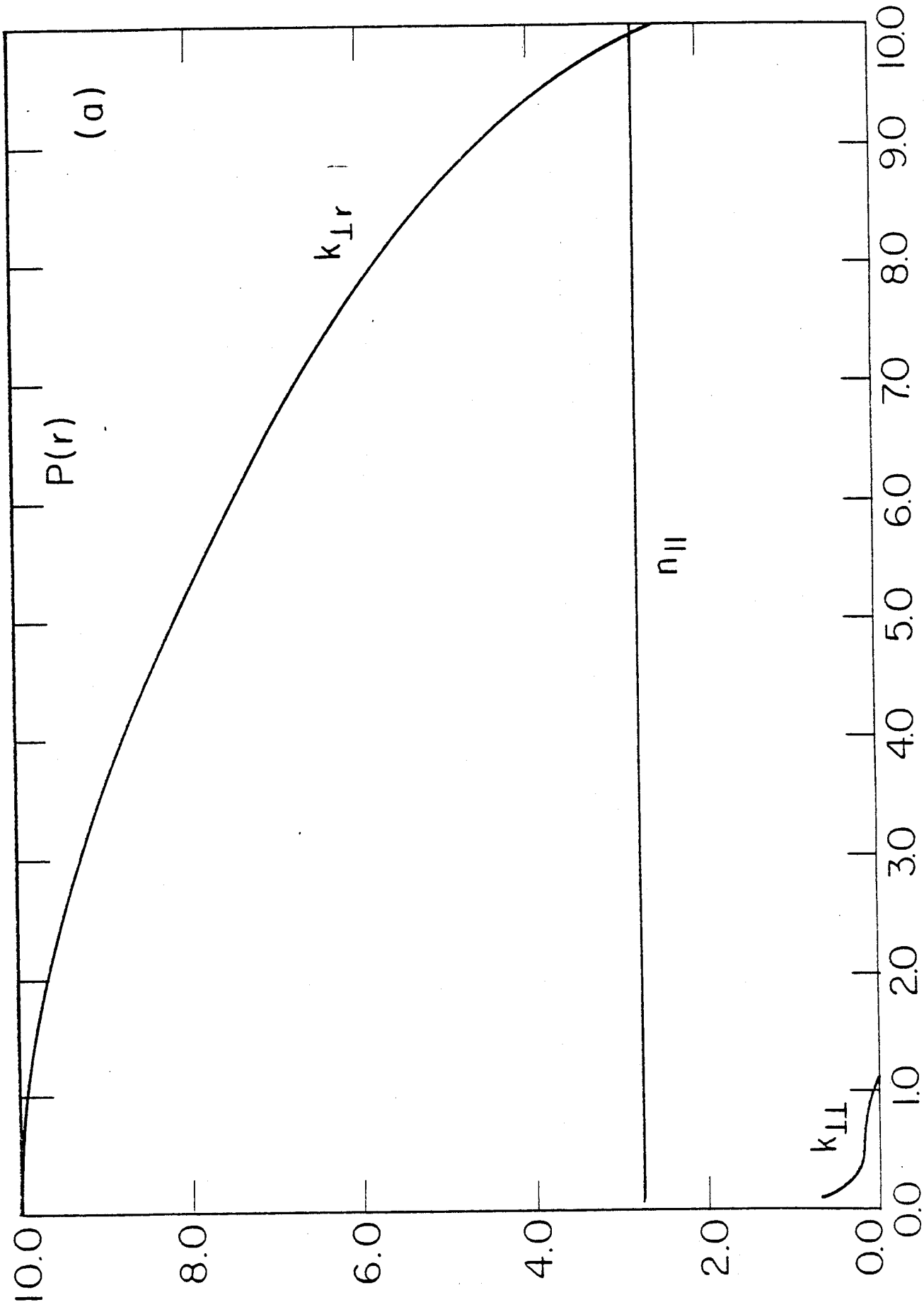
(a)
P(r)
$k_{\perp r}$
$n_{\parallel}$
$k_{\perp\perp}$
r (cm)
0.0
1.0
2.0
3.0
4.0
5.0
6.0
7.0
8.0
9.0
10.0
10.0
8.0
6.0
4.0
2.0
0.0

Fig. 5

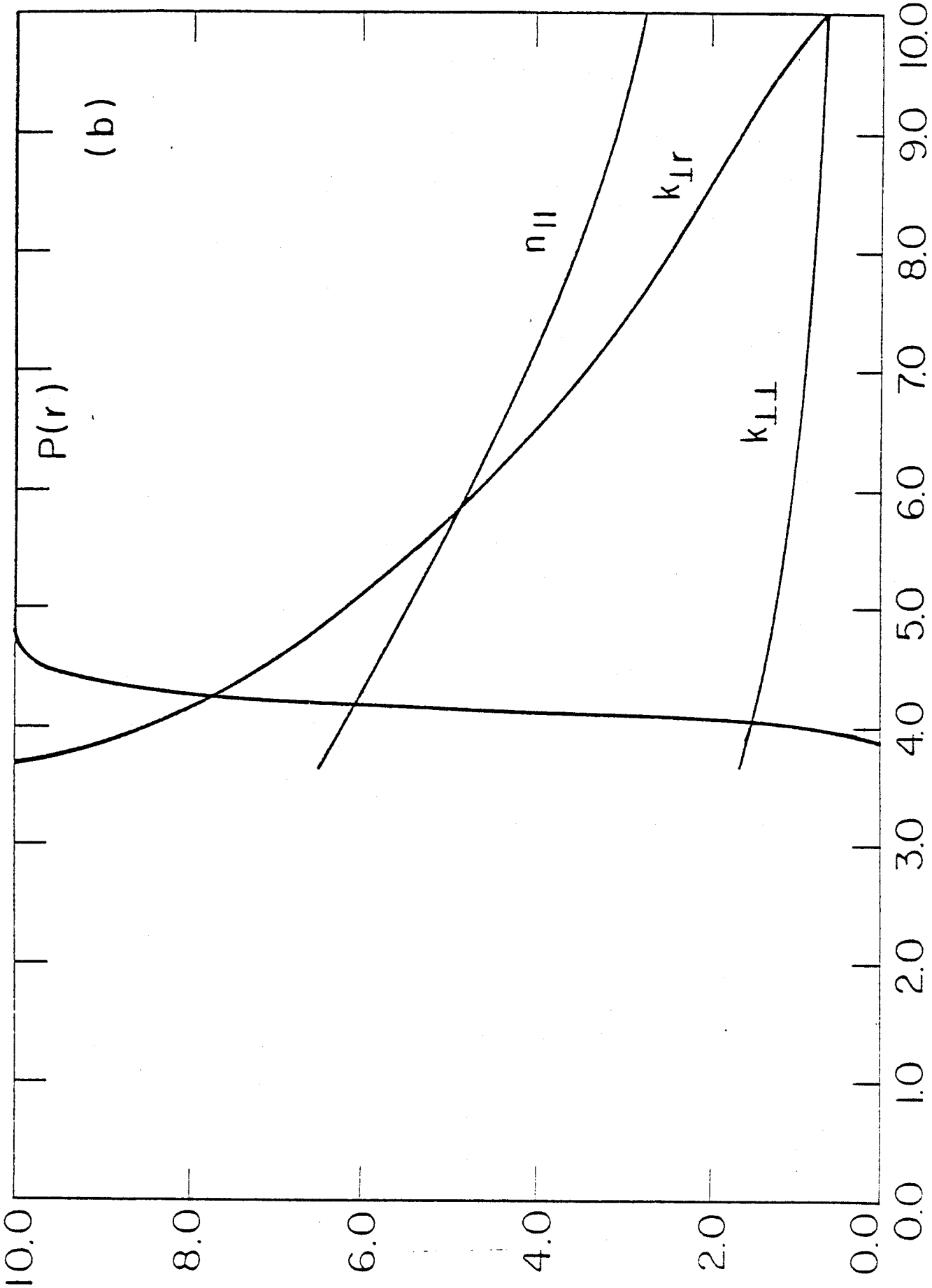
(b)
P(r)
$\eta_{\parallel}$
$k_{\perp r}$
$k_{\perp\perp}$
r (cm)
0.0
1.0
2.0
3.0
4.0
5.0
6.0
7.0
8.0
9.0
10.0
10.0
8.0
6.0
4.0
2.0
0.0

Fig. 5

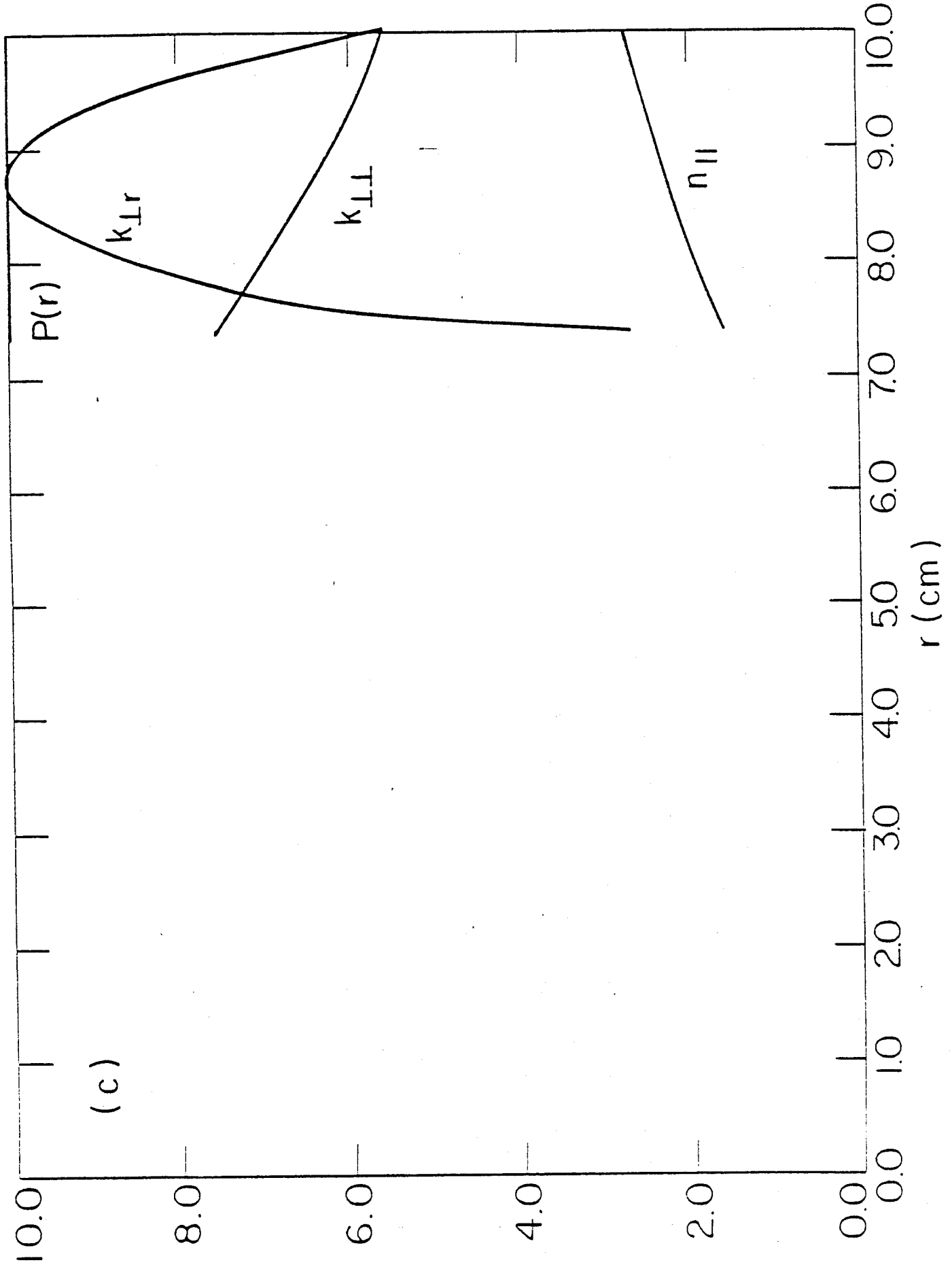
P(r)
$k_{\perp r}$
$k_{\perp\perp}$
$n_{\parallel}$
(c)
r (cm)
0.0
1.0
2.0
3.0
4.0
5.0
6.0
7.0
8.0
9.0
10.0
10.0
8.0
6.0
4.0
2.0
0.0

Fig. 5

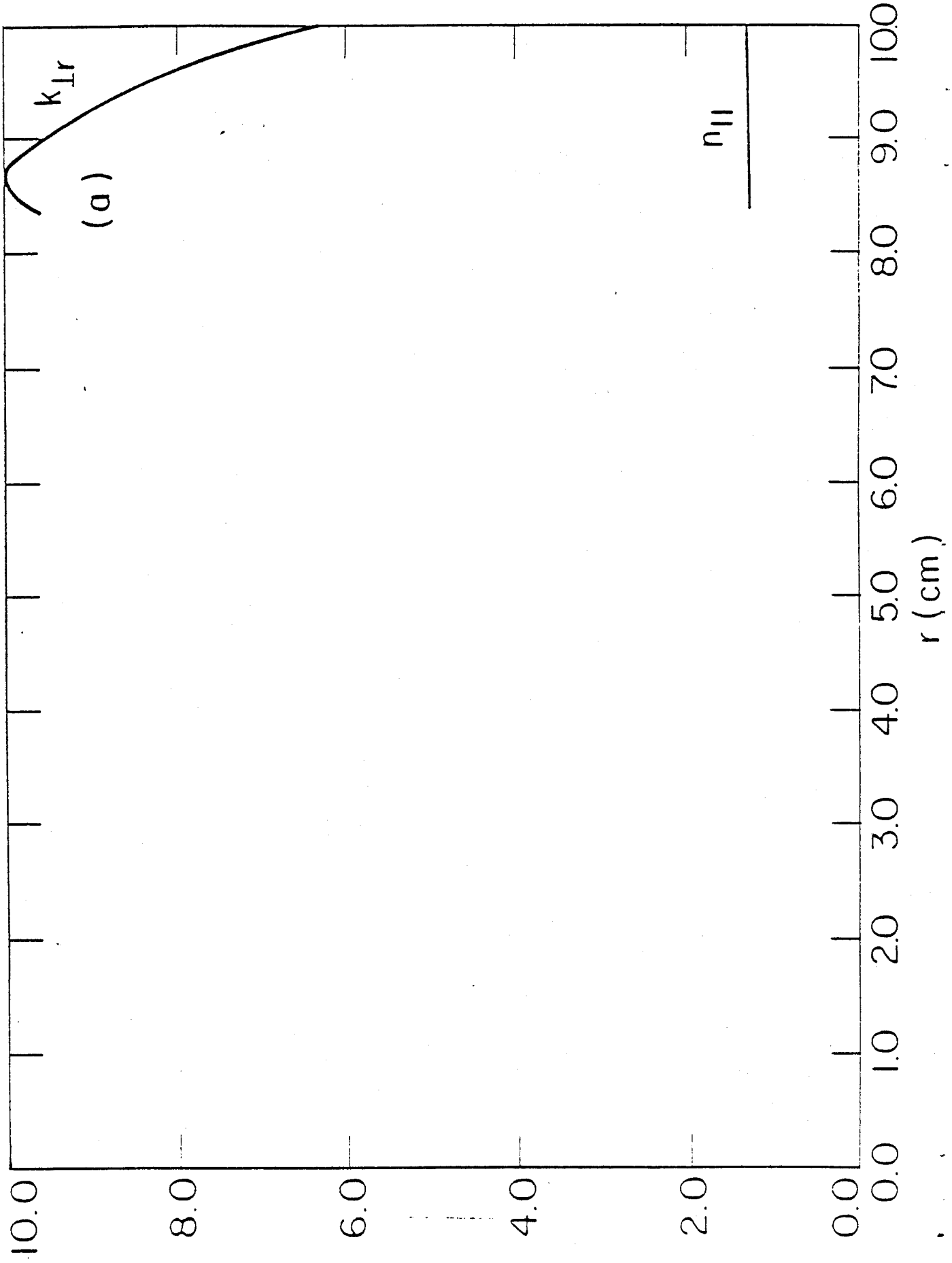
$k_{\perp r}$
(a)
$n_{\parallel}$
10.0
8.0
6.0
4.0
2.0
0.0
0.0
1.0
2.0
3.0
4.0
5.0
6.0
7.0
8.0
9.0
10.0
r (cm)

Fig. 6

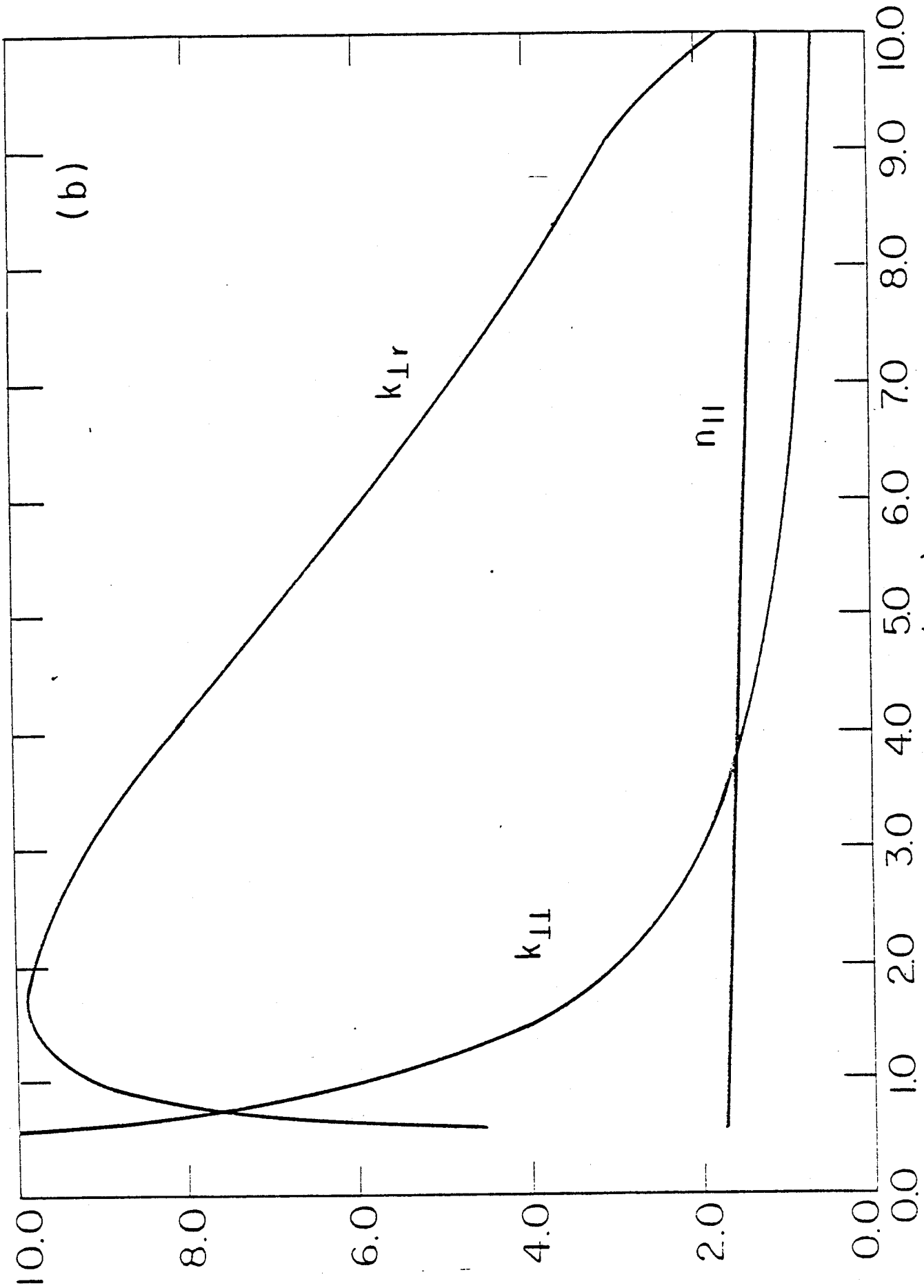
(b)
$k_{\perp r}$
$k_{\perp\perp}$
$n_{\parallel}$
r (cm)
0.0
1.0
2.0
3.0
4.0
5.0
6.0
7.0
8.0
9.0
10.0
0.0
2.0
4.0
6.0
8.0
10.0

Fig. 6

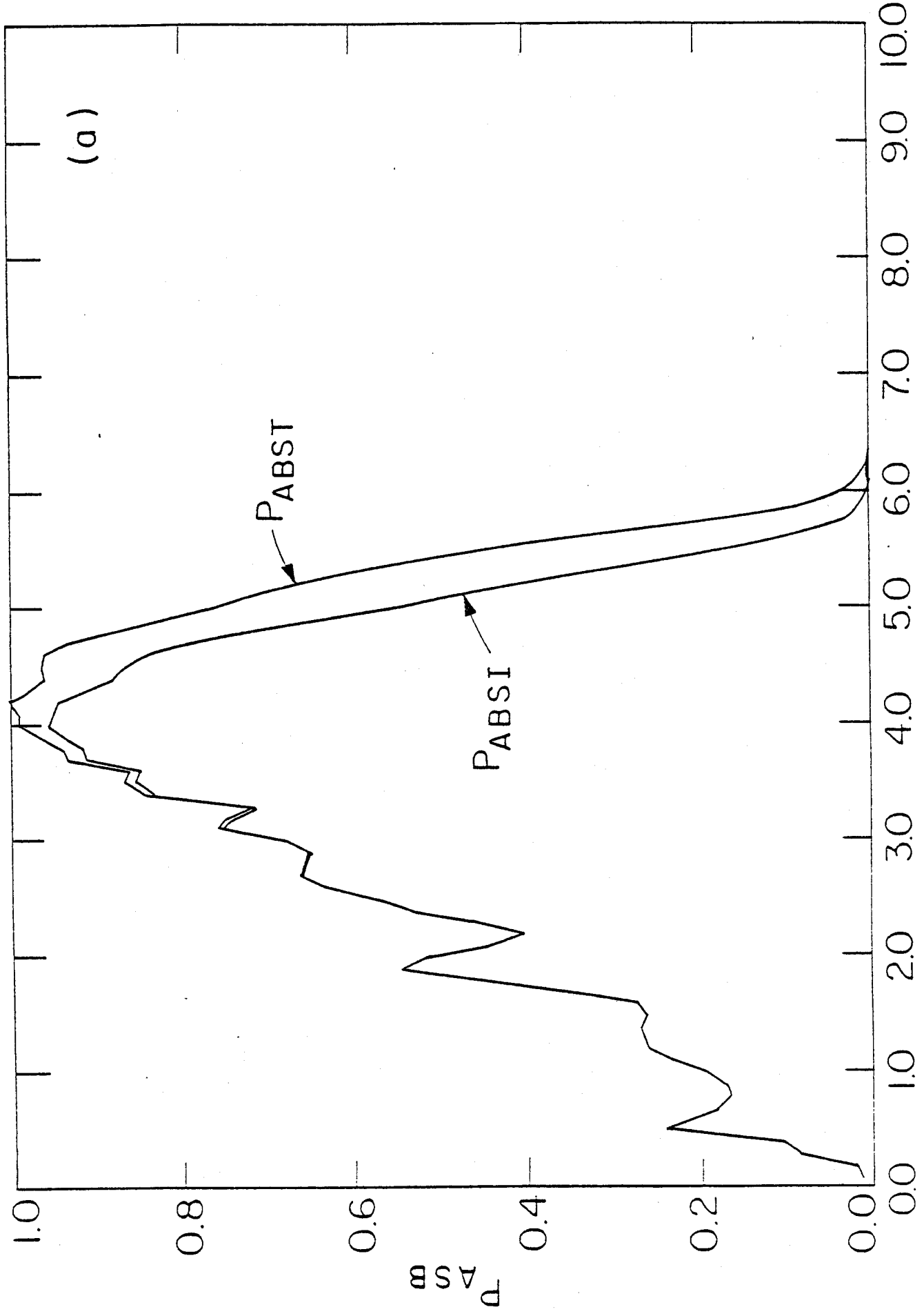
(a)
P_{ABST}
P_{ABSI}
P_{ASB}
r (cm)
0.0
0.2
0.4
0.6
0.8
1.0
1.0
2.0
3.0
4.0
5.0
6.0
7.0
8.0
9.0
10.0

Fig. 7

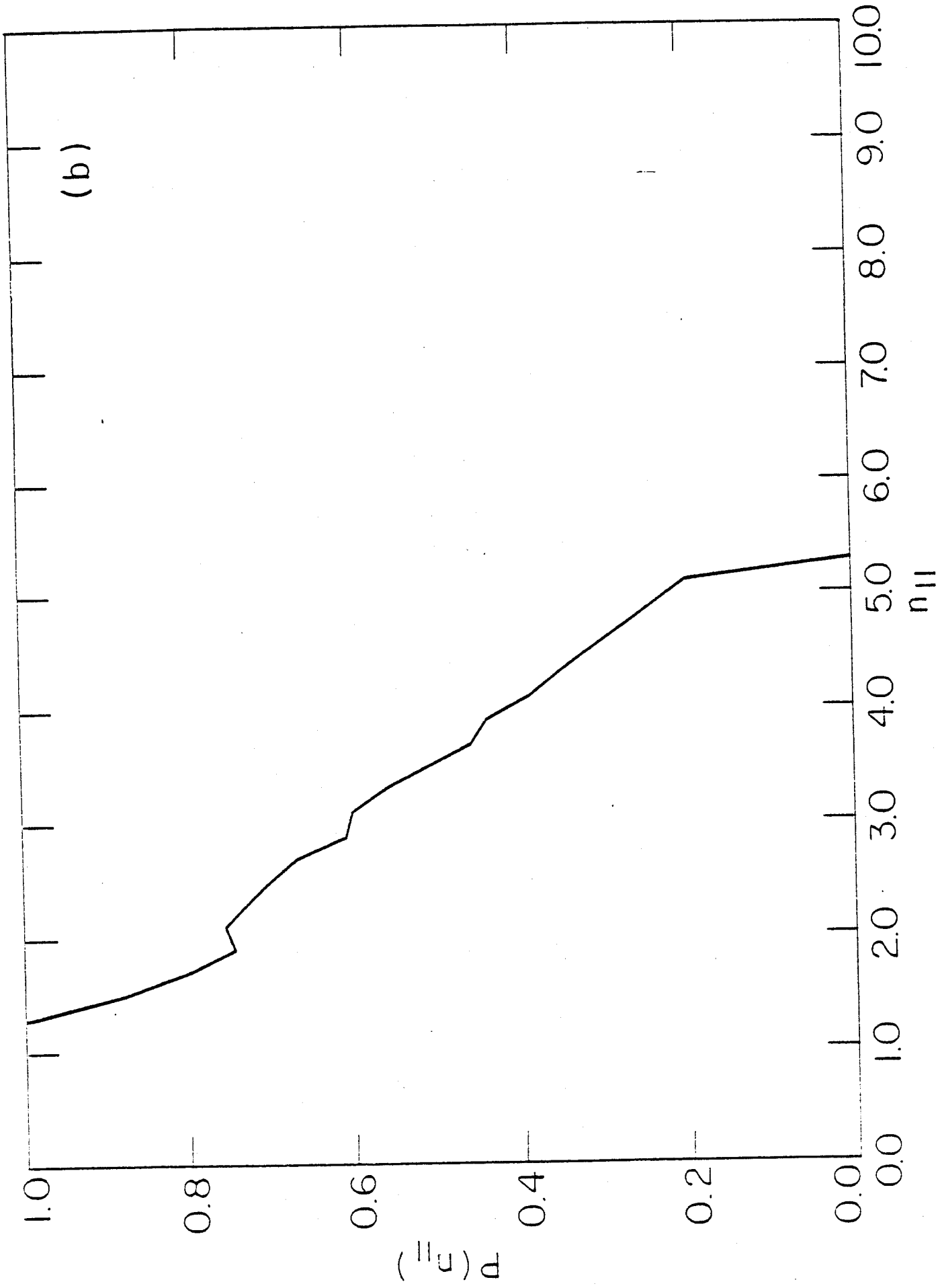

Fig. 7

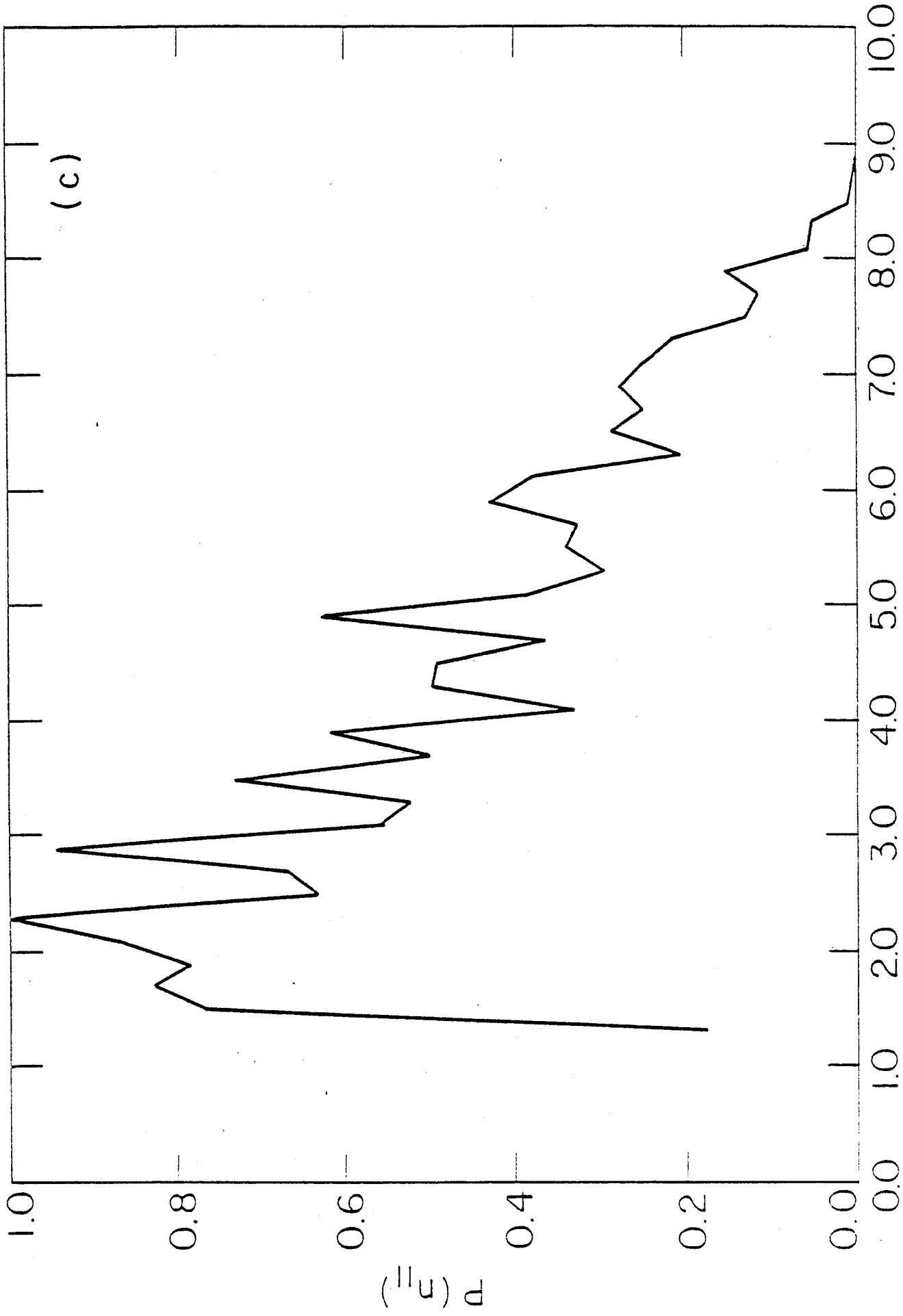

Fig. 7

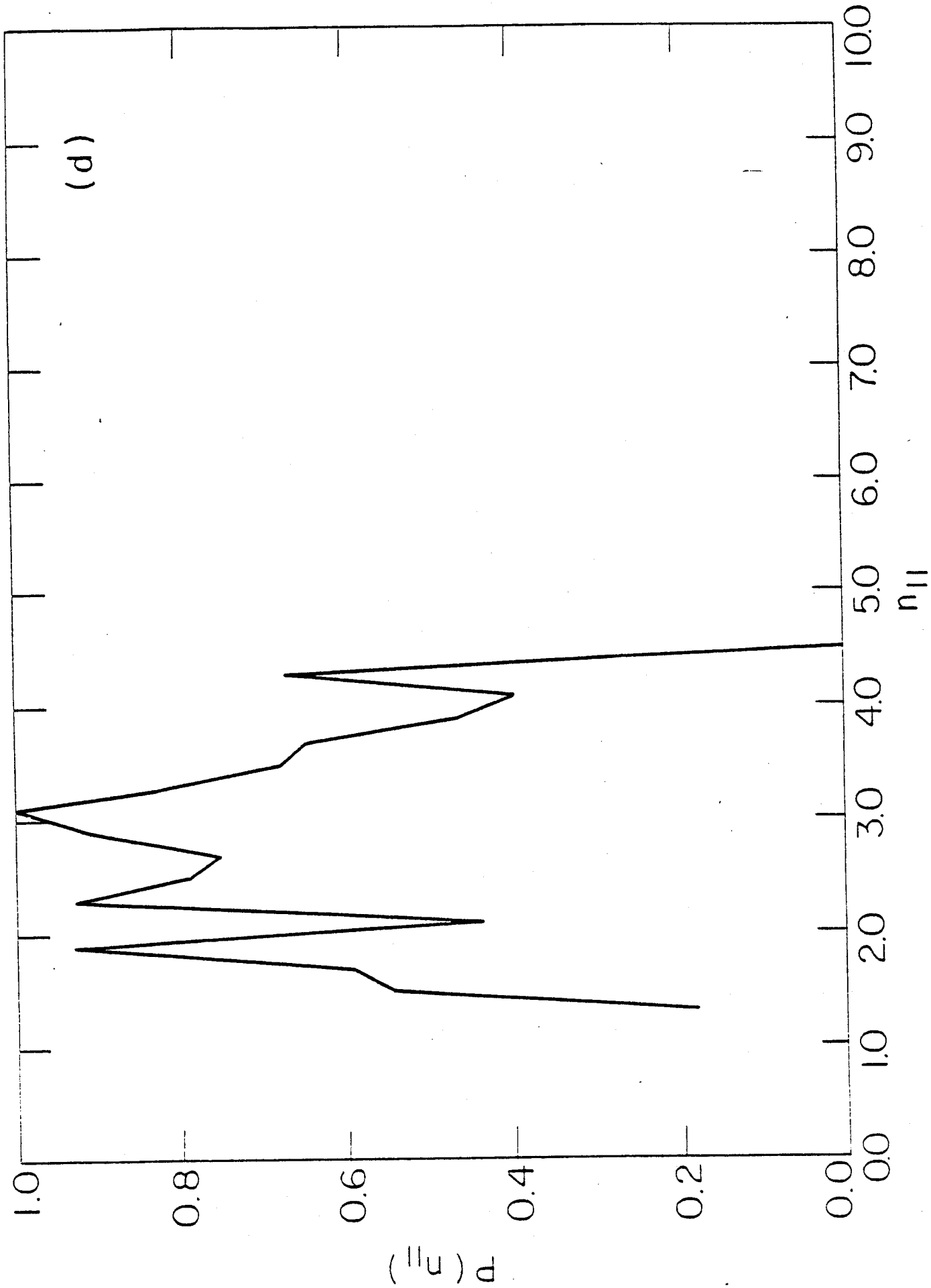

Fig. 7

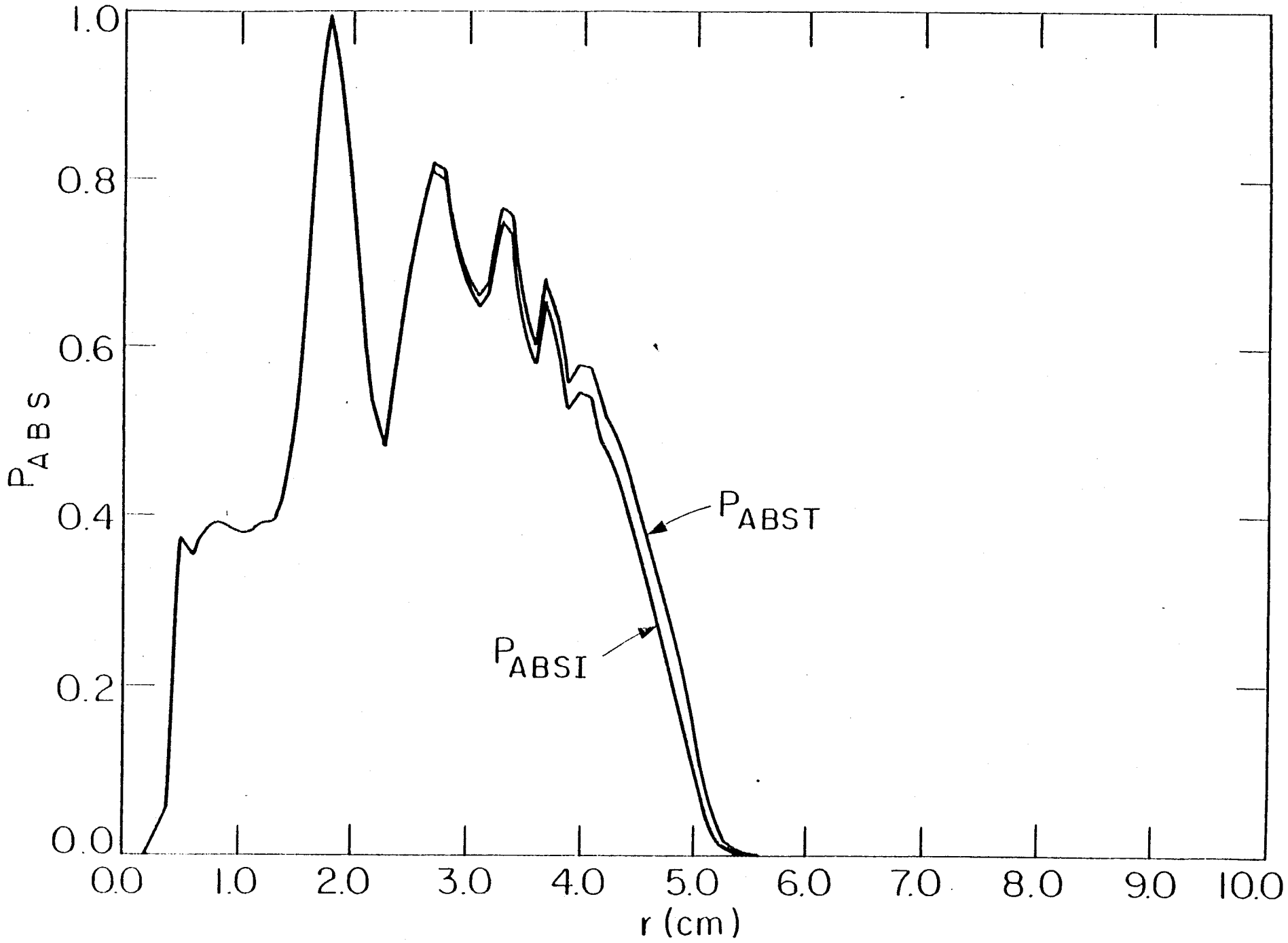
1.0
0.8
0.6
0.4
0.2
0.0
P_{ABS}
P_{ABST}
P_{ABSI}
0.0
1.0
2.0
3.0
4.0
5.0
6.0
7.0
8.0
9.0
10.0
r (cm)

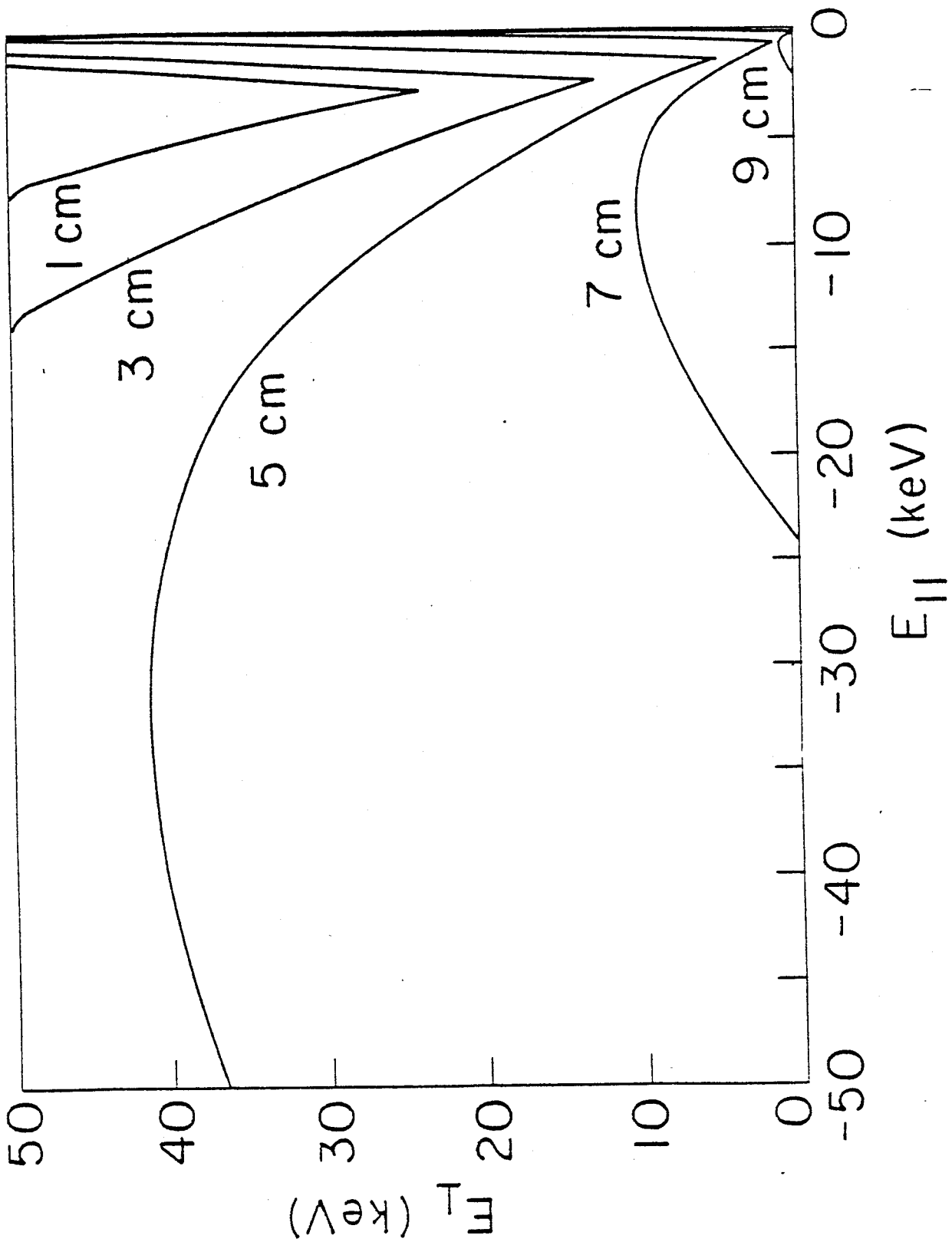

Fig. 9

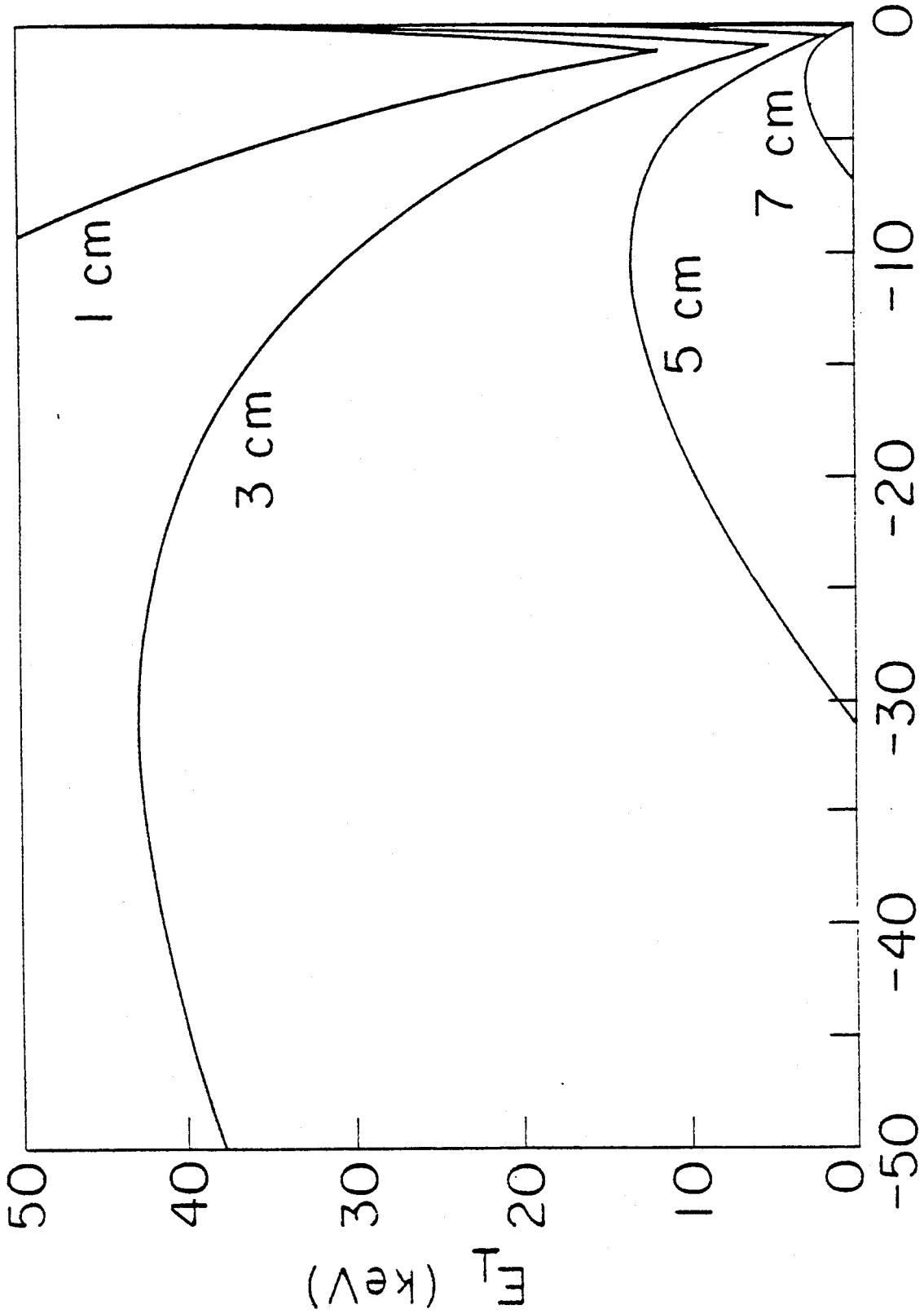

Fig. 10

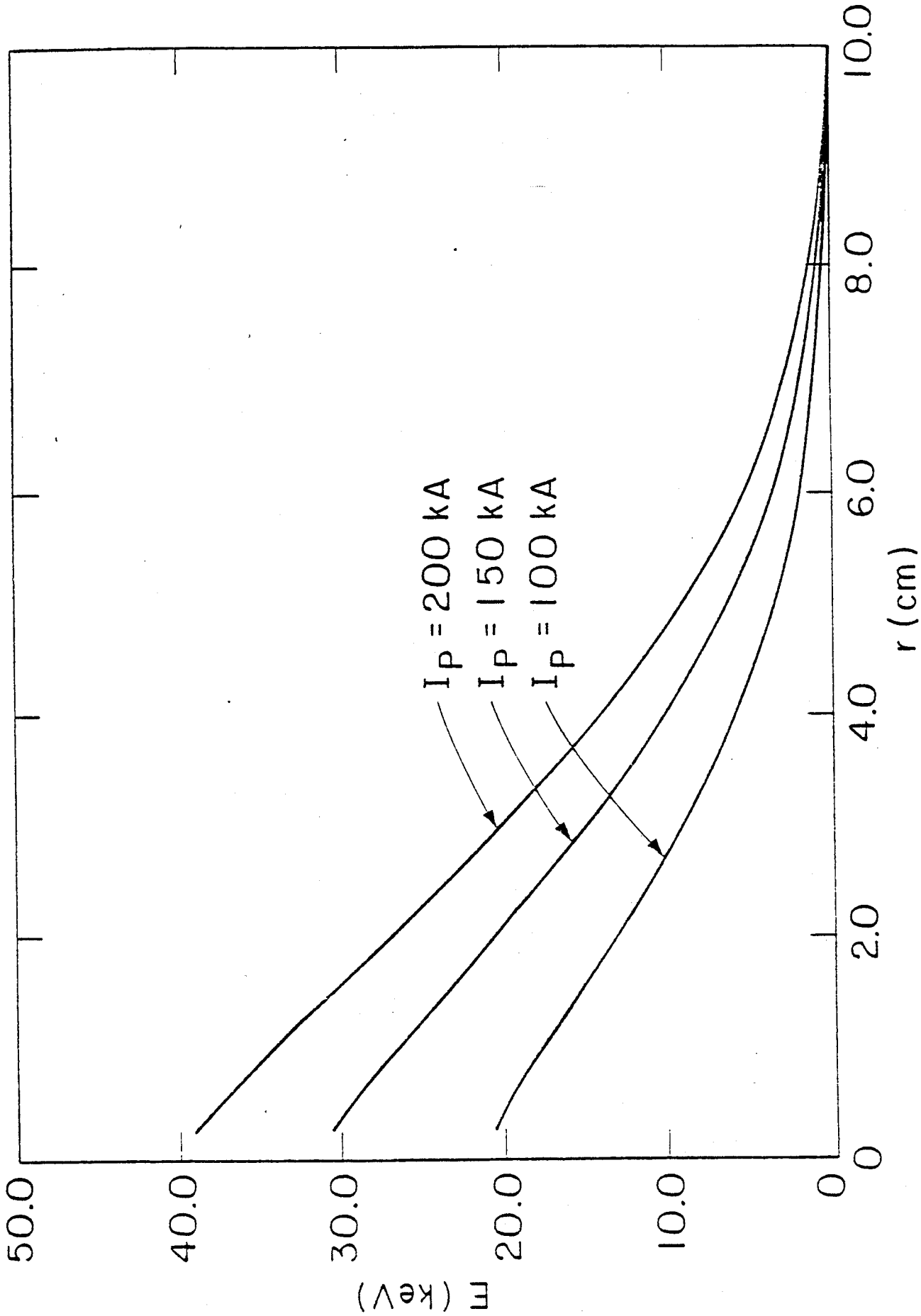
E (keV)
50.0
40.0
30.0
20.0
10.0
0
0
2.0
4.0
6.0
8.0
10.0
r (cm)
I_P = 200 kA
I_P = 150 kA
I_P = 100 kA

Fig. 11

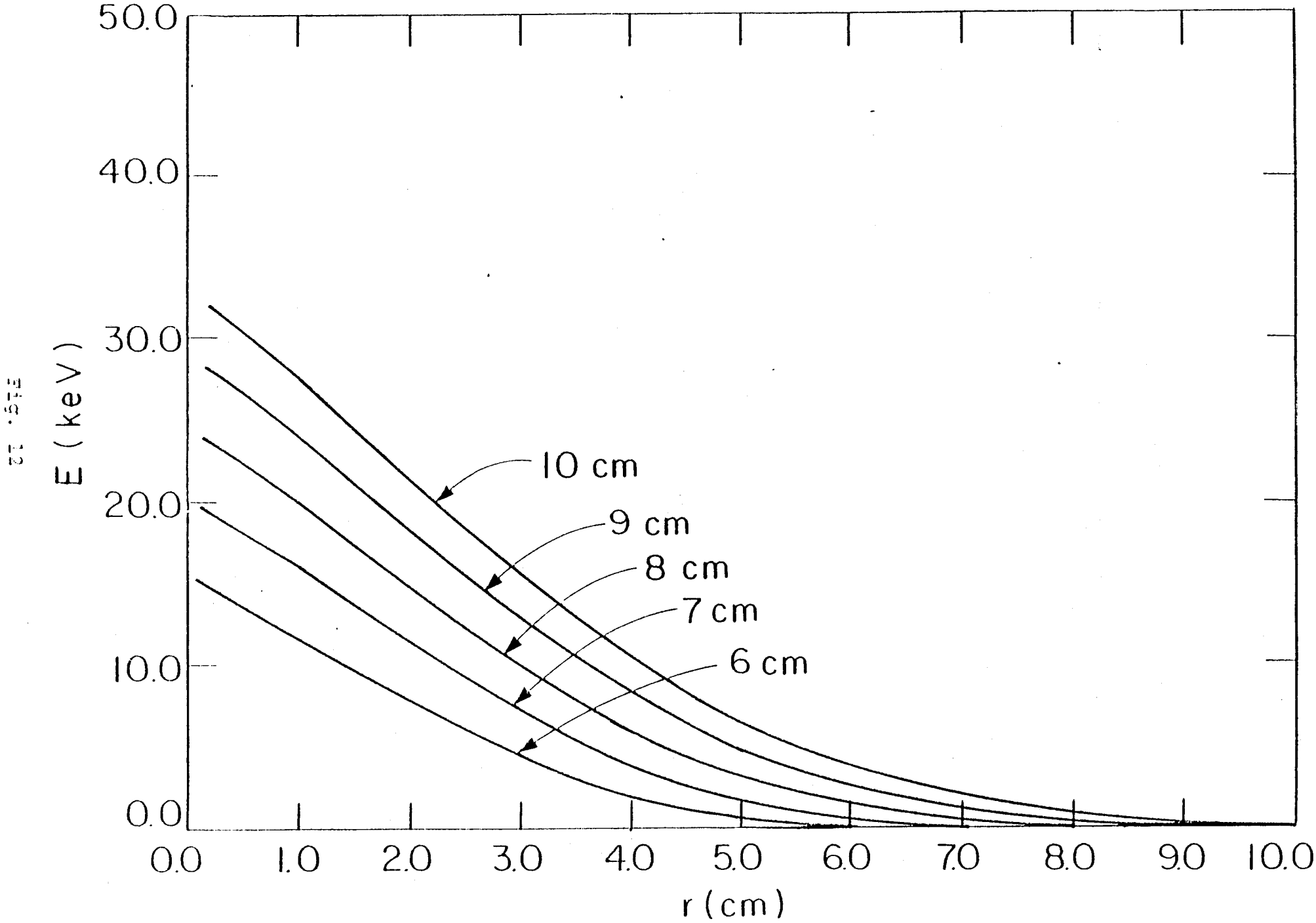
50.0
40.0
30.0
20.0
10.0
0.0
E (keV)
10 cm
9 cm
8 cm
7 cm
6 cm
0.0
1.0
2.0
3.0
4.0
5.0
6.0
7.0
8.0
9.0
10.0
r (cm)

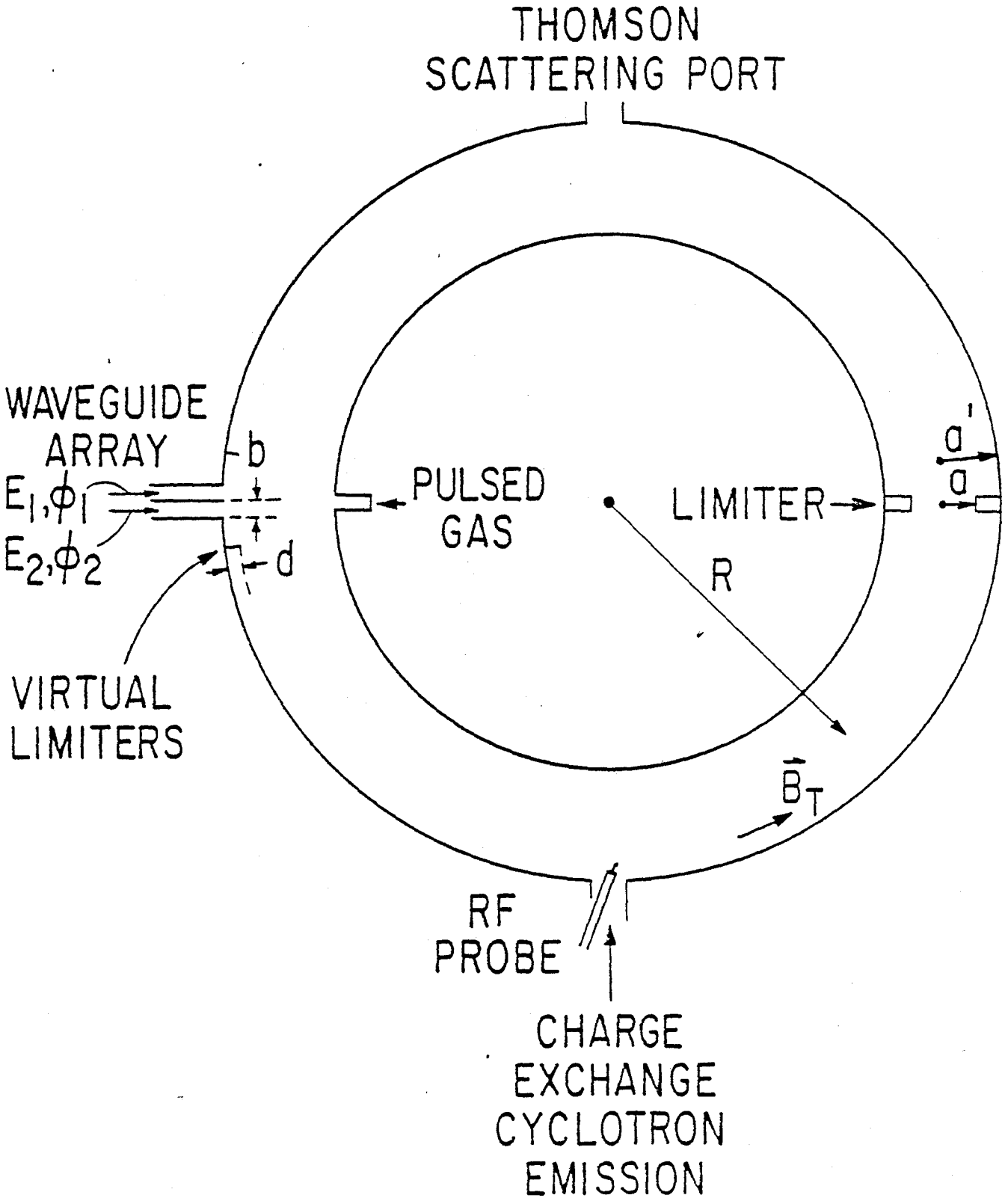
THOMSON
SCATTERING PORT
WAVEGUIDE
ARRAY
b
E_1, ϕ_1
E_2, ϕ_2
d
VIRTUAL
LIMITERS
PULSED
GAS
LIMITER
a'
a
R
$\vec{B}_T$
RF
PROBE
CHARGE
EXCHANGE
CYCLOTRON
EMISSION

Fig. 13

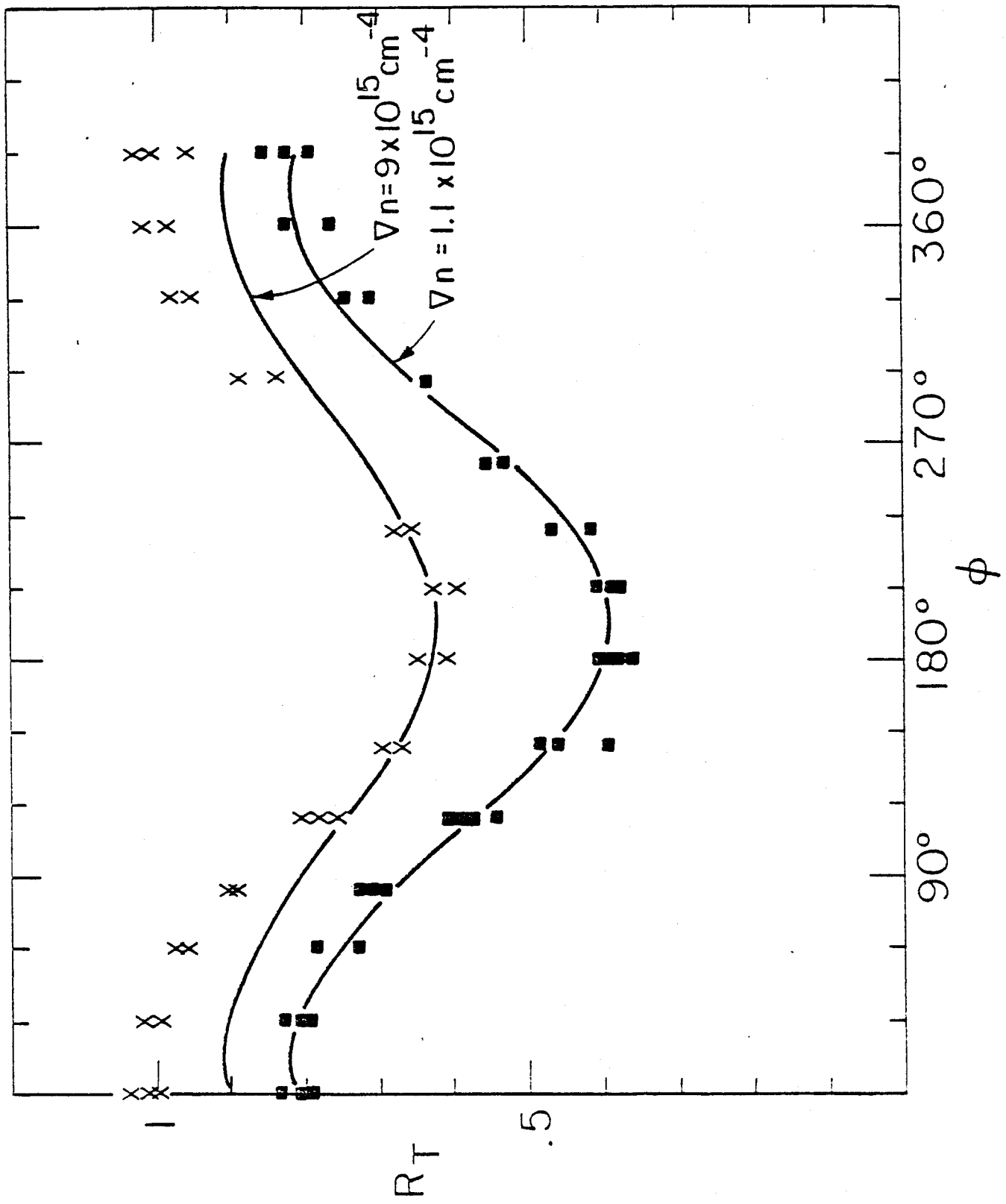
$\nabla n = 9 \times 10^{15}\ cm^{-4}$
$\nabla n = 1.1 \times 10^{15}\ cm^{-4}$
1
.5
R_T
90°
180°
270°
360°
ϕ

Fig. 11

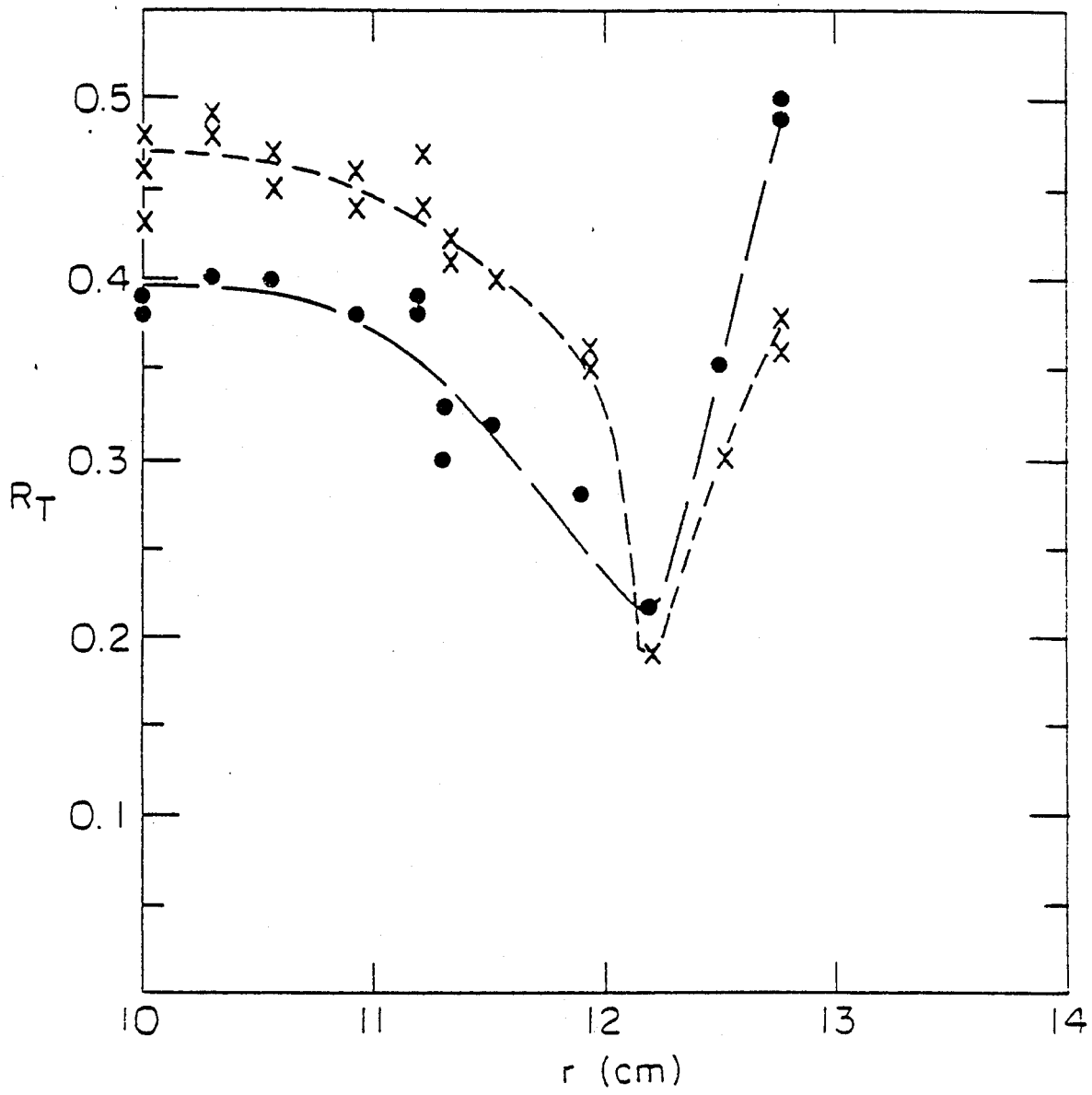

Fig. 13

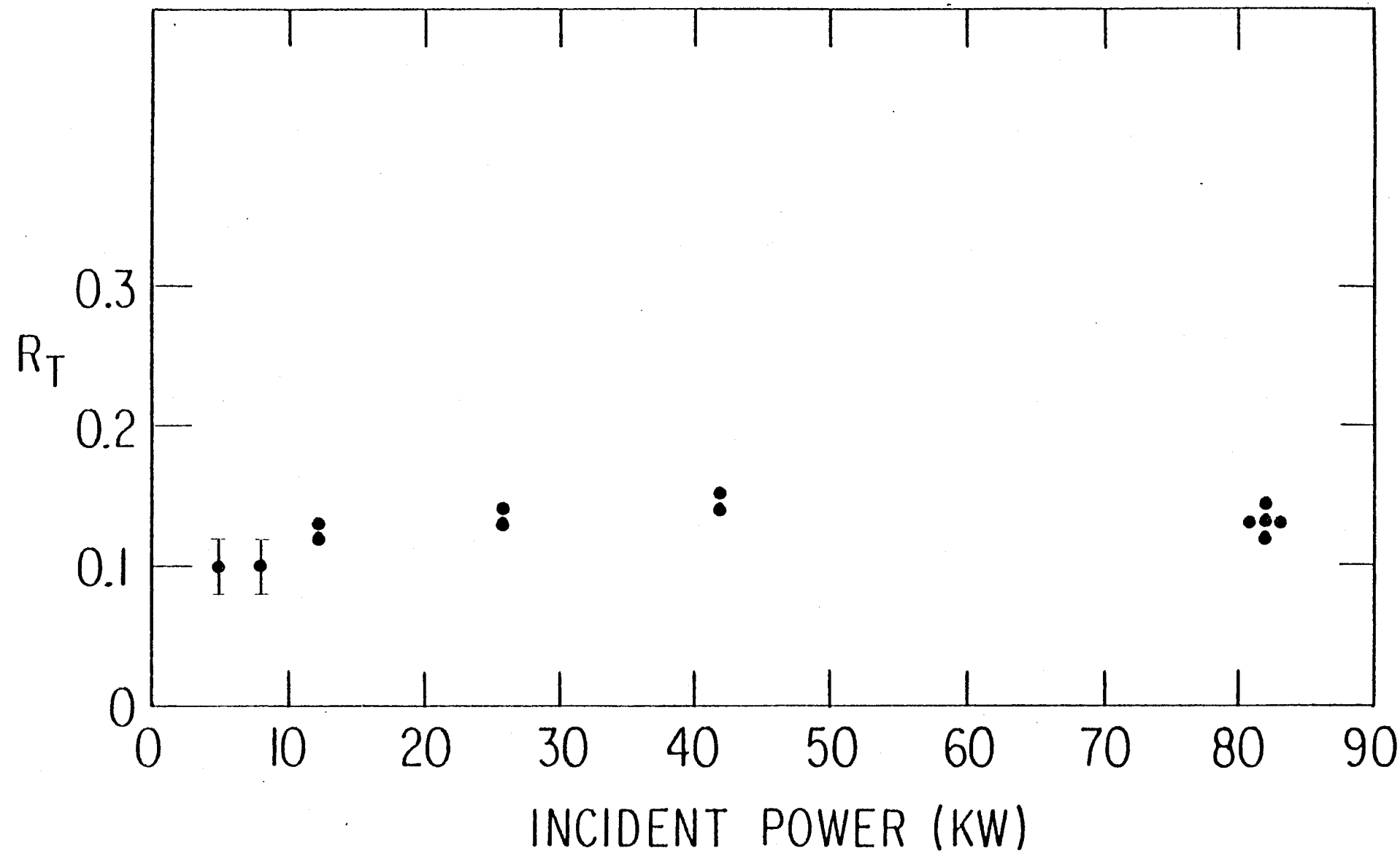

FIG. 16

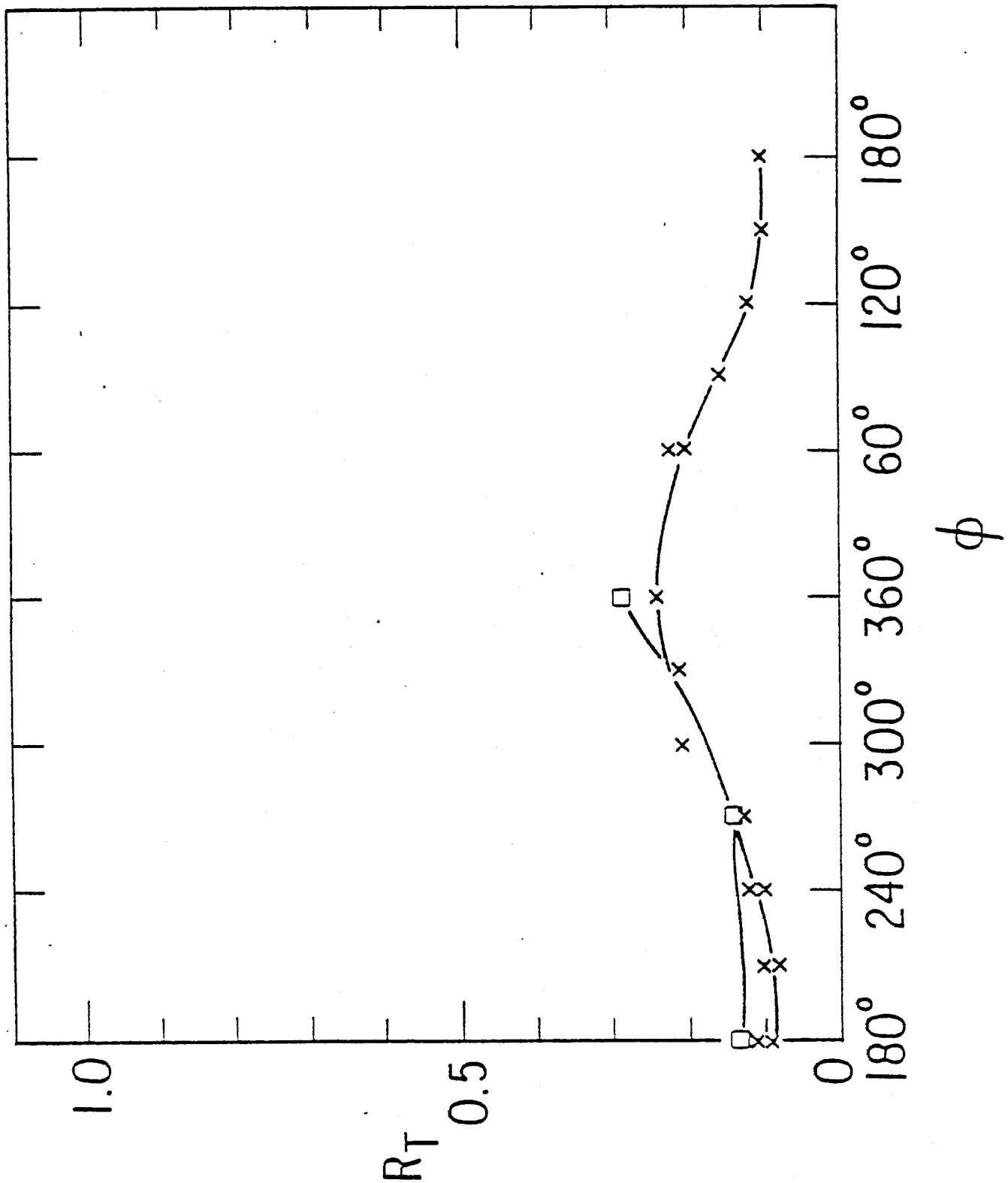

Fig. 17

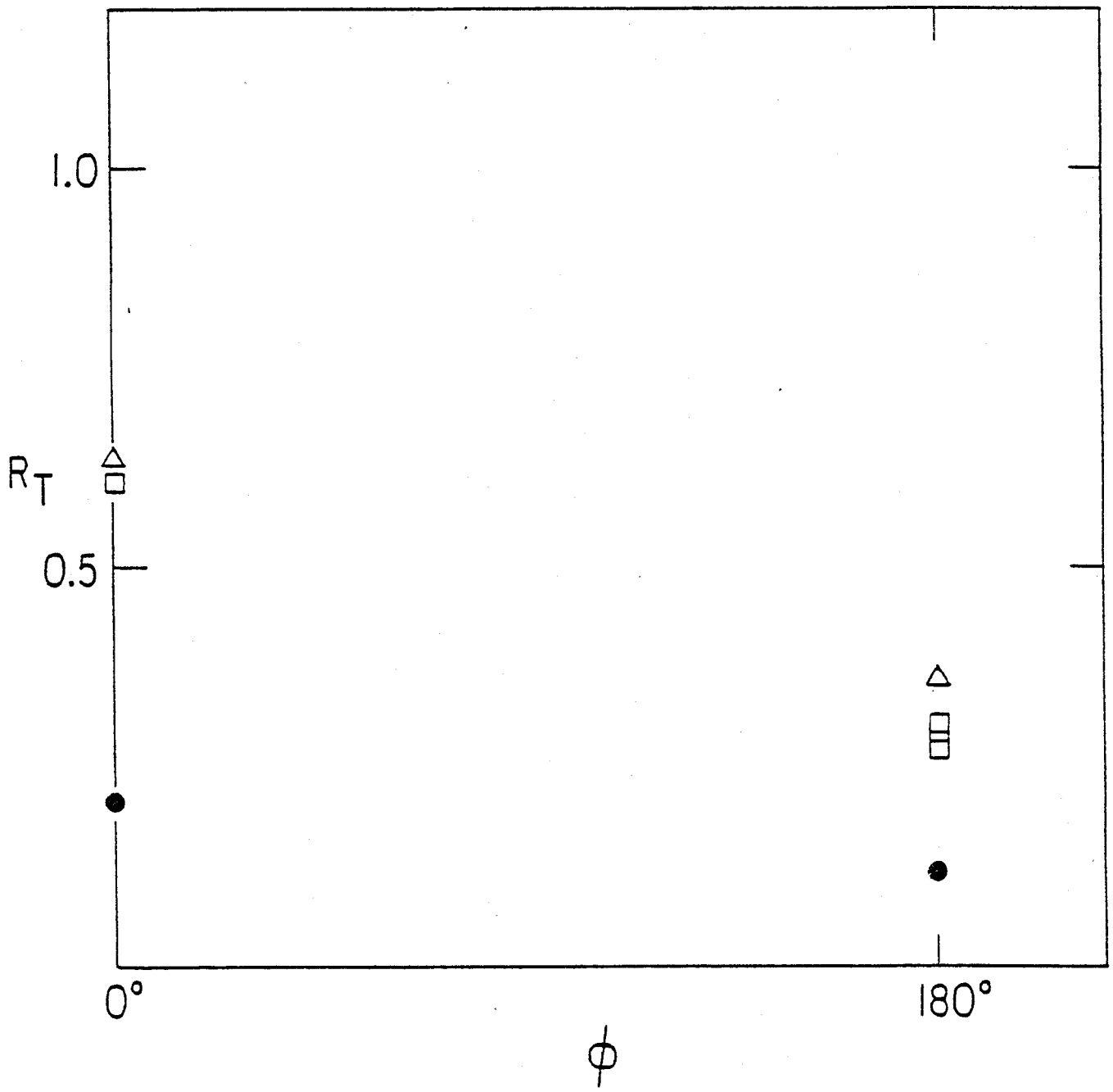

Fig. 18

FIG. 19

BALANCE VS. RF POWER

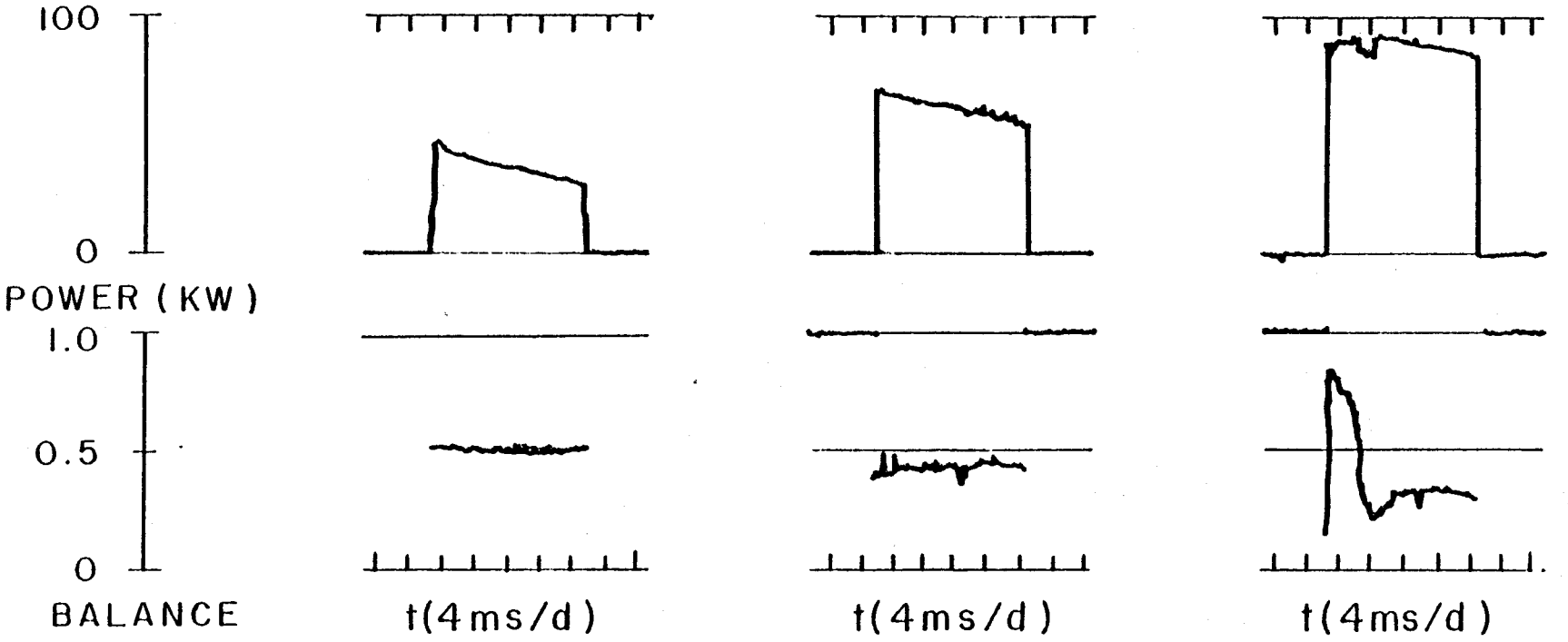

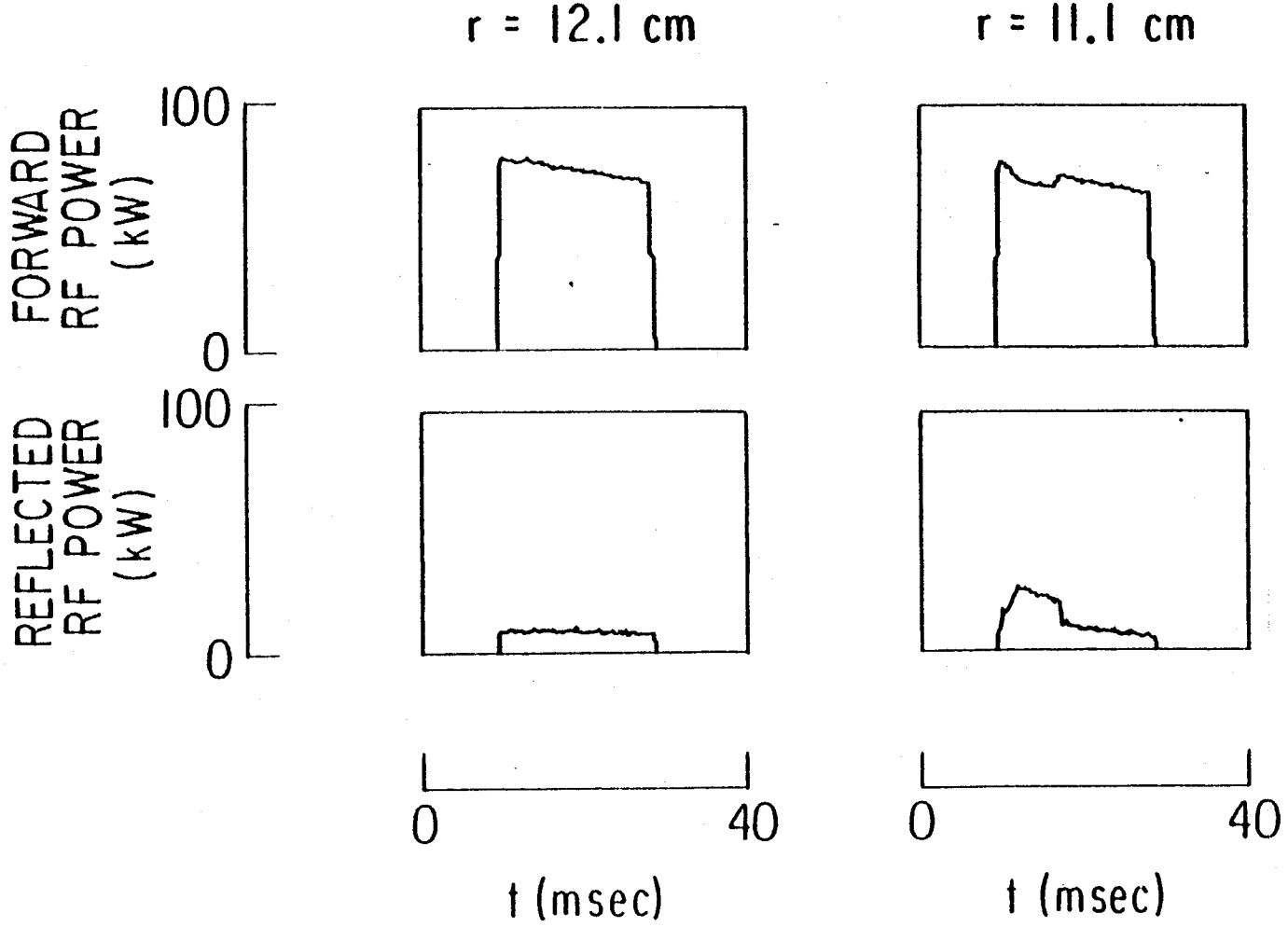
r = 12.1 cm
r = 11.1 cm
FORWARD RF POWER (kW)
100
0
REFLECTED RF POWER (kW)
100
0
0
40
t (msec)
0
40
t (msec)

Fig. 20

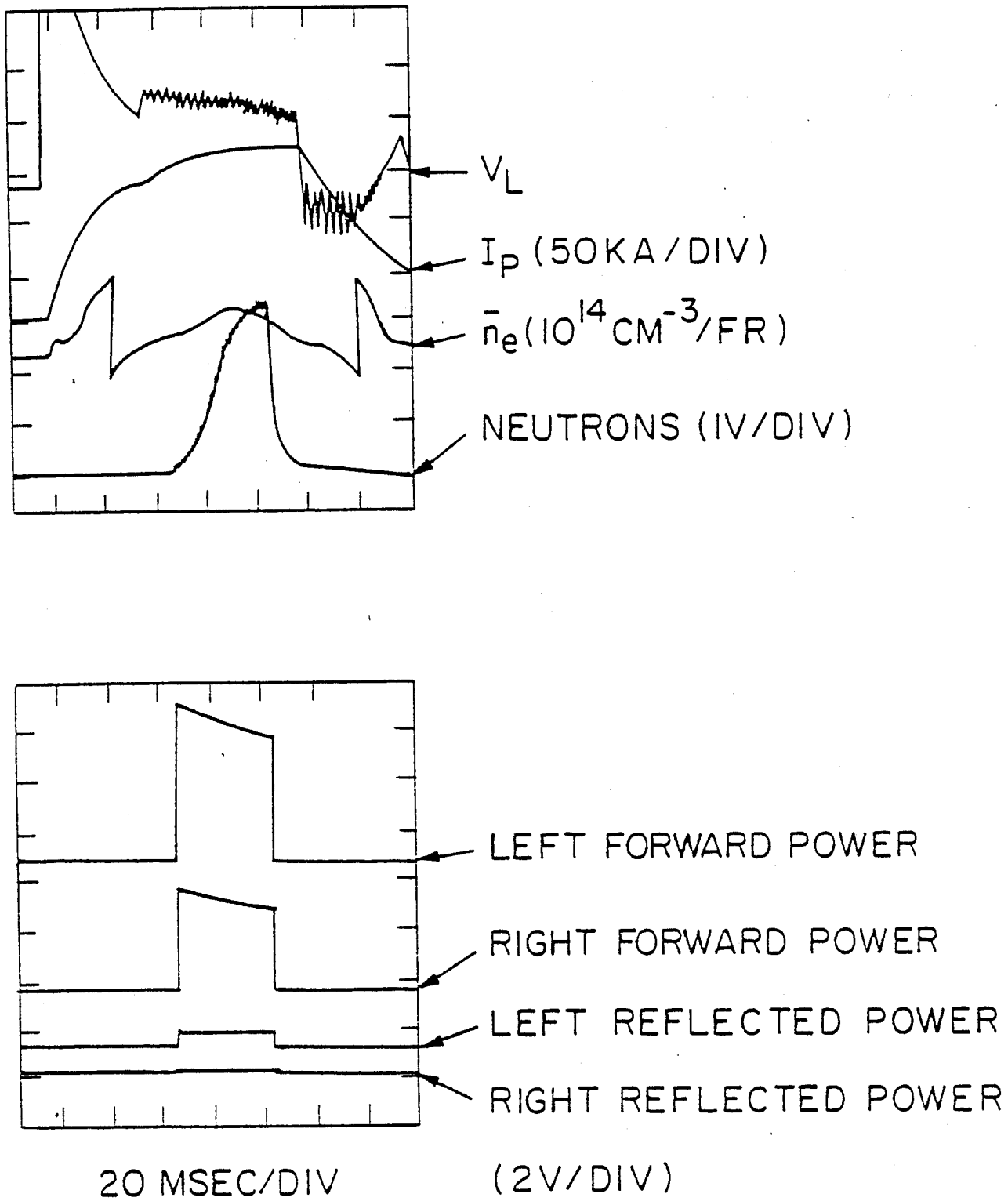
V_L
I_P (50KA/DIV)
$\bar{n}_e(10^{14}CM^{-3}/FR)$
NEUTRONS (IV/DIV)
LEFT FORWARD POWER
RIGHT FORWARD POWER
LEFT REFLECTED POWER
RIGHT REFLECTED POWER
20 MSEC/DIV
(2V/DIV)

Fig. 21

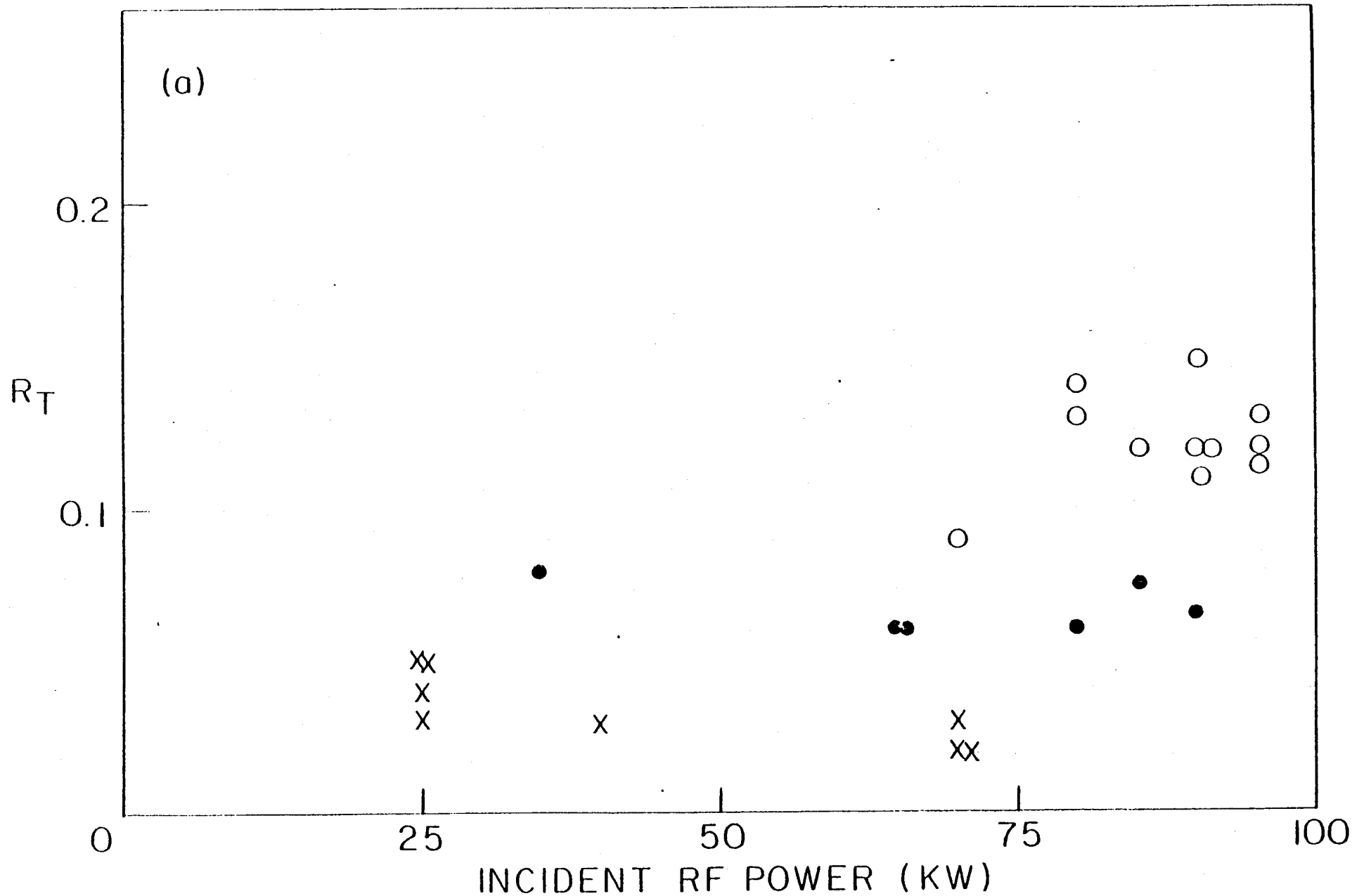

Fig. 22

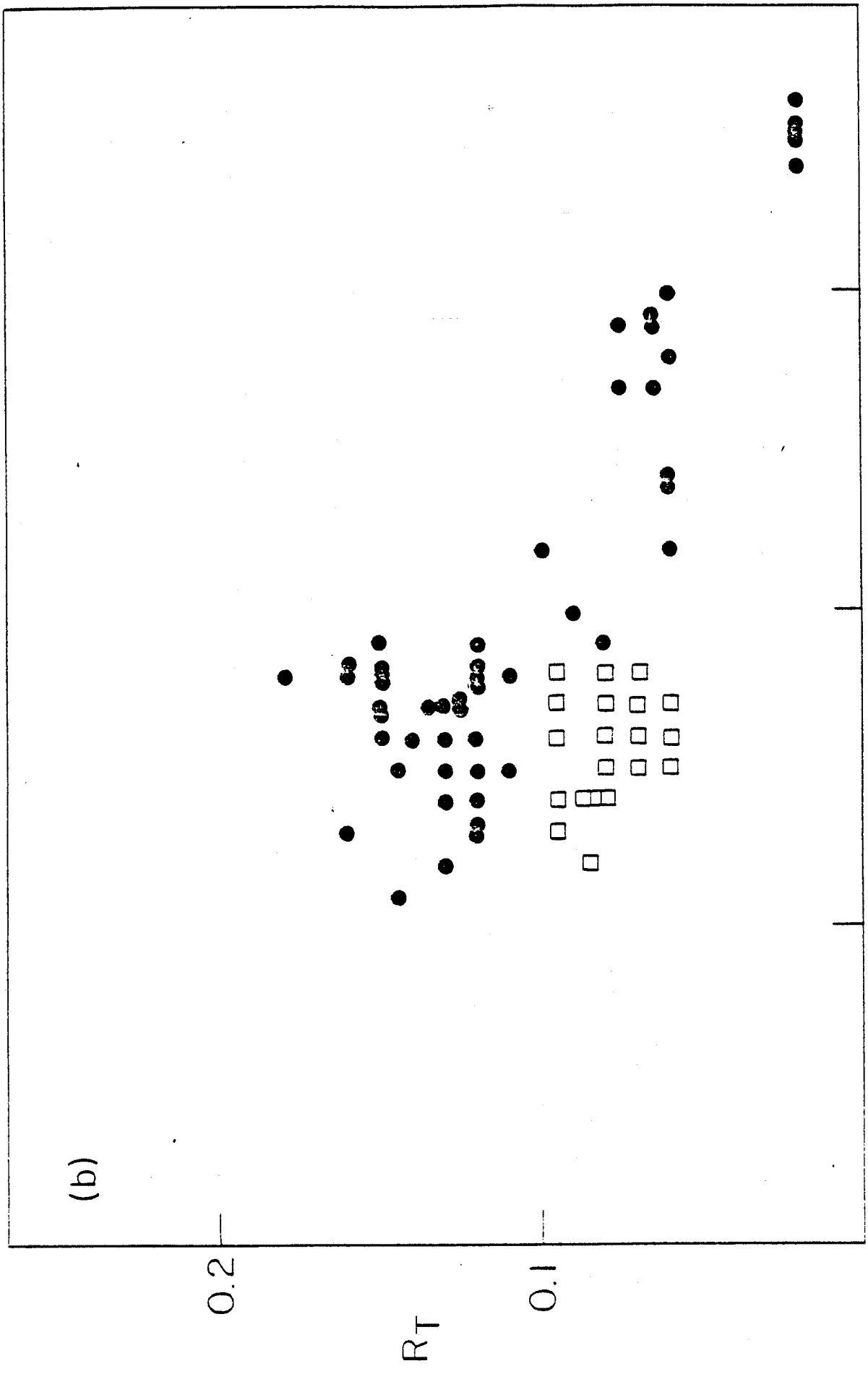

Fig. 22

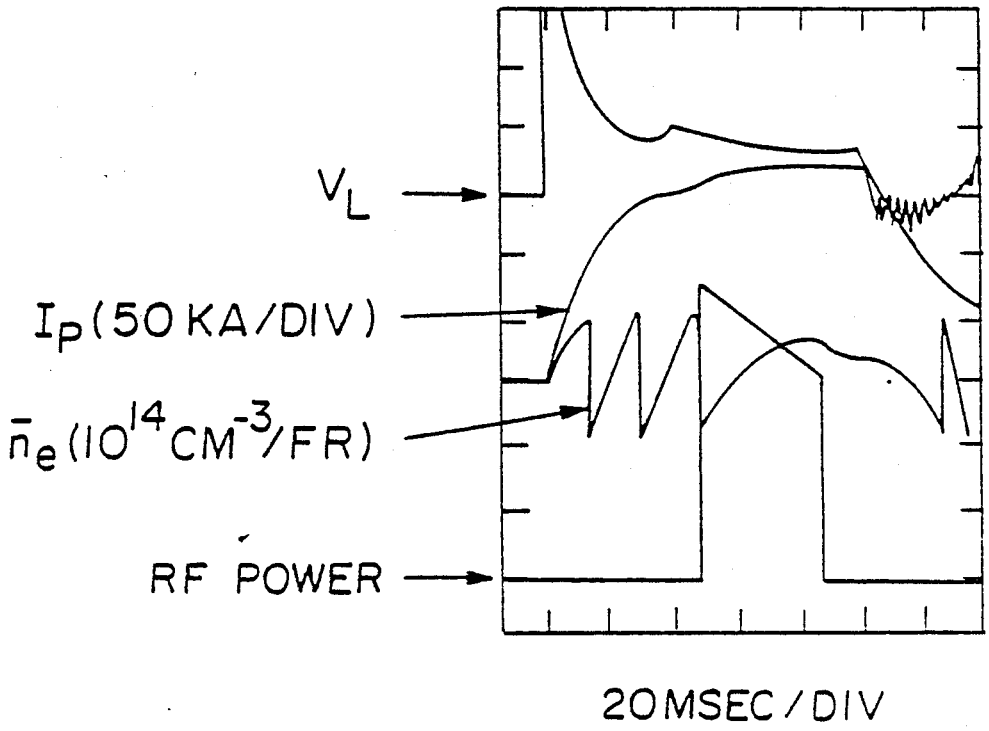

Fig. 23

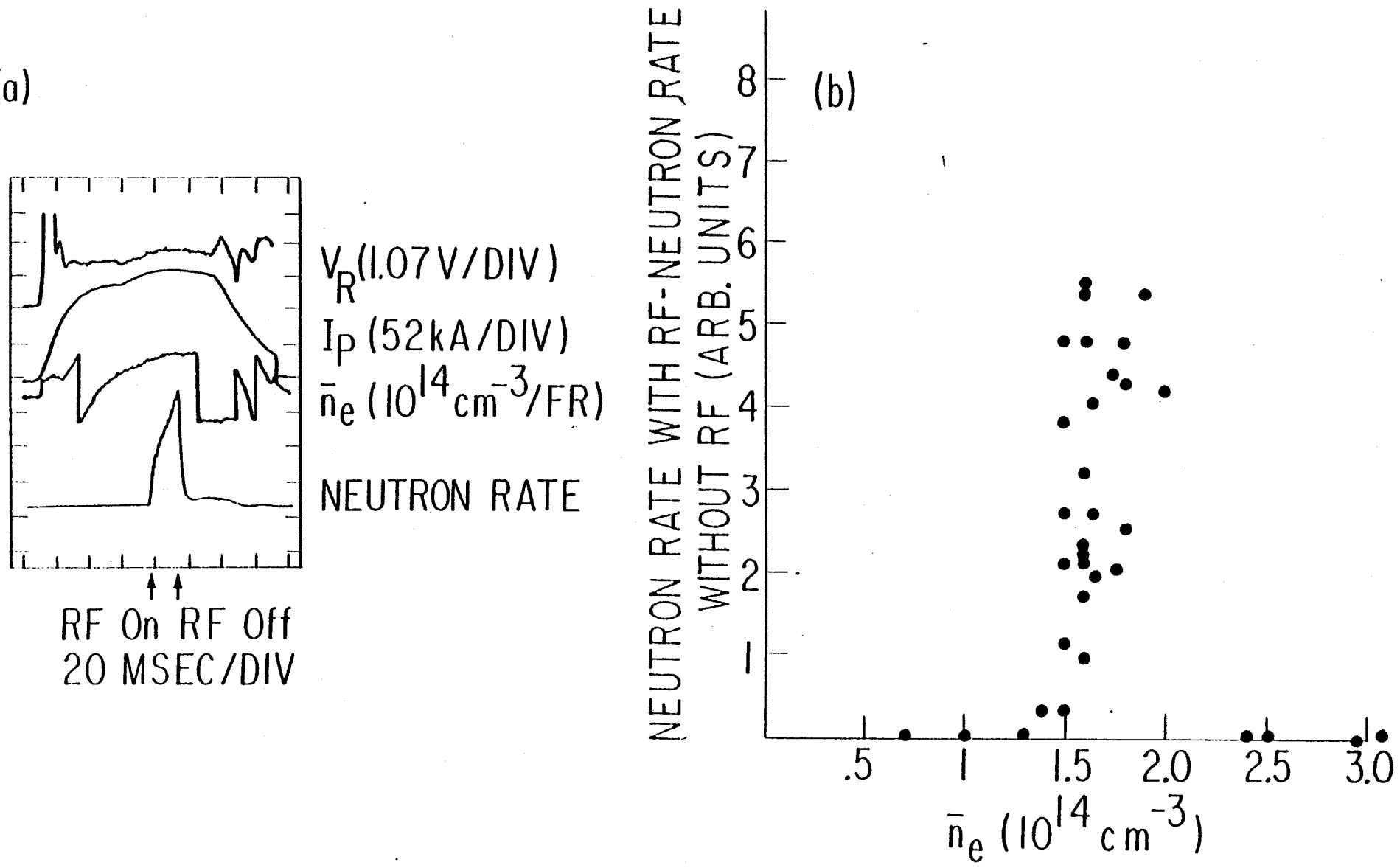
(a)
V_R(1.07V/DIV)
I_P (52kA/DIV)
$\bar{n}_e$ (10^{14}cm^{-3}/FR)
NEUTRON RATE
RF On RF Off
20 MSEC/DIV
(b)
NEUTRON RATE WITH RF-NEUTRON RATE
WITHOUT RF (ARB. UNITS)
1
2
3
4
5
6
7
8
.5
1
1.5
2.0
2.5
3.0
$\bar{n}_e$ (10^{14} cm^{-3})

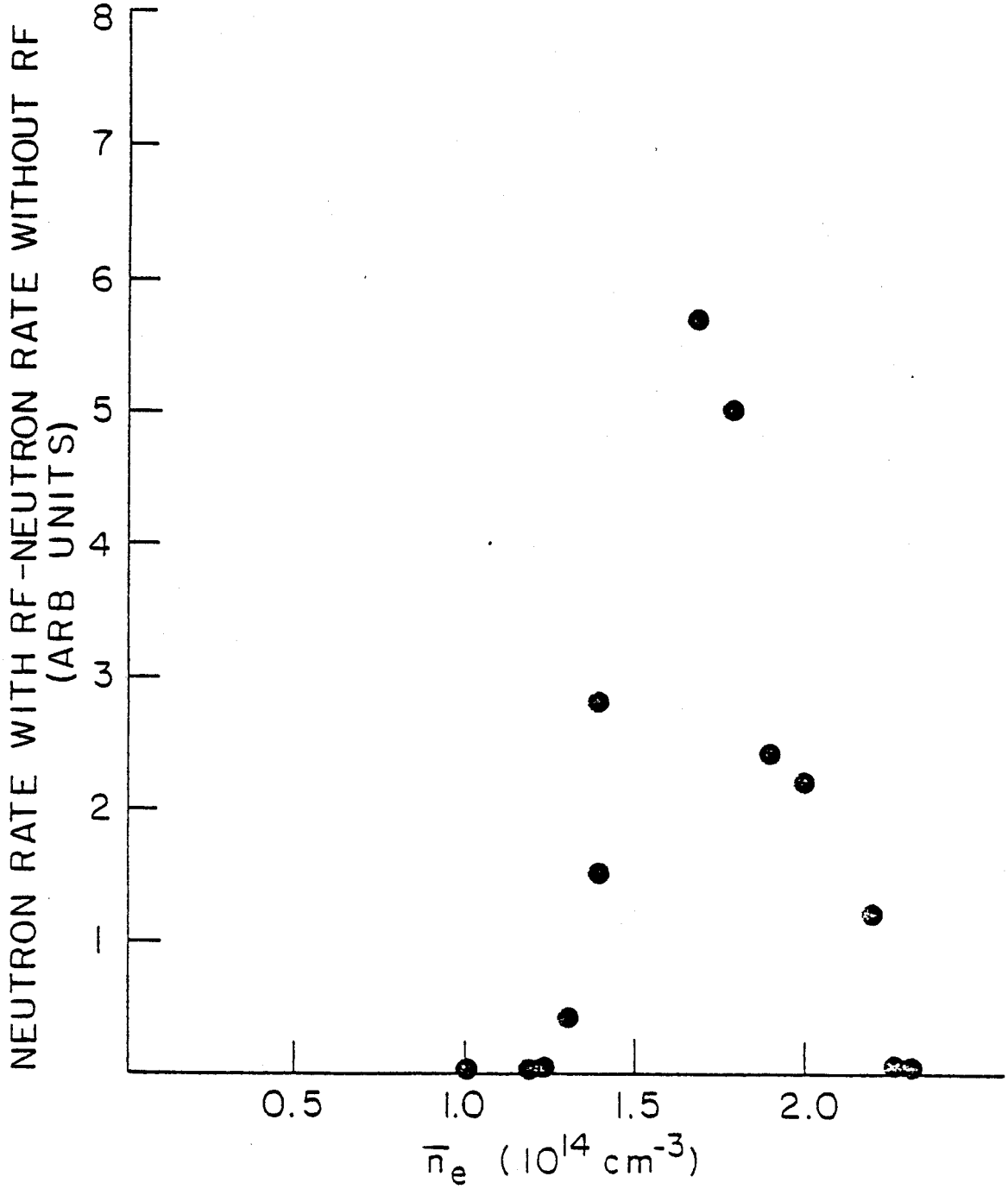
NEUTRON RATE WITH RF-NEUTRON RATE WITHOUT RF
(ARB UNITS)
8
7
6
5
4
3
2
1
0.5
1.0
1.5
2.0
$\bar{n}_e$ (10^{14} cm^{-3})

Fig. 25

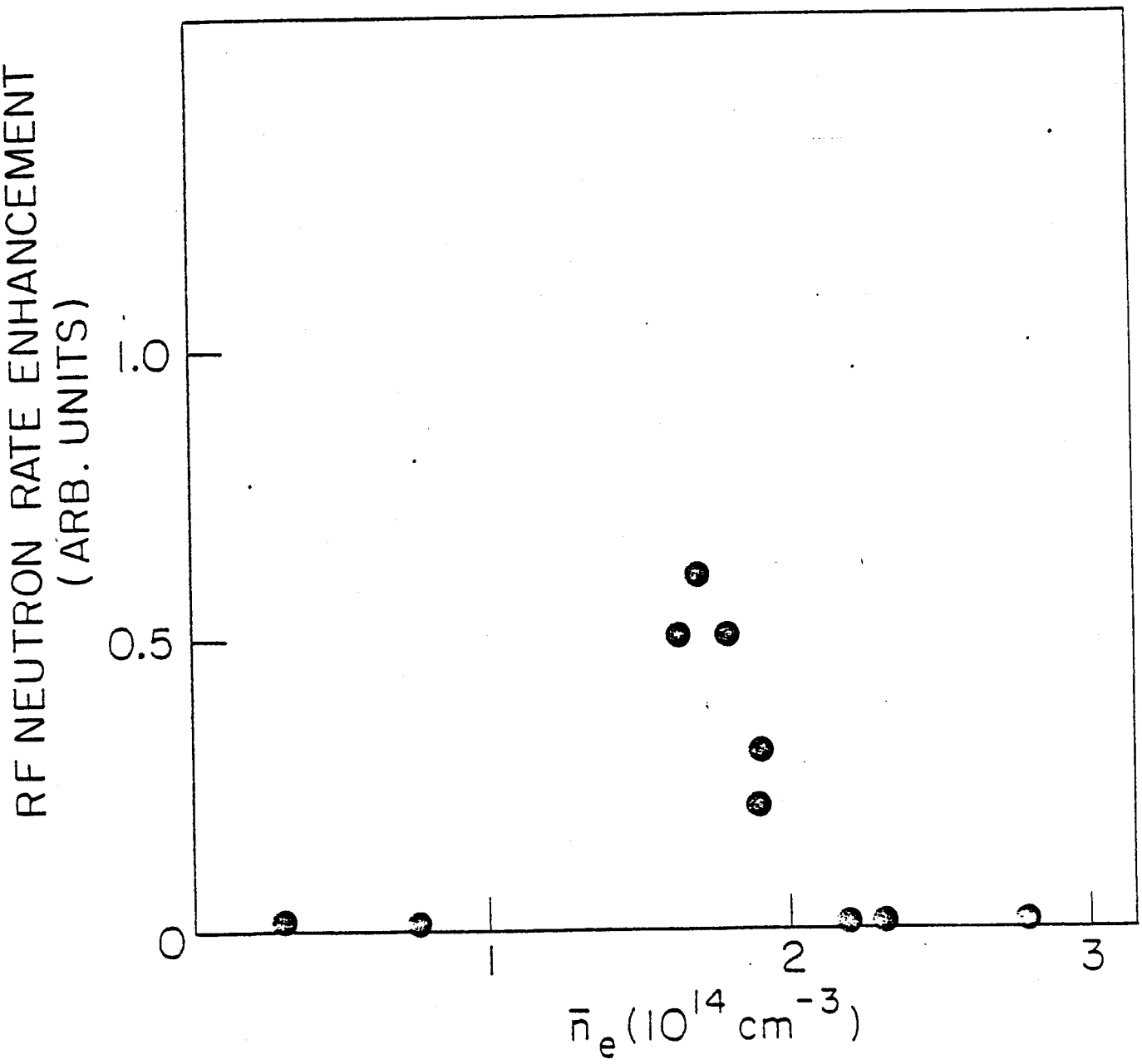
RF NEUTRON RATE ENHANCEMENT
(ARB. UNITS)
1.0
0.5
0
1
2
3
$\bar{n}_e(10^{14}\,cm^{-3})$

Fig. 26

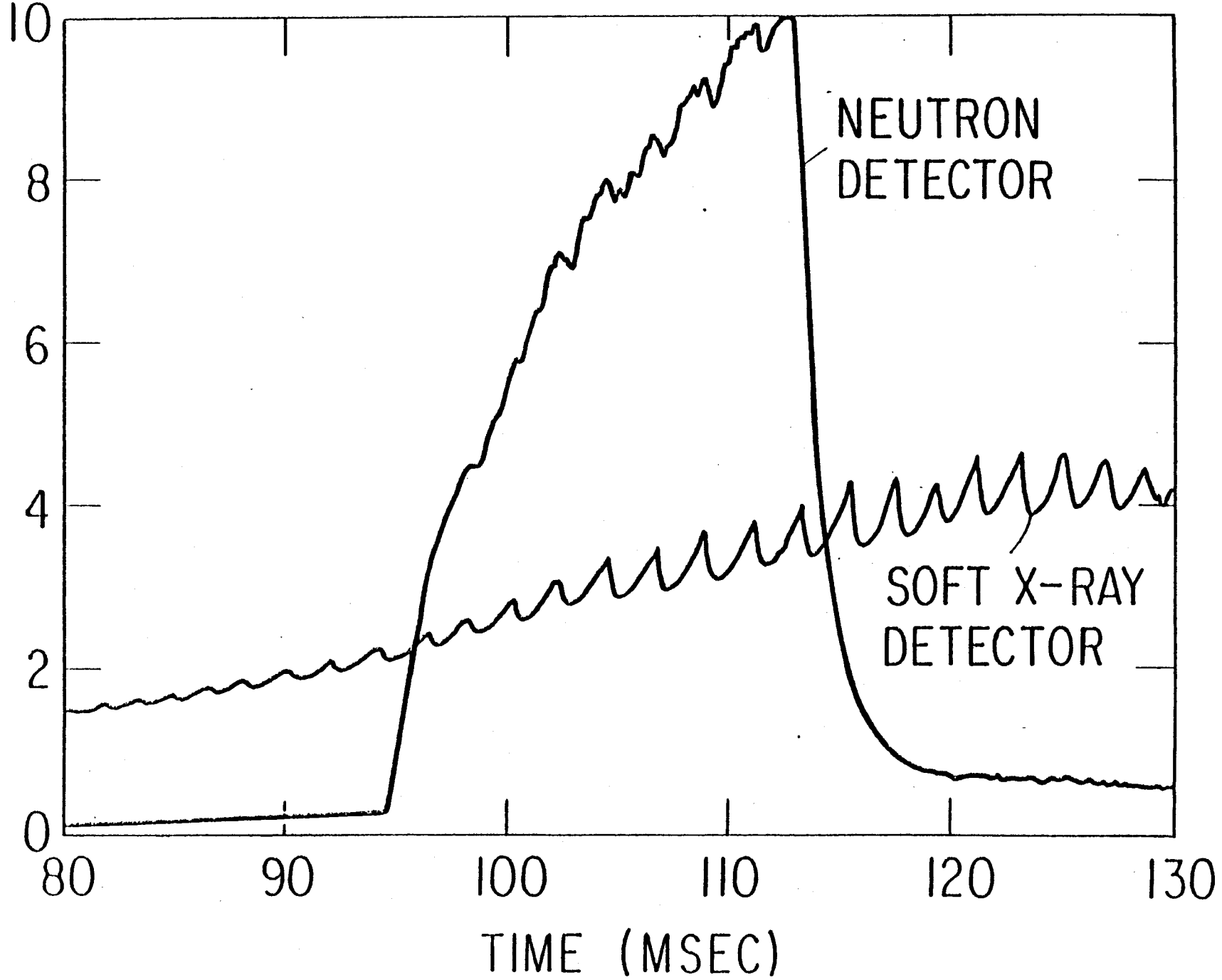
10
8
6
4
2
0
80
90
100
110
120
130
NEUTRON
DETECTOR
SOFT X-RAY
DETECTOR
TIME (MSEC)

Fig. 28

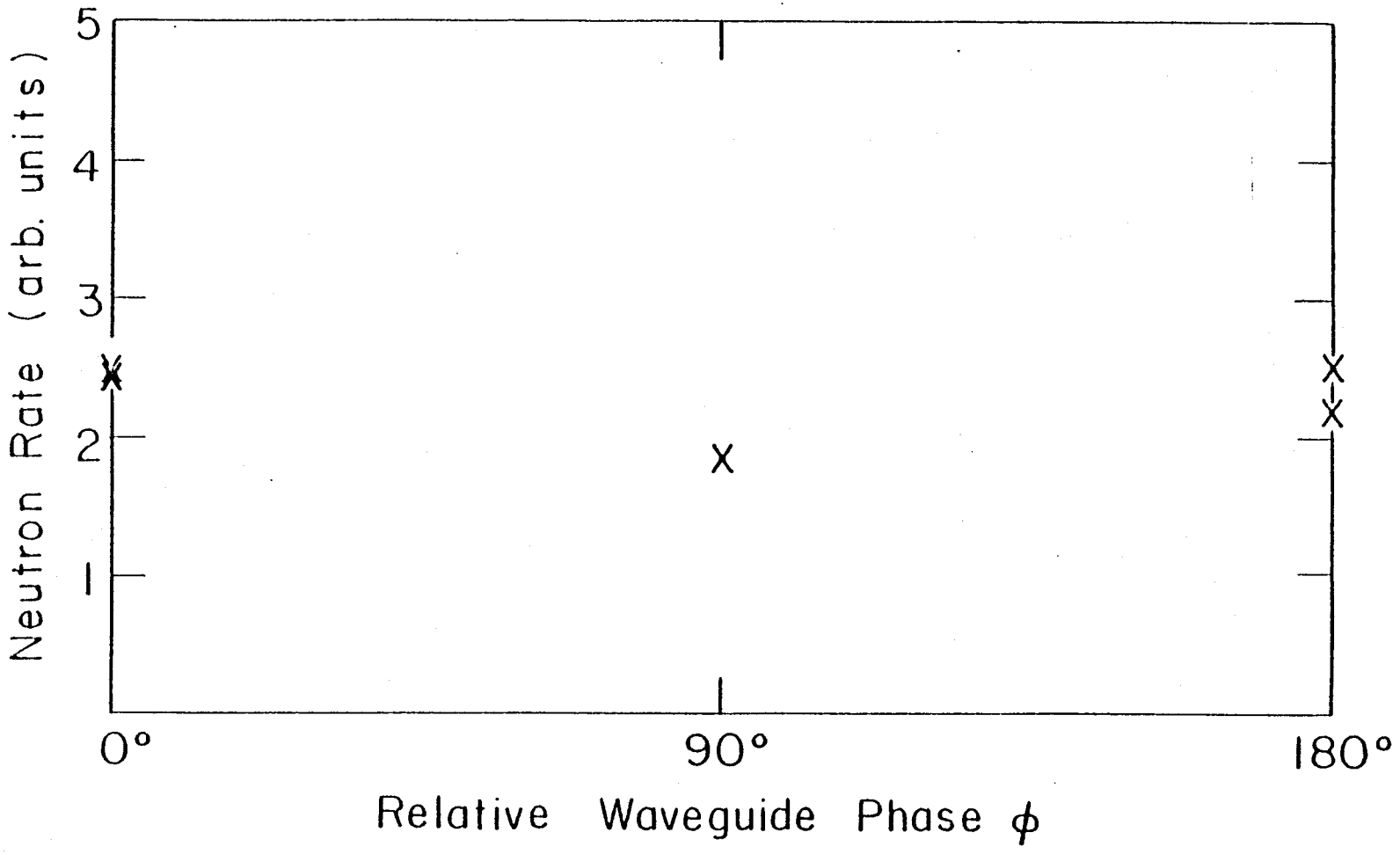
Neutron Rate (arb. units)
5
4
3
2
1
0°
90°
180°
Relative Waveguide Phase ϕ

Fig. 29

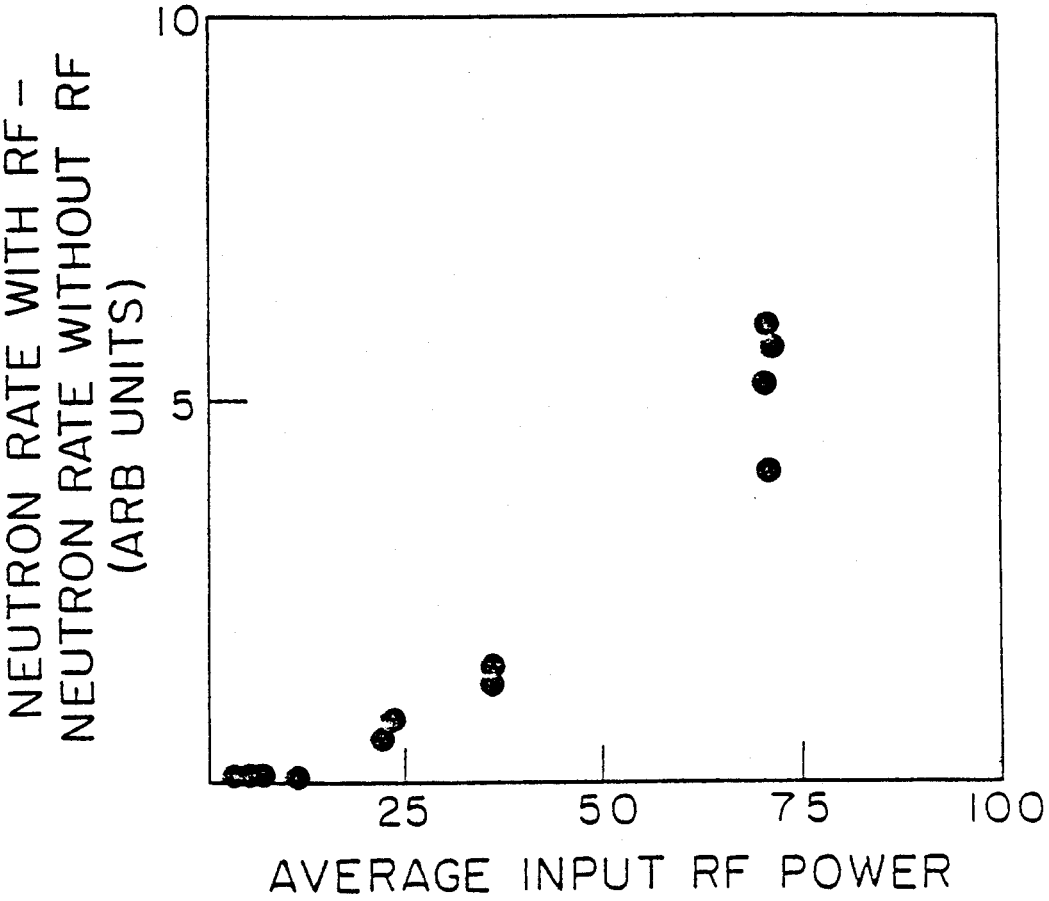
NEUTRON RATE WITH RF –
NEUTRON RATE WITHOUT RF
(ARB UNITS)
10
5
25
50
75
100
AVERAGE INPUT RF POWER

Fig. 30

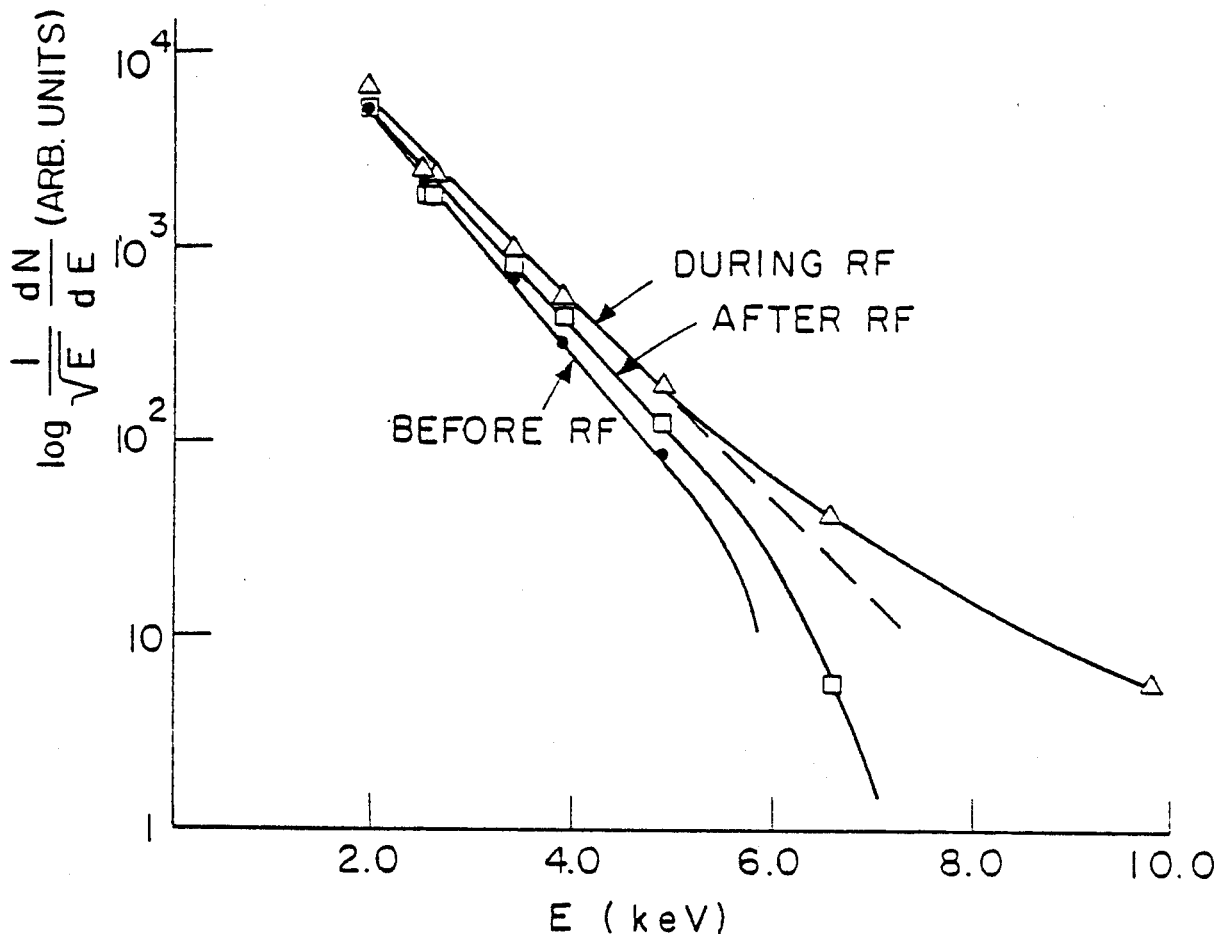
$\log \frac{1}{\sqrt{E}} \frac{dN}{dE}$ (ARB. UNITS)
10^4
10^3
10^2
10
1
DURING RF
AFTER RF
BEFORE RF
2.0
4.0
6.0
8.0
10.0
E (keV)

Fig. 31

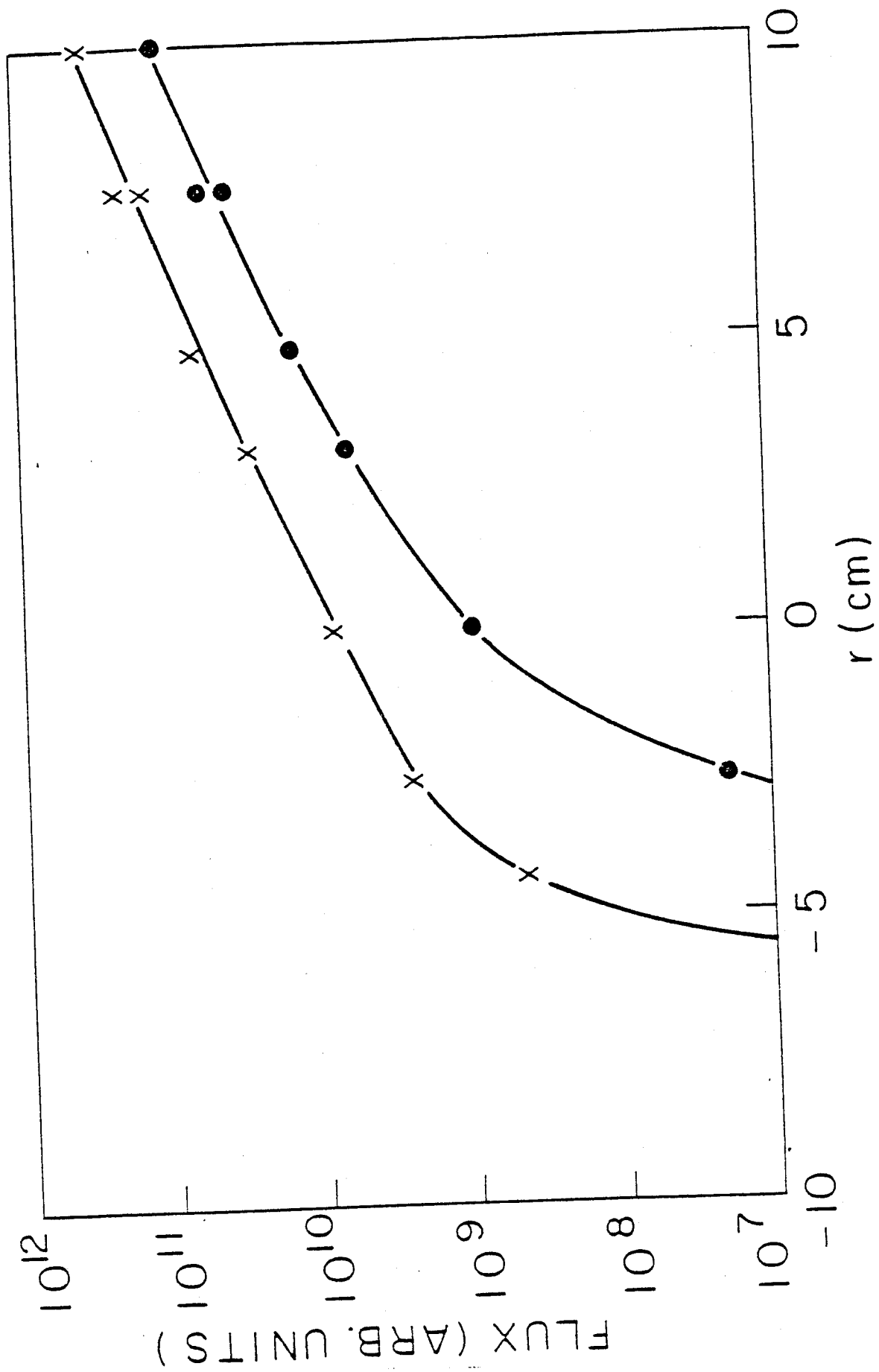

Fig. 32

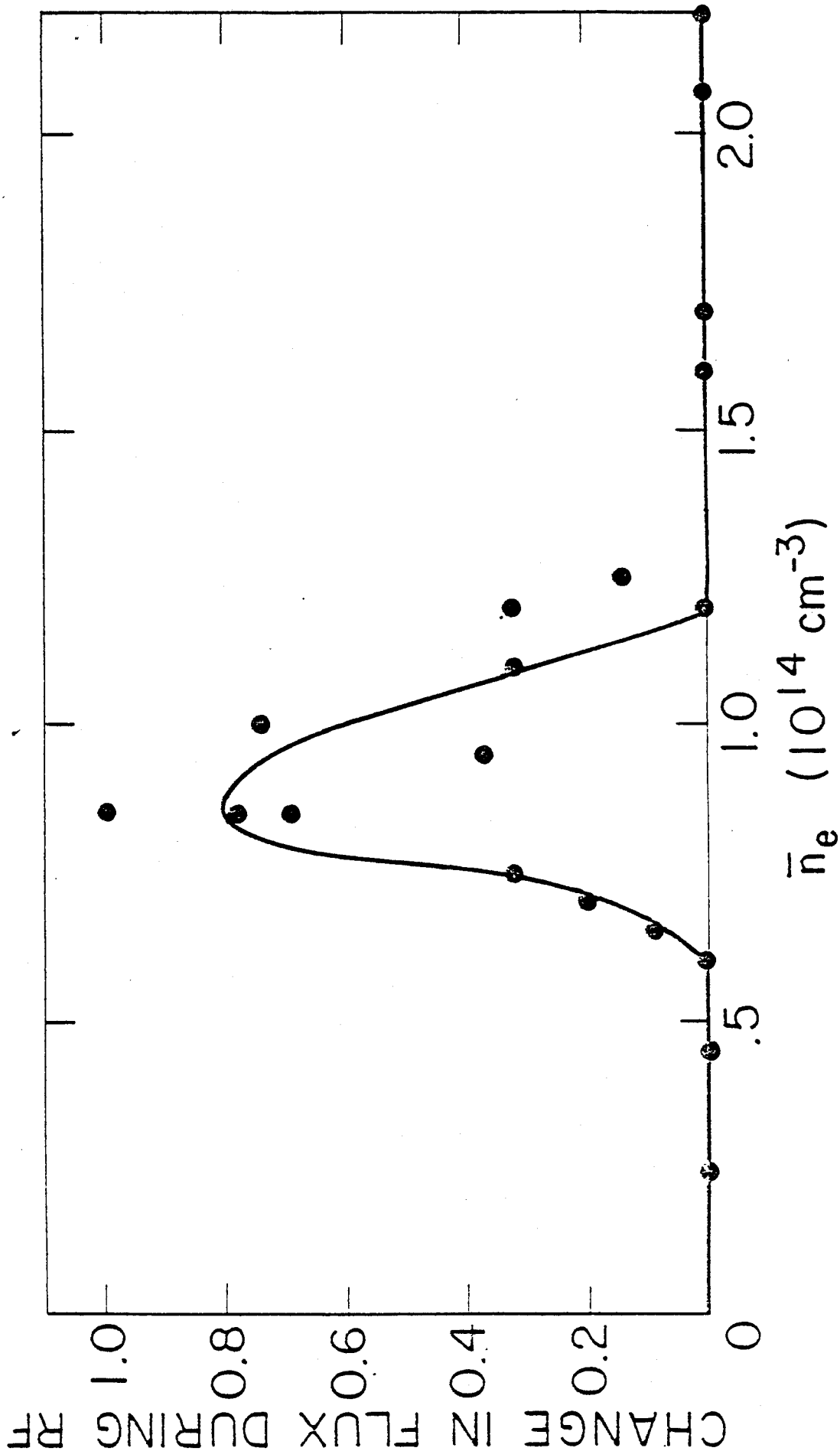
CHANGE IN FLUX DURING RF
0
0.2
0.4
0.6
0.8
1.0
.5
1.0
1.5
2.0
$\bar{n}_e$ (10^{14} cm^{-3})

Fig. 33

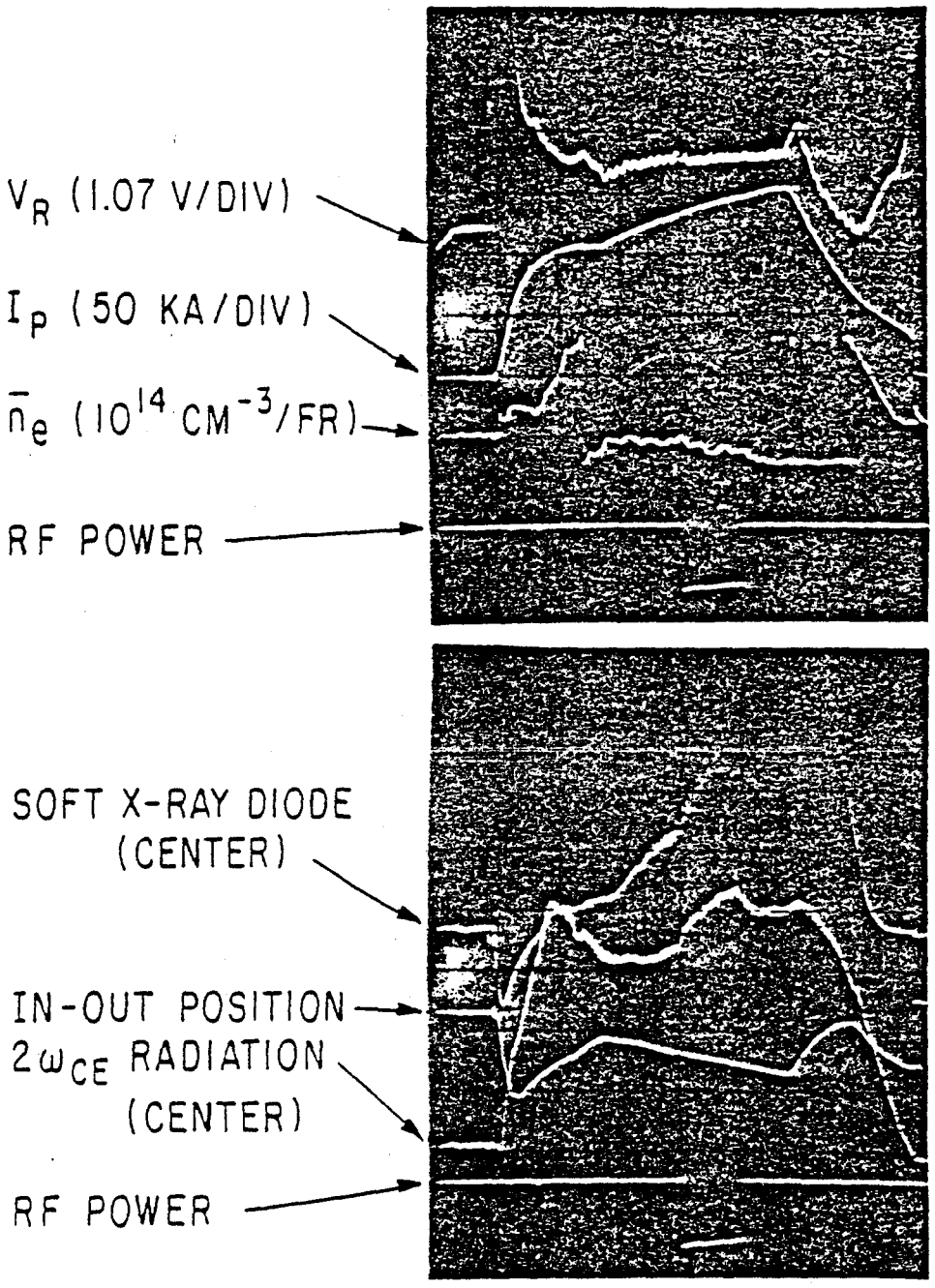
V_R (1.07 V/DIV)
I_p (50 KA/DIV)
$\bar{n}_e$ (10^{14} CM^{-3}/FR)
RF POWER
SOFT X-RAY DIODE (CENTER)
IN-OUT POSITION
$2\omega_{CE}$ RADIATION (CENTER)
RF POWER
20 MSEC / DIV

Fig. 34

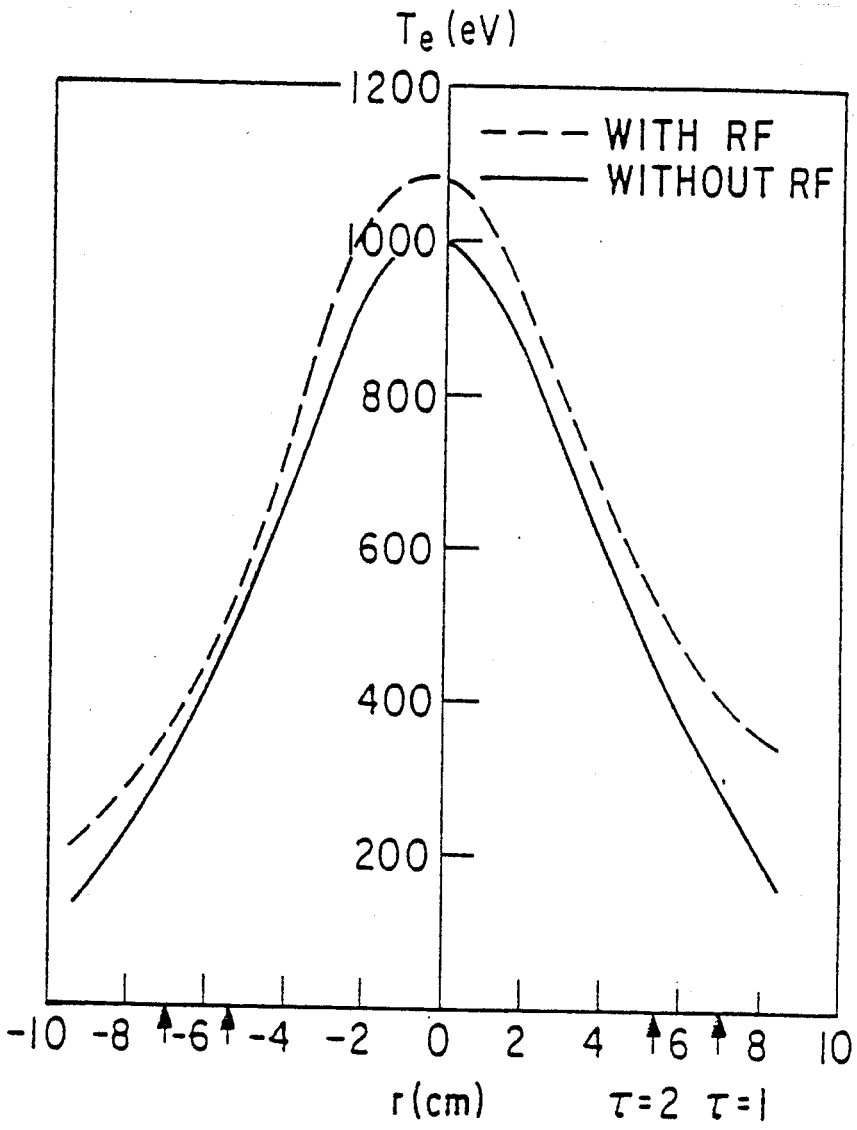
T_e (eV)
1200
1000
800
600
400
200
WITH RF
WITHOUT RF
-10 -8 -6 -4 -2 0 2 4 6 8 10
r(cm)
τ=2 τ=1

Fig. 35

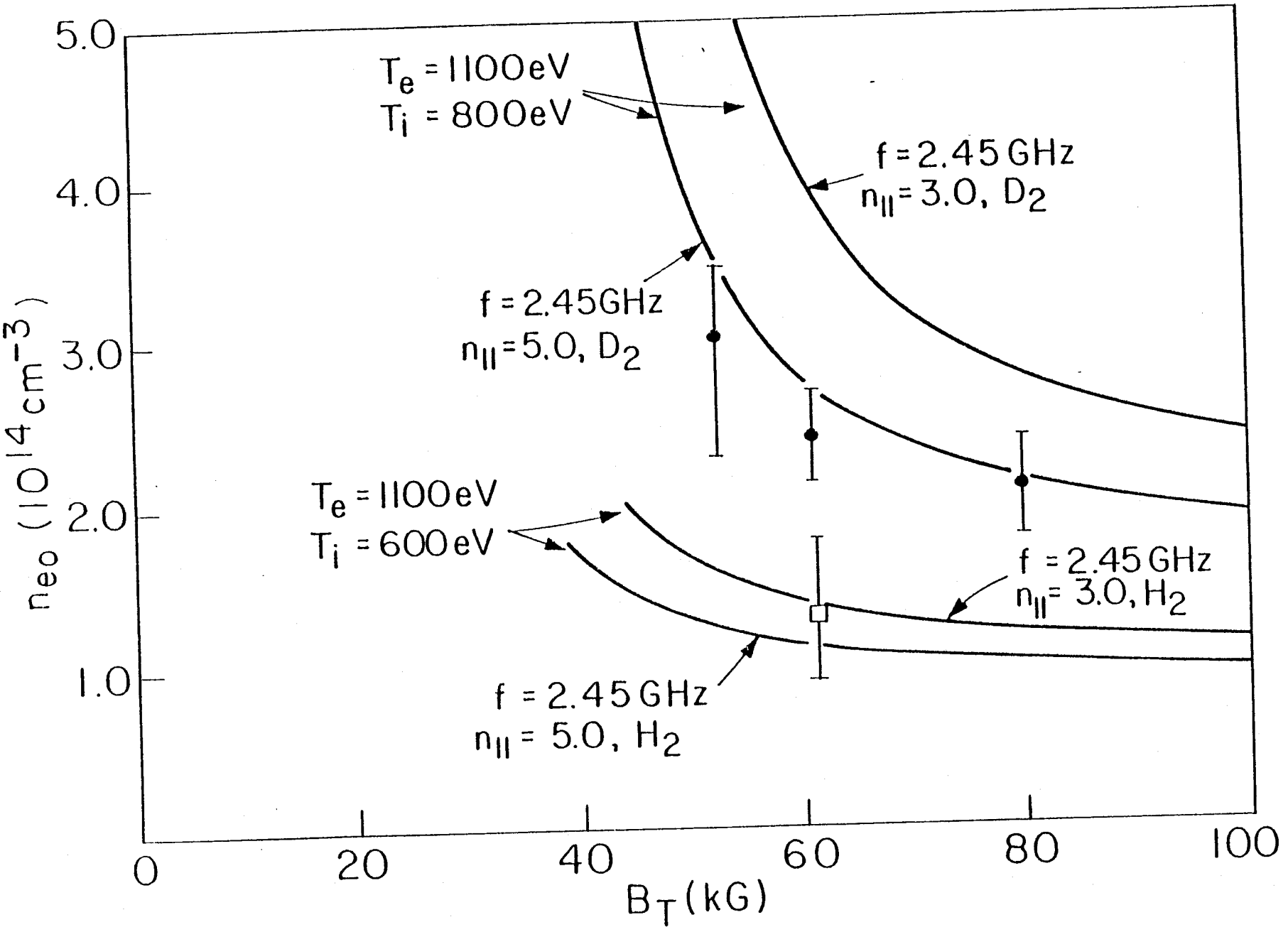
5.0
4.0
3.0
2.0
1.0
n_{eo} (10^{14} cm^{-3})
T_e = 1100eV
T_i = 800eV
f = 2.45 GHz
$n_{||}$ = 3.0, D_2
f = 2.45GHz
$n_{||}$ = 5.0, D_2
T_e = 1100eV
T_i = 600eV
f = 2.45 GHz
$n_{||}$ = 3.0, H_2
f = 2.45 GHz
$n_{||}$ = 5.0, H_2
0
20
40
60
80
100
B_T (kG)

(a)

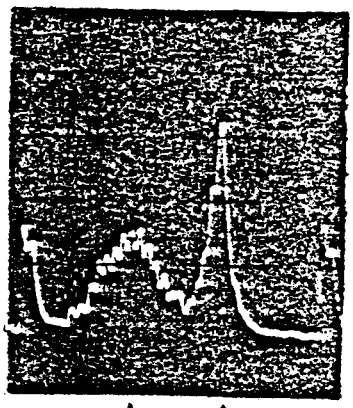

11 DB/DIV

2.0 GHz 2.45 GHz

(b)

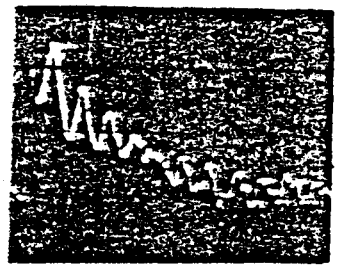

20 DB/DIV

103 MHz/DIV

0 Hz

Fig. 37

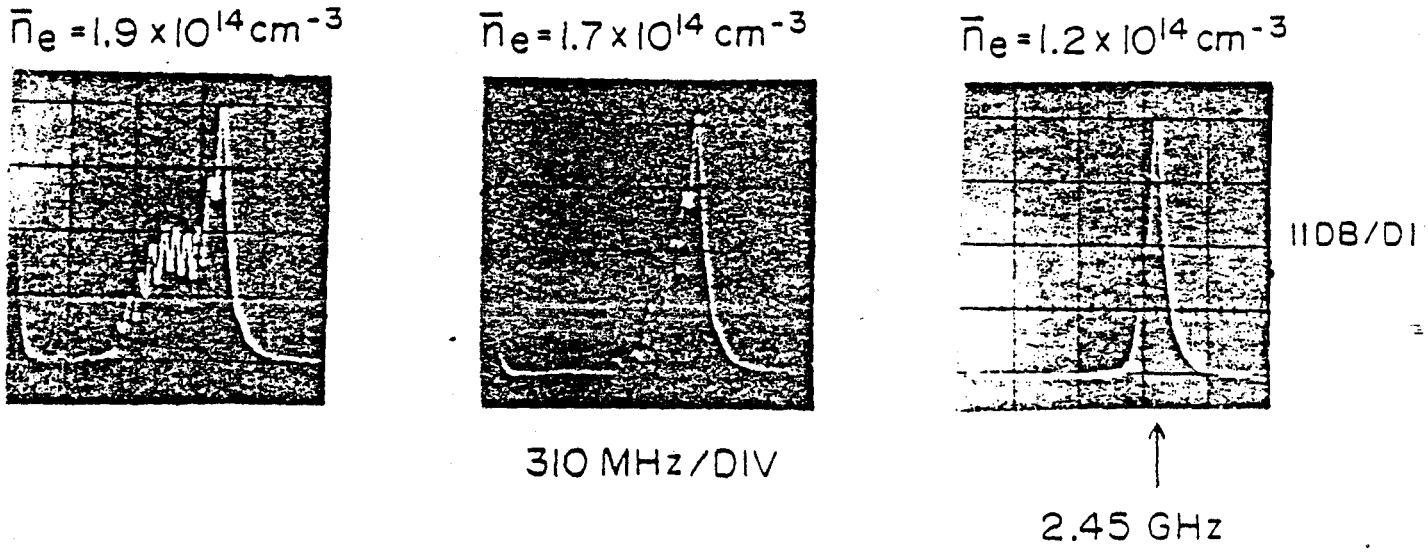
$\bar{n}_e = 1.9 \times 10^{14}\,cm^{-3}$
$\bar{n}_e = 1.7 \times 10^{14}\,cm^{-3}$
$\bar{n}_e = 1.2 \times 10^{14}\,cm^{-3}$
11DB/DI
310 MHz/DIV
2.45 GHz

Fig. 38

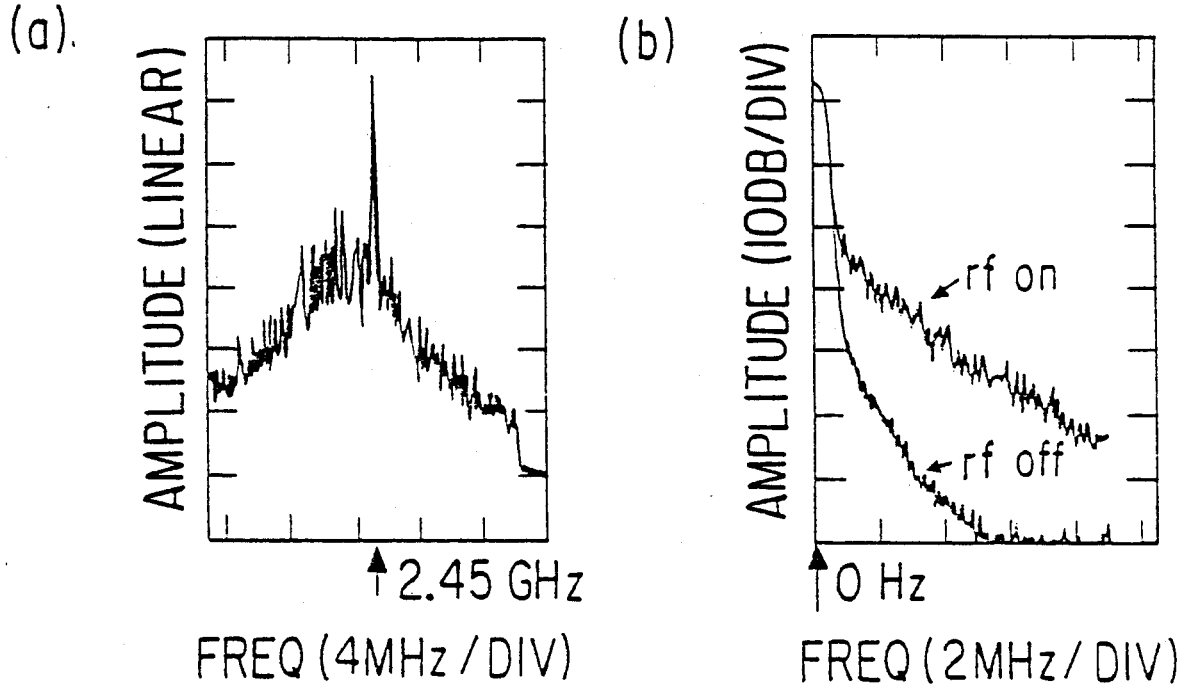
(a).
AMPLITUDE (LINEAR)
2.45 GHz
FREQ (4MHz / DIV)
(b)
AMPLITUDE (10DB/DIV)
rf on
rf off
0 Hz
FREQ (2MHz / DIV)

Fig. 39

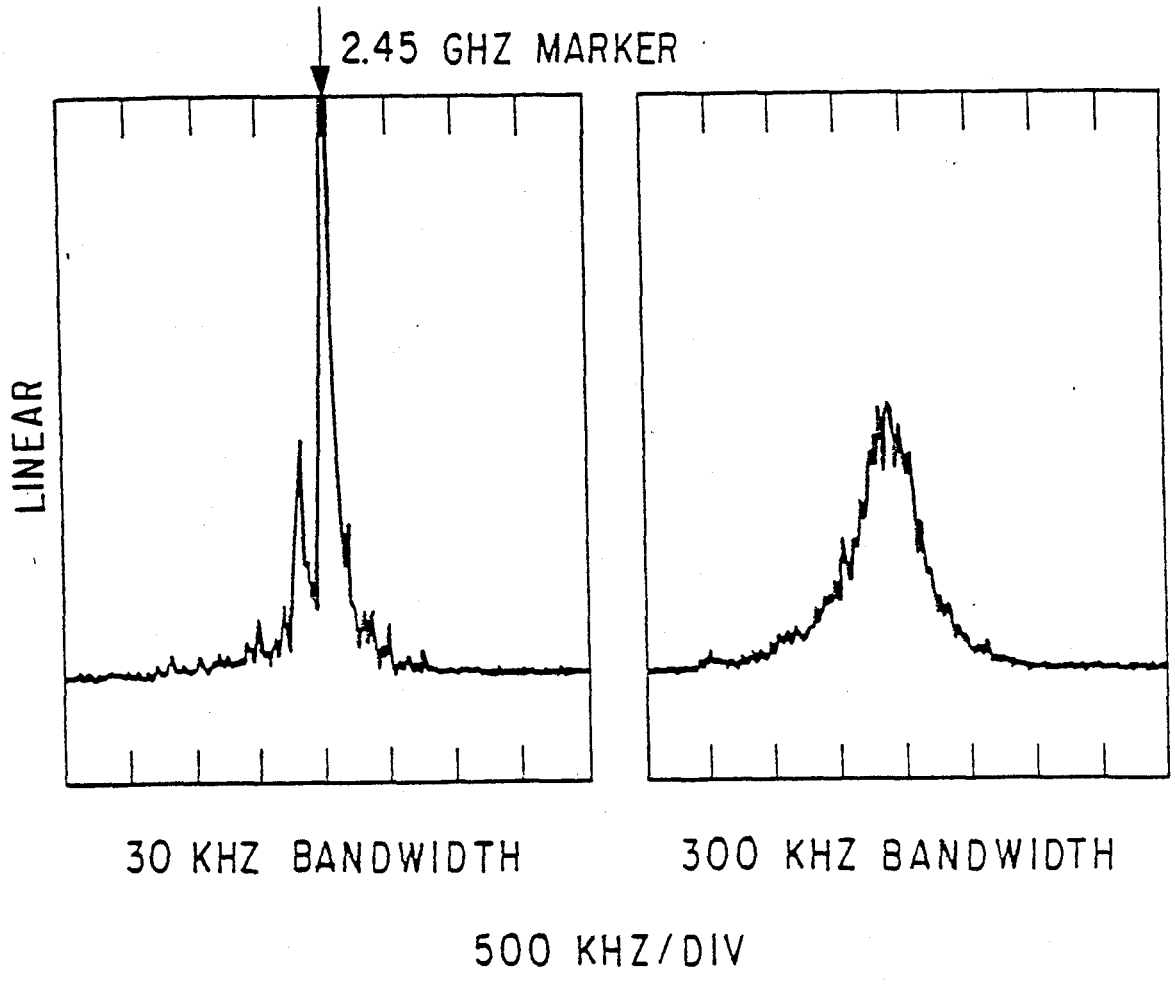
2.45 GHZ MARKER
LINEAR
30 KHZ BANDWIDTH
300 KHZ BANDWIDTH
500 KHZ/DIV

Fig. 40

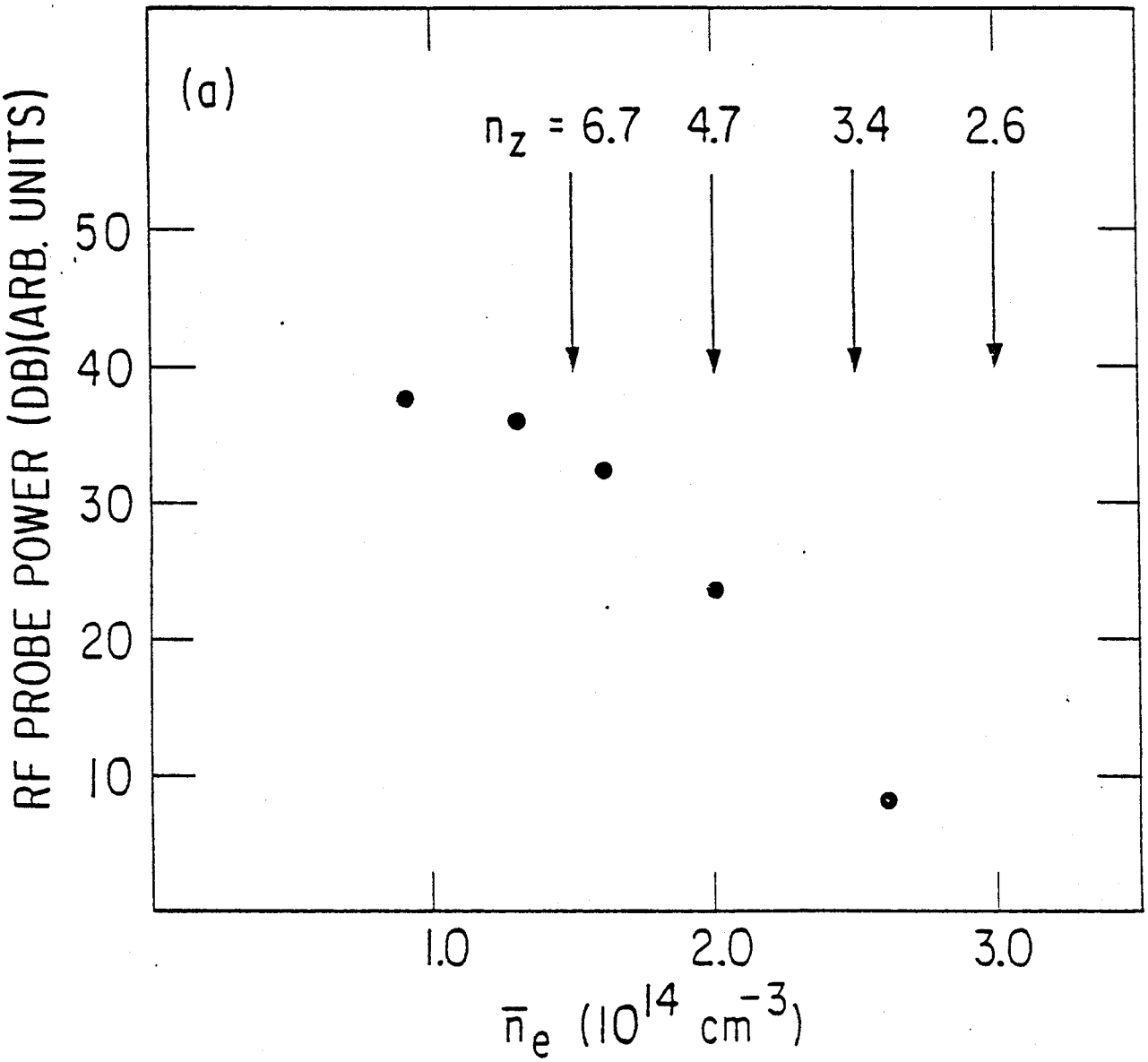
(a)
n_z = 6.7 4.7 3.4 2.6
RF PROBE POWER (DB)(ARB. UNITS)
50
40
30
20
10
1.0
2.0
3.0
$\bar{n}_e$ (10^{14} cm^{-3})

Fig. 41

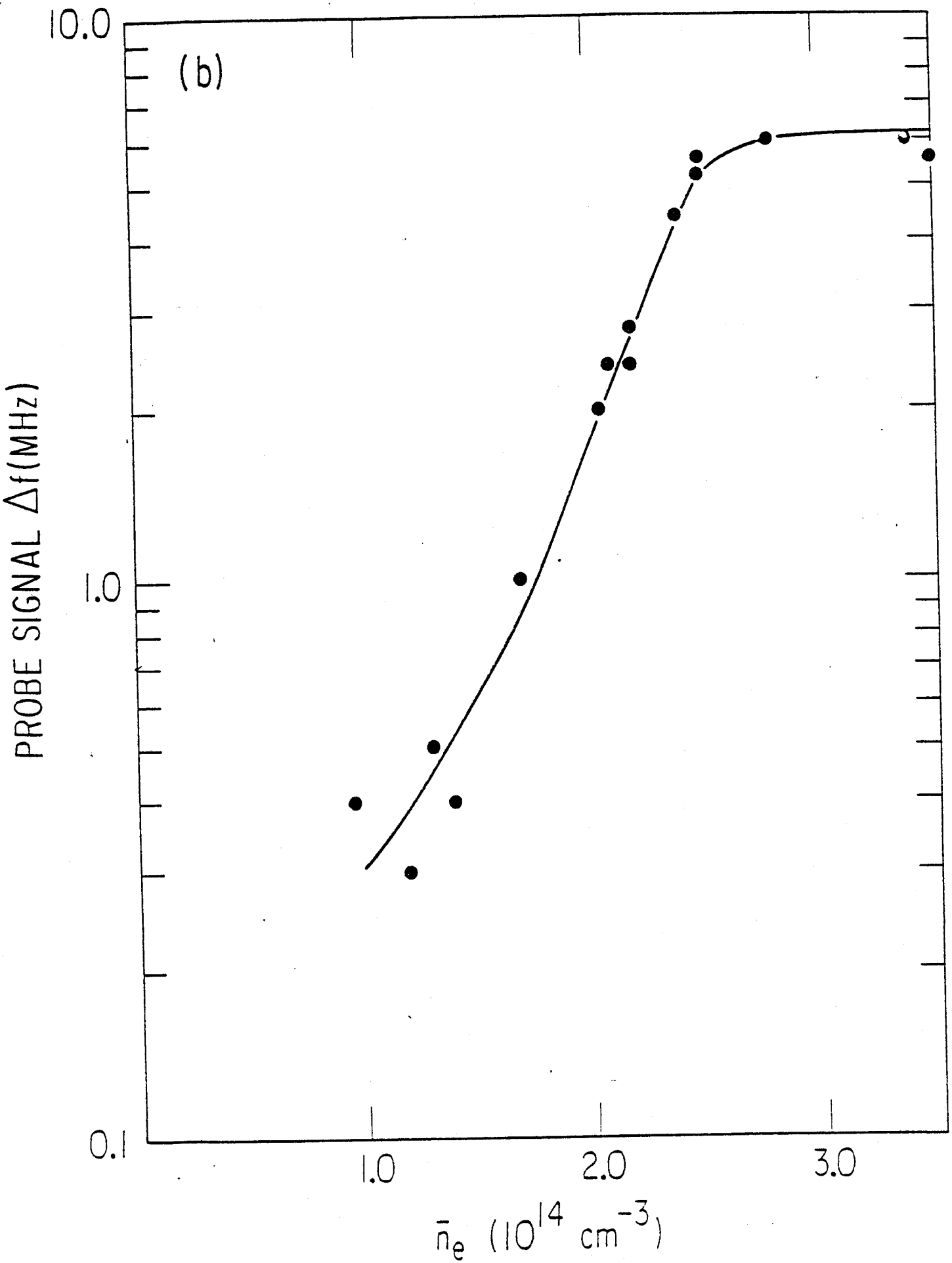

Fig. 41

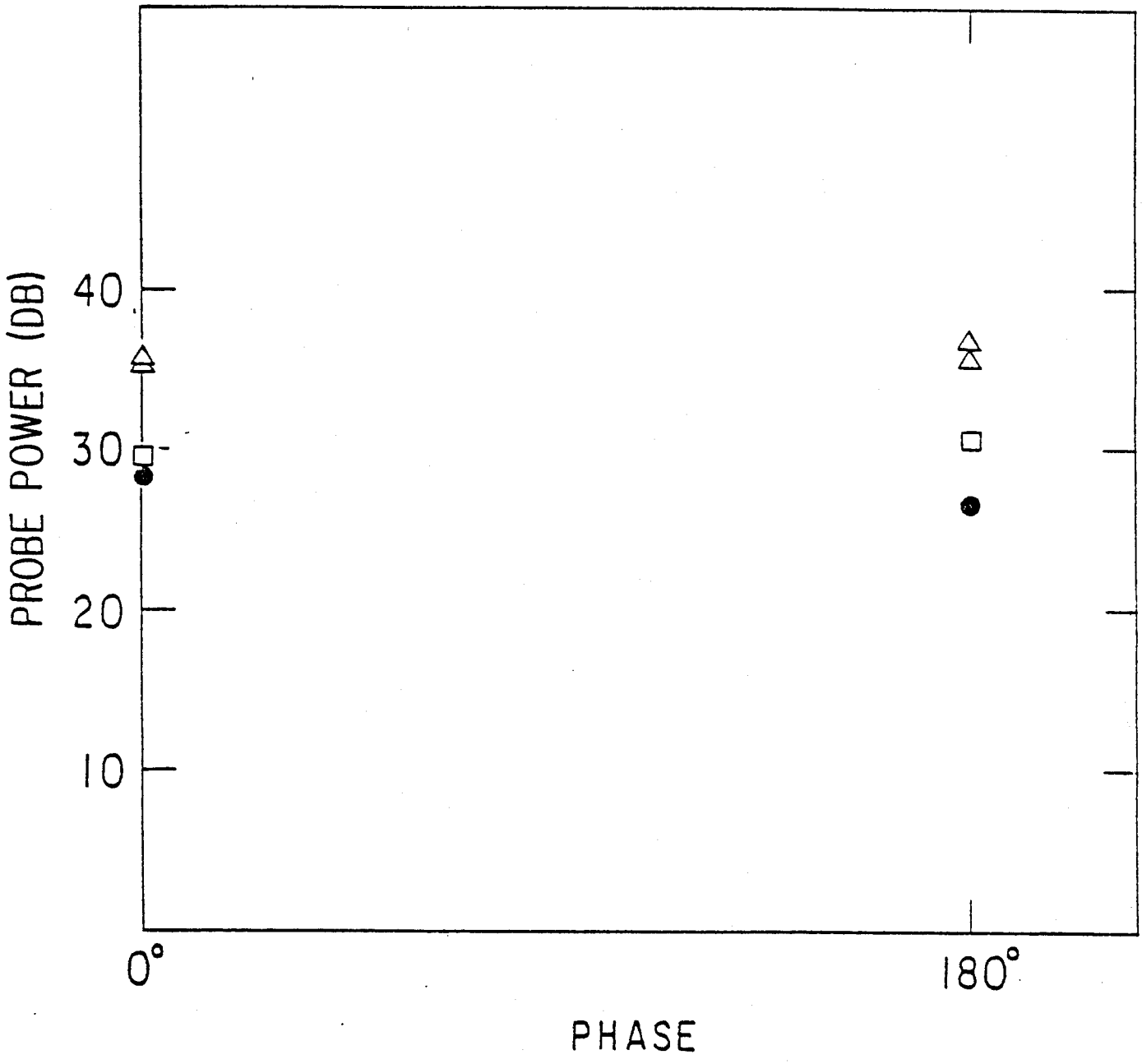

Fig. 42

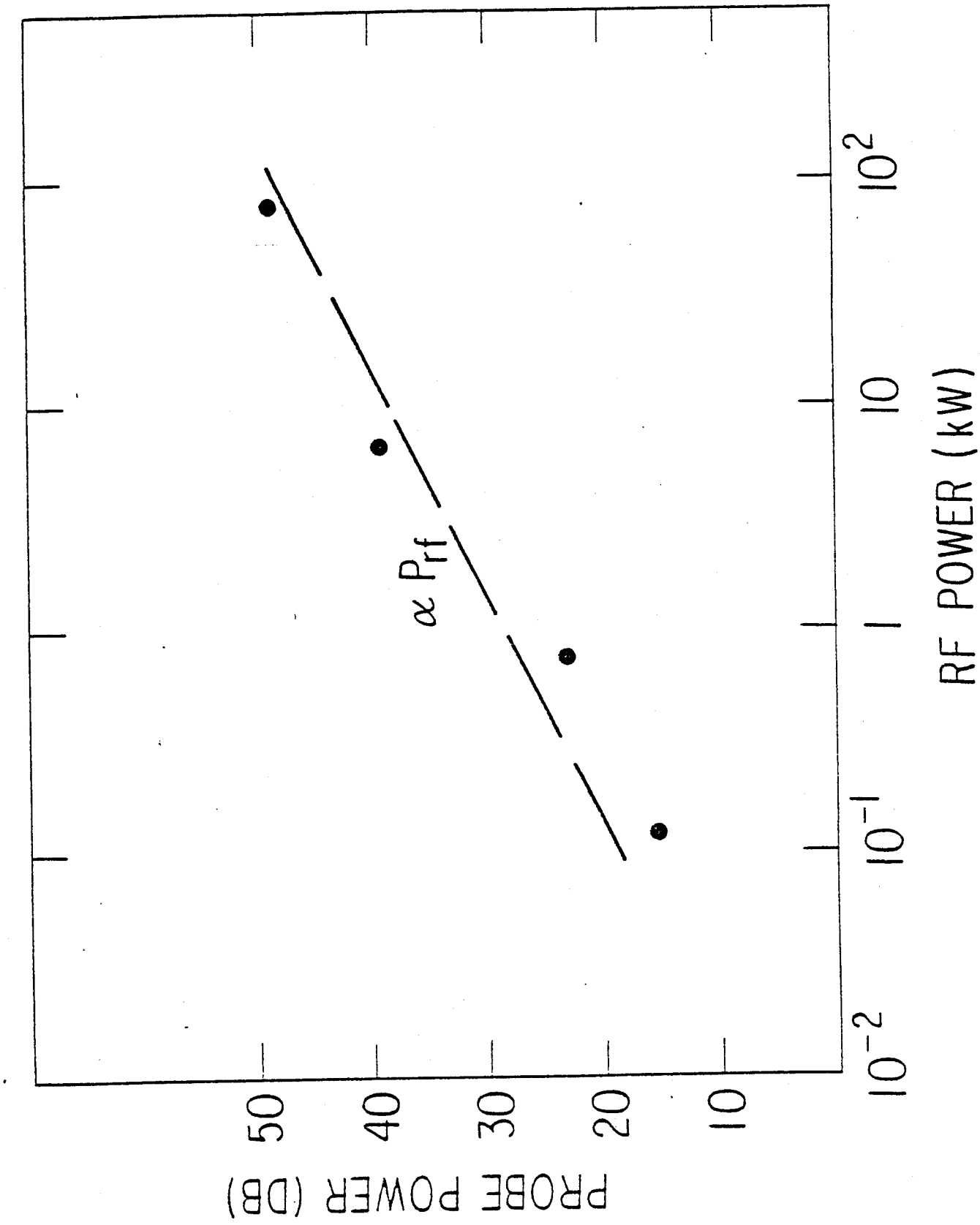
PROBE POWER (DB)
50
40
30
20
10
RF POWER (kW)
10^{-2}
10^{-1}
1
10
10^{2}
αP_{rf}

Fig. 43

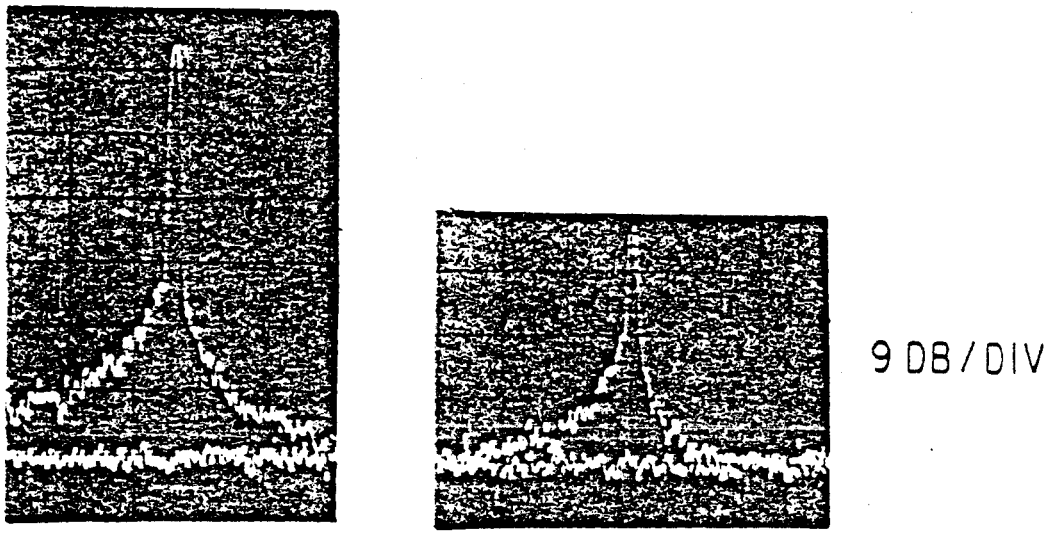

Fig. 44

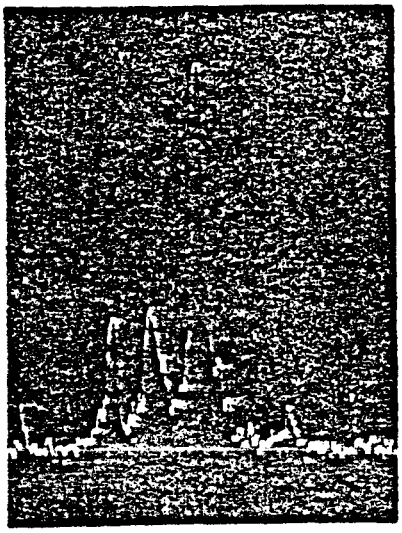

9 DB/DIV

2 MHZ/DIV

Fig. 45

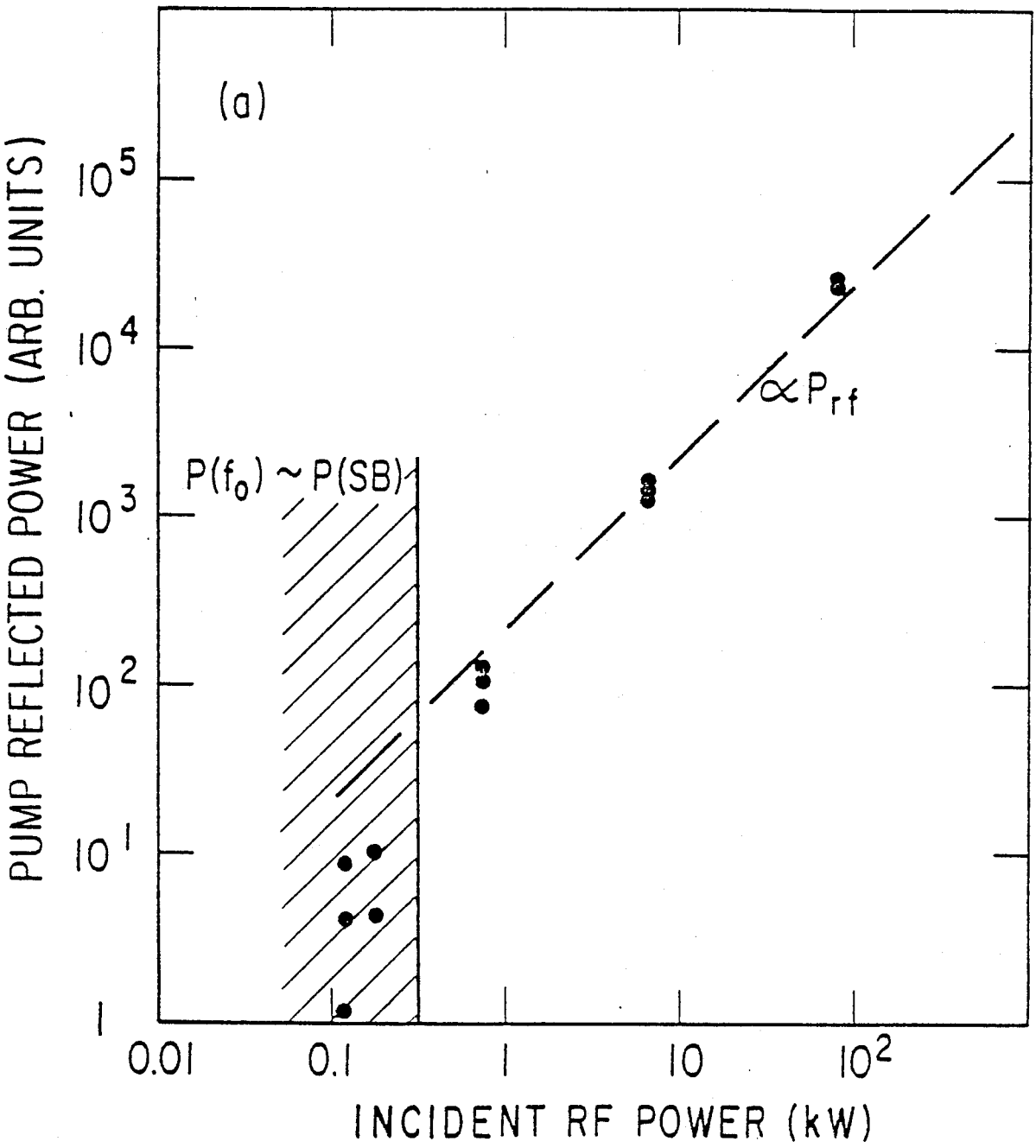
(a)
PUMP REFLECTED POWER (ARB. UNITS)
10^5
10^4
10^3
10^2
10^1
1
$\propto P_{rf}$
$P(f_0) \sim P(SB)$
0.01
0.1
1
10
10^2
INCIDENT RF POWER (kW)

Fig. 46

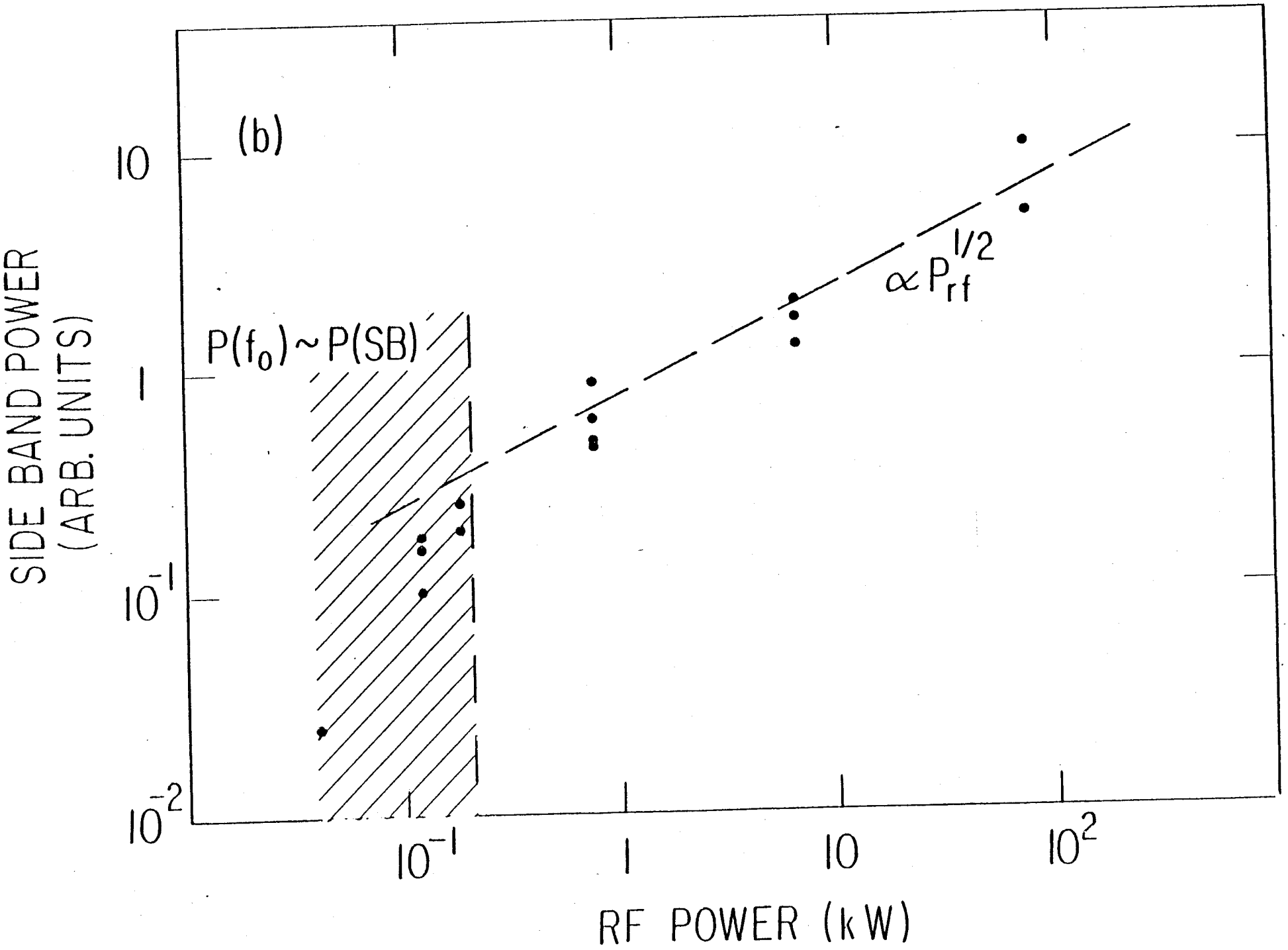
(b)
10
1
10^{-1}
10^{-2}
SIDE BAND POWER
(ARB. UNITS)
$P(f_0) \sim P(SB)$
$\propto P_{rf}^{1/2}$
10^{-1}
1
10
10^2
RF POWER (kW)

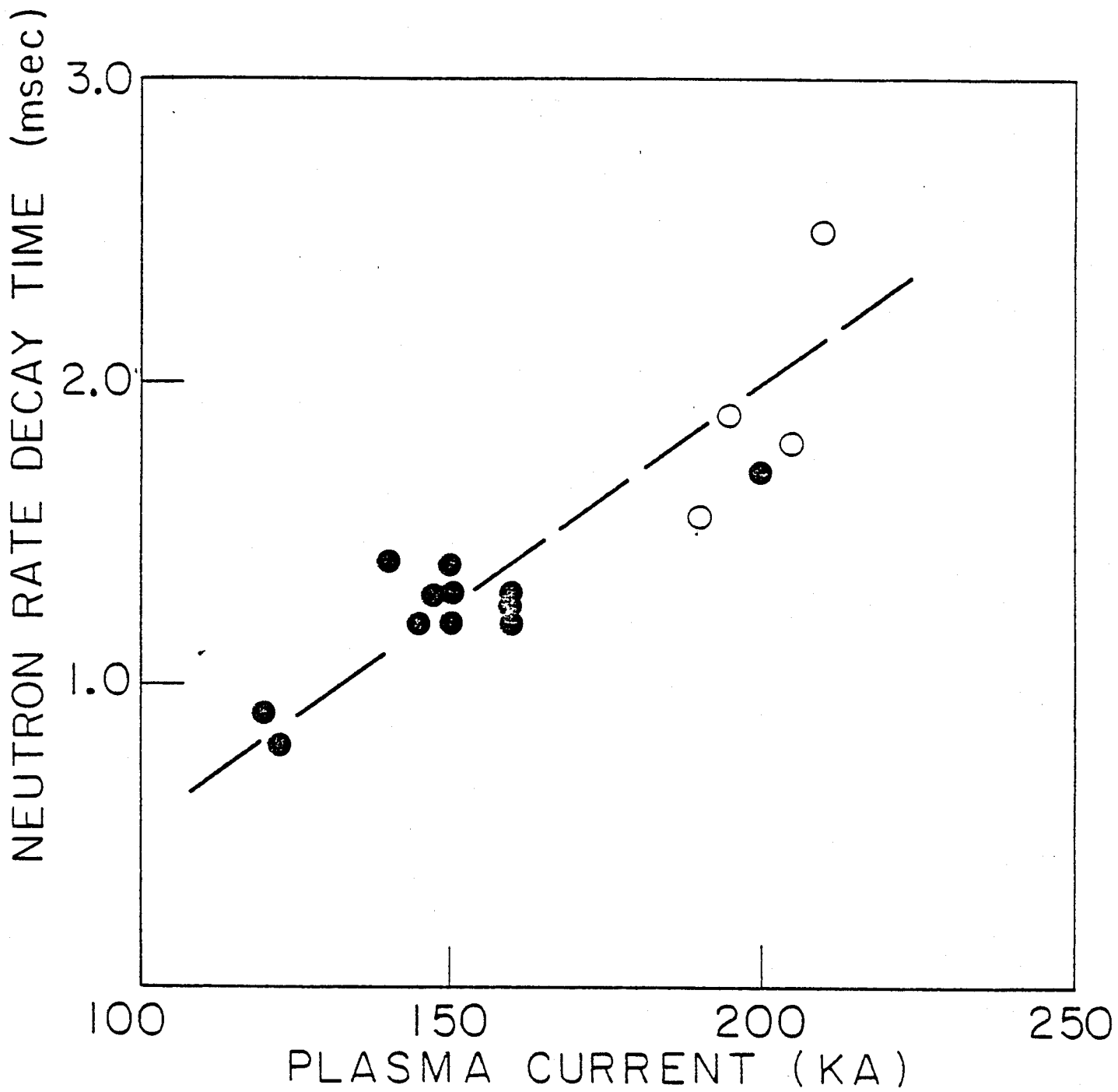
NEUTRON RATE DECAY TIME (msec)
3.0
2.0
1.0
100
150
200
250
PLASMA CURRENT (KA)

Fig. 47

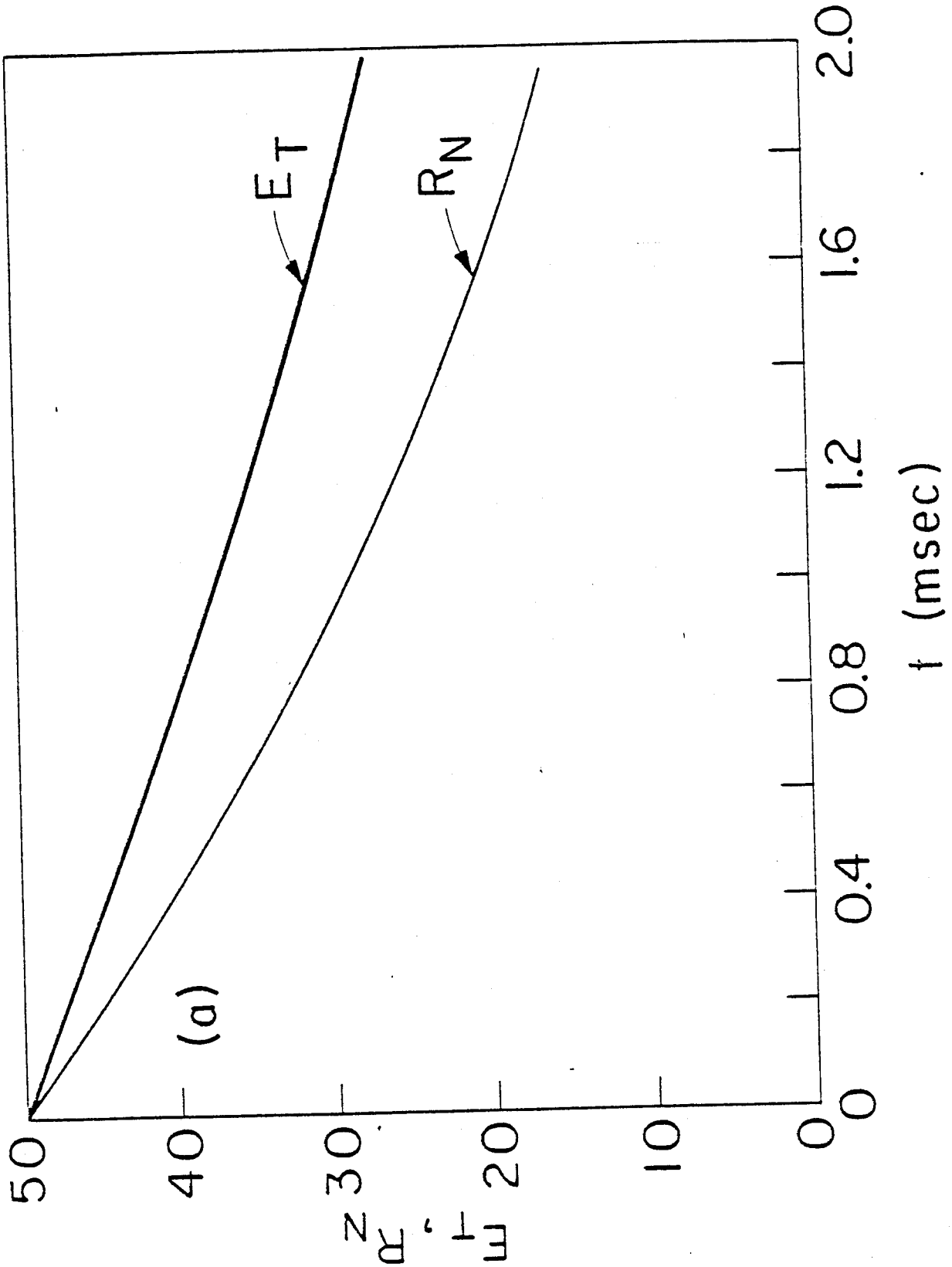

Fig. 48

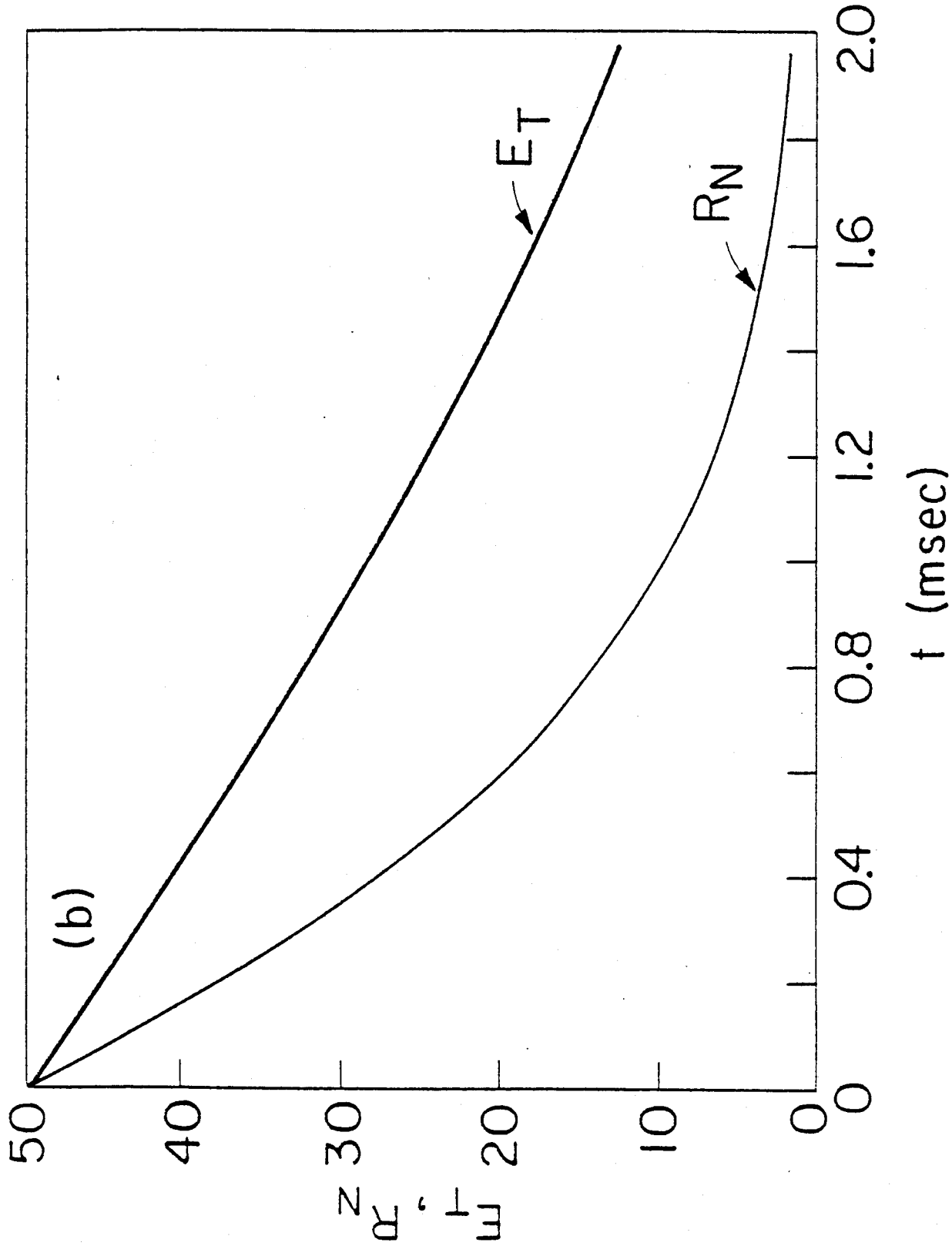

Fig. 43

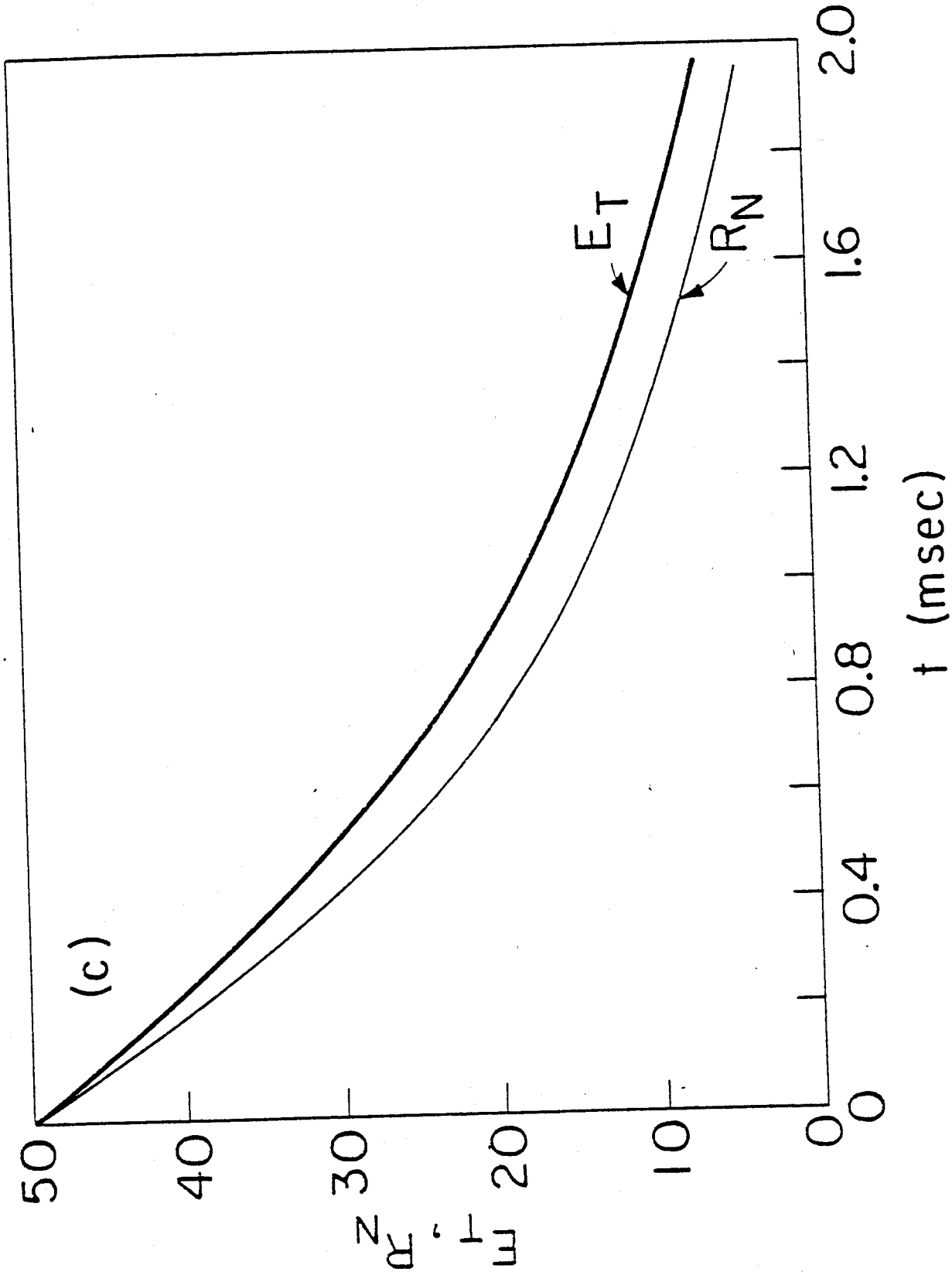

Fig. 48

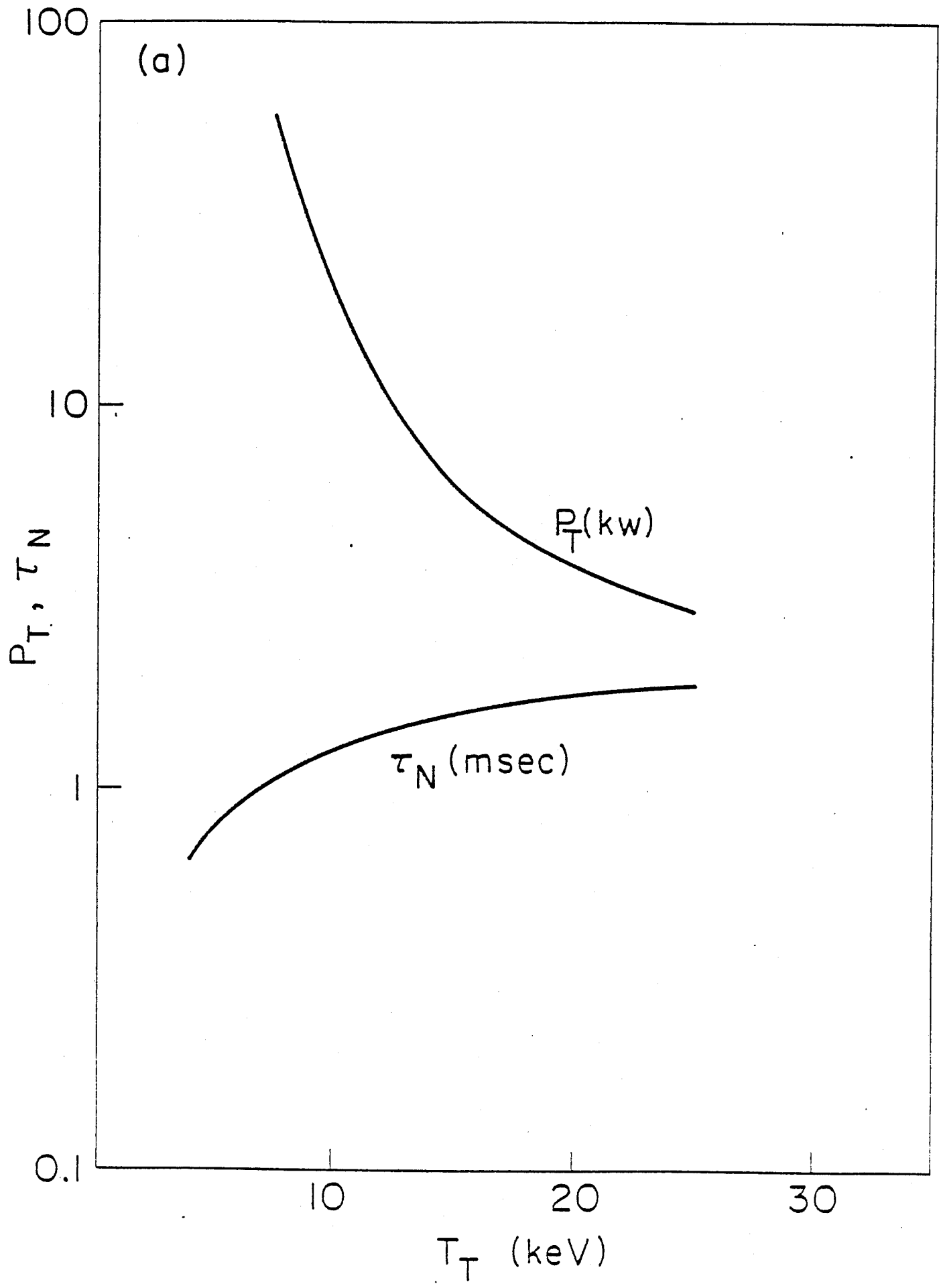

Fig. 49

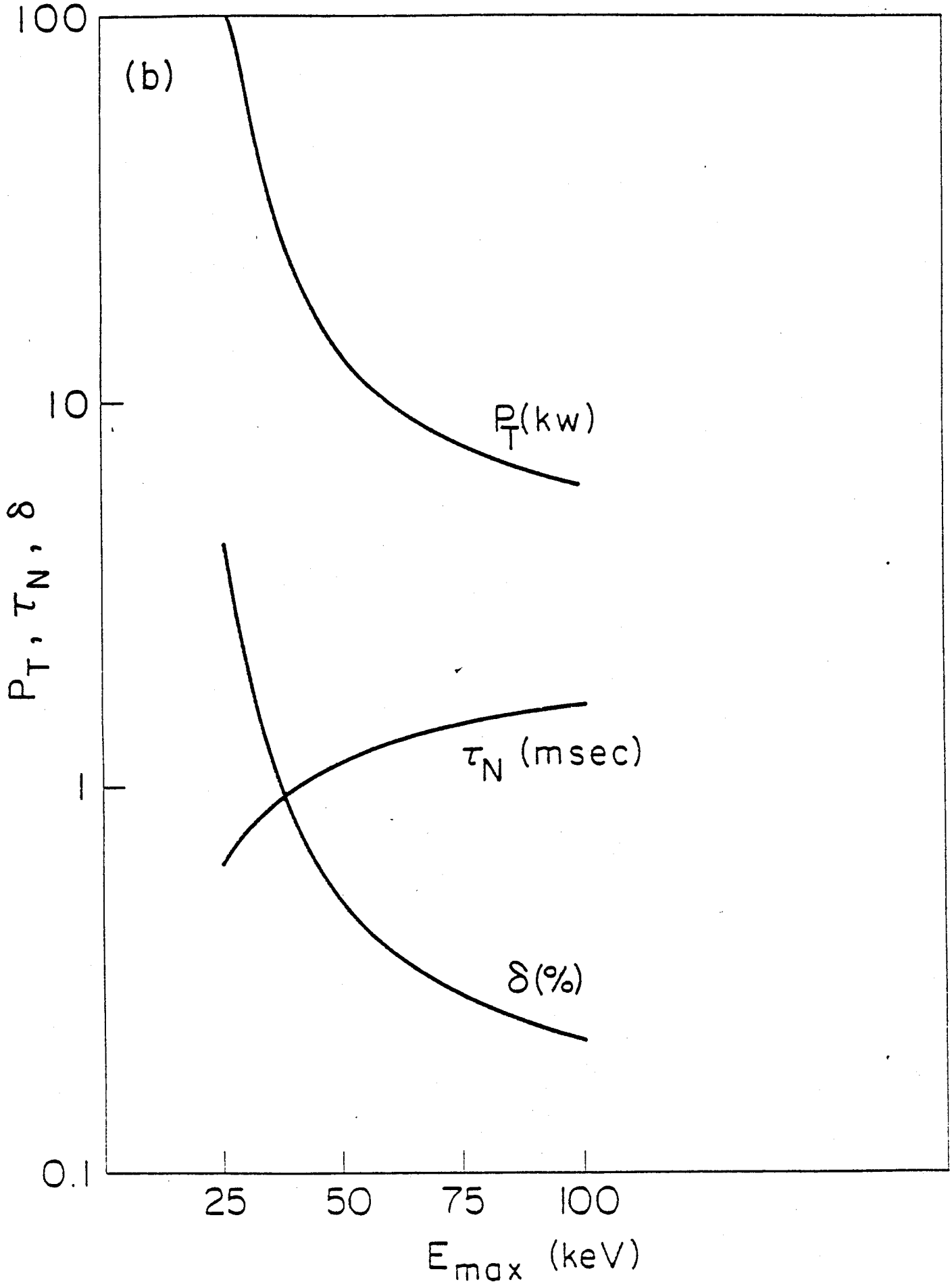
100
(b)
10
1
0.1
P_T, τ_N, δ
P_T(kw)
τ_N (msec)
δ(%)
25
50
75
100
E_{max} (keV)

Fig. 49